

DEPARTMENT OF PHYSICS, UNIVERSITY OF JYVÄSKYLÄ

**JET TRANSVERSE MOMENTUM DISTRIBUTIONS
MEASURED BY ALICE**

**BY
TOMAS SNELLMAN**

PHD thesis

Supervisors: Jan Rak, Dong Jo Kim

Jyväskylä, Finland
December, 2018

3 Contents

4	1	Introduction	3
5	1.1	Quantum chromodynamics	4
6	1.1.1	Foundation of QCD	4
7	1.1.2	Asymptotic Freedom	5
8	1.2	Heavy ion physics	9
9	1.2.1	History	9
10	1.3	Features of Heavy-Ion Collisions	11
11	1.3.1	Collision Geometry	11
12	1.3.2	Nuclear Geometry	12
13	1.3.3	Hydrodynamical Modelling	15
14	1.4	Flow	18
15	1.4.1	Anisotropic Flow	19
16	1.4.2	High p_T Phenomena	20
17	1.5	Hard processes	21
18	1.5.1	pQCD factorization	21
19	1.5.2	Jet hadronisation	23
20	1.5.3	Jet energy loss	27
21	1.5.4	Monte Carlo Implementations	35
22	1.6	QGP in Small systems	35
23	1.6.1	Collective phenomena	35
24	1.6.2	Absence of jet quenching	37
25	1.6.3	Centrality determination in small systems	38
26	2	Experimental setup and data samples	42
27	3	Experimental Details	43
28	3.1	CERN	43
29	3.2	Large Hadron Collider	45
30	3.2.1	LHC experiments	46
31	3.3	ALICE	46
32	3.3.1	Tracking	47
33	3.3.2	TPC	49
34	3.3.3	TPC upgrade	49
35	3.3.4	Particle identification	51
36	3.3.5	Electromagnetic Calorimeter	52

37	3.3.6	Forward detectors	52
38	3.3.7	Muon spectrometer	53
39	3.3.8	Trigger	54
40	4	Event and track selection	55
41	5	Analysis method	55
42	5.1	Jet Finding	55
43	5.1.1	Anti k_T algorithm	55
44	5.2	j_T	56
45	5.2.1	1 over j_T	56
46	5.3	Unfolding	57
47	5.3.1	Bayesian unfolding	58
48	5.3.2	Toy Monte Carlo	58
49	5.3.3	Pythia Response matrices	59
50	5.3.4	2D response matrices	60
51	5.3.5	Unfolding algorithm	60
52	5.3.6	Effect of number of iterations	60
53	5.3.7	Effect of different prior	61
54	5.3.8	Effect of p_T truncation	61
55	5.3.9	Unfolding closure test	61
56	5.4	Background	63
57	5.4.1	Perpendicular cone background	64
58	5.4.2	Random background	64
59	5.4.3	Auto-correlations	67
60	5.5	Fitting	67
61	6	Systematic uncertainties	68
62	7	TPC Upgrade?	70
63	8	Systematic errors	71
64	8.1	Background subtraction	71
65	8.2	Unfolding	71
66	8.3	Tracking	71
67	8.4	Combining systematics	71
68	9	Results	74
69	9.1	statistics	74
70	9.2	Data	74
71	9.3	Inclusive results	74
72	9.4	Background	75

73	9.5	Comparison between A and C side	75
74	9.6	Subtracted signal	75
75	9.7	Fitting	76
76	9.7.1	Results	76
77	9.8	Comparison to dihadron results	76
78	9.9	Different R parameters	80
79	10	Discussion	83
80	10.1	Discussion	83
81	10.1.1	Dihadron j_T	83
82	11	Summary	87

83 List of Figures

84	1	QCD phase diagram	7
85	2	η/s vs $(T - T_c)/T_c$	8
86	3	The definitions of the Reaction Plane and Participant Plane coordinate systems	11
88	4	Interaction between partons in central and peripheral collisions.	12
89	5	An illustration of the multiplicity distribution in ALICE measurement with centrality classes.	13
91	6	The results of one Glauber Monte Carlo simulation.	16
92	7	Schematic representation of a heavy-ion collision	17
93	8	Charged particle spectra	18
94	9	Illustration of flow in momentum space in central and peripheral collisions.	19
96	10	QCD Leading Order	21
97	11	Hard scattering	21
98	12	Jet showering	22
99	16	Elliptic flow, v_2 from $p_T = 1$ to 60 GeV/ c	30
100	17	Photon spectrum	31
101	18	Measurements of the nuclear modification factor R_{AA} in central heavy-ion collisions	33
103	19	A comparison between observed $R_{AA}(\Delta\phi, p_T)$ and R_{AA} using v_2	34
104	20	Calculations of the initial energy density in small collision systems at RHIC and the resulting hydrodynamic evolution.	36
106	21	Two-particle correlation results in PbPb, pPb, and pp collisions at the LHC [].	36
108	22	RpA in proton-lead collisions	38

109	23	Distribution of the sum of amplitudes in the V0A hodoscopes (Pb-going), as well as the NBD-Glauber fit (explained in the text). Centrality classes are indicated by vertical lines. The inset shows a zoom-in on the most peripheral events. [?]	40
110			
111			
112			
113	24	Top: Scatter plot of number of participating nucleons versus impact parameter; Bottom: Scatter plot of multiplicity versus the number of participating nucleons from the Glauber fit for V0A. The quantities are calculated with a Glauber Monte Carlo of p-Pb (left) and Pb-Pb (right) collisions. [?]	41
114			
115			
116			
117	25	CERN collider complex	44
118			
119	26	ALICE	47
120			
121	27	ITS	48
122			
123	28	TPC	50
124			
125	29	Illustration of \vec{j}_T . The jet fragmentation transverse momentum, \vec{j}_T , is defined as the transverse momentum component of the track momentum, \vec{p}_{track} , with respect to the jet momentum, \vec{p}_{jet} .	56
126			
127	30	Results from unfolding in Toy Monte Carlo	59
128			
129	31	Unfolding with different number of iterations	61
130			
131	32	Effect of changing minimum jet p_T used in unfolding from 5 to 10 GeV	62
132			
133	33	Effect of changing minimum jet p_T used in unfolding from 5 to 10 GeV	62
134			
135	35	j_T Response matrices in single jet p_T bins	64
136			
137	36	Pythia closure test results. Fake tracks include also tracks that do exist in the true dataset, but for one reason or another were not given j_T values. j_T is only calculated for tracks that are associated with jets	65
138			
139	38	j_T signal with random background subtraction fits in different jet p_T bins	71
140			
141	39	Differences between perpendicular cone and random background subtraction in the resulting RMS values.	72
142			
143	40	j_T signal with random background subtraction fits in different jet p_T bins	72
144			
145	41	Differences between Bayesian and SVD unfolding in the resulting RMS values	72
146			
147	42	Inclusive j_T with background	75
148			
149	43	j_T background with two different methods	76
150			
151	44	Comparison of inclusive j_T distributions between A and C side for minimum bias and EMCAL triggered data.	77
152			
153	45	j_T signal with background subtracted	78

149	46	Comparison of the effect of background method on j_T signal.	78
150	47	j_T signal fits in different jet p_T bins	79
151	48	RMS values extracted from the fits for the gaussian (narrow) and inverse gamma (wide) components	79
152	49	RMS values extracted from the fits for the gaussian (narrow) and inverse gamma (wide) components	80
153	50	Jet j_T results are compared to results obtained in the dihadron analysis. This is done both in jet p_T and trigger p_T bins by converting between them.	80
154	51	Pythia R parameters j_T	81
155	52	Pythia R parameters RMS	82
156	53	Dihadron j_T results	83
157	54	RMS values of the narrow and wide j_T components in the dihadron correlation analysis. Results from pp collisions at $\sqrt{s} = 7$ TeV (circular symbols) and from p–Pb collisions at $\sqrt{s_{NN}} = 5.02$ TeV (square symbols) are compared to PYTHIA 8 tune 4C simulations at $\sqrt{s} = 7$ TeV (short dashed line) and at $\sqrt{s} = 5.02$ TeV (long dashed line). Different panels correspond to different x_{\parallel} bins with $0.2 < x_{\parallel} < 0.4$ on the left, $0.4 < x_{\parallel} < 0.6$ in the middle, and $0.6 < x_{\parallel} < 1.0$ on the right. The statistical errors are represented by bars and the systematic errors by boxes. [107]	84
158	55	Comparison of results with dihadron j_T results. Dihadron trigger p_T bins are converted to jet p_T bins using observed mean $p_{T,jet}$ values in $p_{T,trigger}$ bins. Dihadron results are for $0.2 < x_{\parallel} < 0.4$	85
159	56	PYTHIA R parameters j_T	86
160	57	Results of calculating j_T with respect to the jet axis or the leading hadron. The assumption is that because the leading hadron is an imperfect estimate of the jet axis, low j_T tracks should on average be shifted to higher j_T	86

178 1 Introduction

179 At sufficiently high energies quarks and gluons are no longer bound to hadrons,
180 but they form a deconfined state known as Quark-Gluon plasma (QGP). The
181 main goal of heavy ion physics is the study of QGP and its properties. One of the
182 experimental observables that is sensitive to the properties of QGP is the azimuthal
183 distribution of particles in the plane perpendicular to the beam direction.

184 When nuclei collide at non-zero impact parameter (non-central collisions), their
185 overlap region is asymmetric. This initial spatial asymmetry is converted via multi-
186 ple collisions into an anisotropic momentum distribution of the produced particles.
187 For low momentum particles ($p_T \lesssim 3$ GeV/c), this anisotropy is understood to
188 result from hydrodynamically driven flow of the QGP [1–5].

189 One way to characterize this anisotropy is with coefficients from a Fourier se-
190 ries parametrization of the azimuthal angle distribution of emitted hadrons. The
191 second order coefficient, v_2 which is also known as elliptic flow, shows clear depen-
192 dence on centrality. The collision geometry is mainly responsible for the elliptic
193 flow. Higher harmonics don't depend that much on centrality. These higher har-
194 monics carry information about the fluctuations in collisions. The event-by-event
195 fluctuations have an increasing importance in measurements and it has been ob-
196 served that measurements of elliptic flow in central collisions and measurements
197 of higher order harmonics are consistent with the assumption that flow in these
198 cases is mainly due to fluctuations [6].

199 At LHC energies $\sqrt{s_{NN}} = 2.76\text{GeV}$ it has been observed that in general there
200 is little difference to flow at RHIC energies. The v_2 coefficient is about 20% greater
201 at LHC than at RHIC, depending on the centrality bin. The particle identified
202 v_2 for kaons and pions follows the same trend. However it was observed that for
203 proton v_2 the quark number scaling does not work [7]. So far there is no agreement
204 of why this scaling breaks down at LHC or why it works so well at RHIC energies.

205 **1.1 Quantum chromodynamics**

206 **1.1.1 Foundation of QCD**

207 There are four known basic interactions in the universe: gravity, electromagnetic,
208 weak and strong interactions. The standard model of particle physics includes
209 three of these excluding the gravitational interaction. The theory of strong inter-
210 actions is known as Quantum Chromodynamics (QCD).

211 The development of QCD began after the introduction of new powerful particle
212 accelerators that were capable of particle physics research in the 1950s. Before this
213 particles were mainly discovered from cosmic rays. Positrons, neutrons and muons
214 were discovered in the 1930s and charged pions were discovered in 1947 []. The
215 neutral pion was discovered in 1950 [8].

216 The Lawrence Berkeley National Laboratory started the Bevalac accelerator in
217 1954, Super Proton Synchrotron (SPS) in CERN began operating in 1959 and the
218 Alternating Gradient Synchrotron at Brookhaven started in 1960. With an energy
219 of 33GeV AGS was the most powerful accelerator of that time. By the beginning
220 of 1960s several new particles had been discovered. These include antiprotons,
221 antineutrons, Δ -particles and the six hyperons (Ξ^0 , Ξ^- , Σ^\pm , Σ^0 and Λ).

222 Facing this number of different particles started the search for symmetries. Al-
223 ready in 1932 Heisenberg [9] had proposed an isospin model to explain similarities
224 between the proton and the neutron. In 1962 Gell-Mann and Ne'eman presented
225 that particles sharing the same quantum numbers (spin, parity) could be organ-
226 ised using the symmetry of SU(3). [10] Heisenberg's Isospin model followed the
227 symmetry of SU(2). Using the SU(3) model known baryons and mesons could be
228 presented as octets. This also lead to the discovery of the Ω^- particle since this
229 was missing from the SU(3) decoupler that included heavier baryons.

230 The most simple representation of SU(3) was a triplet. Inside this triplet
231 particles would have electric charges $2/3$ or $-1/3$. These had not been however
232 detected. In 1964 Gell-Mann [11] and Zweig proposed that baryons and mesons
233 would bound states of these three hypothetical triplet particles that Gell-Mann
234 called quarks. Now we know that these are the u , d and s quarks. This original
235 quark model was violating the Pauli exclusion principle. For example the Ω^-
236 particle is comprised of three s quarks which would have exactly the same quantum
237 states.

238 The first one to present the idea of colour was Greenberg already in 1964 [12].
239 In 1971 Gell-Mann and Frtizsch presented their model, which solved the antisym-
240 metry problem. They added a colour quantum number to quarks, which separated
241 quarks of the same species. In the new colour model the baryonic wave function
242 became

$$(qqq) \rightarrow (q_r q_g q_b - q_g q_r q_b + q_b q_r q_g - q_r q_b q_g + q_g q_b q_r - q_b q_g q_r), \quad (1)$$

243 The colour model was also supported by experimental evidence. The decay
244 rate of a neutral pion with the addition of colours is

$$\Lambda(\pi^0 \rightarrow \gamma\gamma) = \frac{\alpha^2}{2\pi} \frac{N_c^2}{3^2} \frac{m_\pi^3}{f_\pi^2}. \quad (2)$$

245 For $N_c = 3$ this gives 7.75eV and the measured value is (7.86 ± 0.54) eV [13].

246 Another observable that combines the colour information also to the number
247 of quark flavours is The Drell-Ratio R [14]

$$R = \frac{\sigma(e^+ + e^- \rightarrow \text{hadrons})}{\sigma(e^+ + e^- \rightarrow \mu^+ + \mu^-)} = N_c \sum_f Q_f^2. \quad (3)$$

248 This ratio has the numerical value 2 when including the three light quarks u , d
249 and s . When the collision energy reaches the threshold of heavy quark (c and
250 b) production processes this increases to $^{10}/3$ (for $f = u, d, s, c$) and $^{11}/3$ (for $f =$
251 u, d, s, c, b). The threshold of $t\bar{t}$ production, $\sqrt{s} \approx 350$ GeV has not been reached
252 so far by any e^+e^- colliders.

253 The colour model explained why no free quarks had been observed. Only colour
254 neutral states are possible. The simplest ways of producing a colour neutral object
255 are the combination of three quarks, and the combination of a quark-antiquark
256 pair. These are known as baryons and mesons.

257 After the addition of colour the main ingredients of QCD had been established.
258 The final quantum field theory of Quantum Chromodynamics formed quickly be-
259 tween 1972 and 1974. Main part of this was the work Gross, Wilczek, Politzer
260 and George did for non-abelian gauge field theories [15–19]. Gross, Wilczek and
261 Politzer received the Nobel Prize in Physics for their work. The role of gluons was
262 as a colour octet was presented by Fritzsch, Gell-Mann and Leutwyler in 1973 [20].
263 The theory had now 8 massless gluons to mediate the strong interaction.

264 However, these gluons had not been discovered. Indirect evidence of the ex-
265 istence had been seen as it was observed that only about half of the momentum
266 of protons was transported by the quarks [21]. Direct evidence should be seen in
267 electron-electron collisions as a third, gluonic, jet in addition to two quark jets.
268 Three jet events were first seen in 1979 at the PETRA accelerator at DESY [22–24].

269 1.1.2 Asymptotic Freedom

270 In Quantum Electrodynamics (QED) The electric charge is screened. In the
271 vicinity of a charge, the vacuum becomes polarized. Virtual charged particle-
272 antiparticle pairs around the charge are arranged so that opposing charges face

each other. Since the pairs also include an equal amount opposite charge compared to the original charge the average charge seen by an observer at a distance is smaller. When the distance to the charge increases the effective charge decreases until the coupling constant of QED reaches the fine-structure constant $\alpha = \frac{1}{137}$.

Contrary to QED QCD is a non-abelian theory. In other words the generators of the symmetry group of QCD, SU(3), do not commute. This has the practical consequence that gluons interact also with other gluons, whereas in QED the neutral carrier particles, photons, only interact with charged particles. There is screening also in QCD because of the colour charges, but in addition to that there is antiscreening because of the gluon interactions. In QCD the antiscreening effect is stronger than screening. For larger distances to the colour charge the coupling constant is larger. This explains why no free colour charges can be observed. When the distance between charges increases the interaction strengthens until it is strong enough to produce a new quark-antiquark pair.

On the other hand, at very small distances the coupling constant approaches 0. This is called asymptotic freedom. For large energies and small distances the coupling constant is negligible. In 1975 Collins [25] predicted a state where individual quarks and gluons are no longer confined into bound hadronic states. Instead they form a bulk QCD matter that Edward Shuryak called Quark-Gluon plasma in his 1980 review of QCD and the theory of superdense matter [26]. QGP can be seen as a separate state of matter. A schematic view of a phase diagram for QCD matter is shown in Fig. 1.

In the early universe at the age of 10^{-6} s after the Big Bang the conditions preferred the existence of QGP instead of hadronic matter. Nowadays bulk QCD matter, its properties and its phase transitions between hadronic matter and the quark-gluon plasma (QGP) can be explored in the laboratory, through collisions of heavy atomic nuclei at ultra-relativistic energies. The study of QCD matter at high temperature is of fundamental and broad interest. The phase transition in QCD is the only phase transition in a quantum field theory that can be probed by any present or foreseeable technology.

One important property of the QGP is the shear viscosity to entropy ratio, η/s . It is believed that this ratio has an universal minimum value of $1/4\pi \approx 0.8$, which holds for all substances. This limit would be reached in the strong coupling limit of certain gauge theories [28]. The temperature dependance of the ratio is shown in Fig. 2. The minimum value of η/s is found in the vicinity of the critical temperature, T_c [29]. Finding the η/s values in QGP matter would therefore also provide a way of determining the critical point of QCD matter.

The η/s value for the matter created in Au-Au collisions at RHIC ($\sqrt{s_{NN}}$) has been estimated to be 0.09 ± 0.015 [29], which is very close to the lowest value for a wide class of thermal quantum field theories [28] for all relativistic quantum field

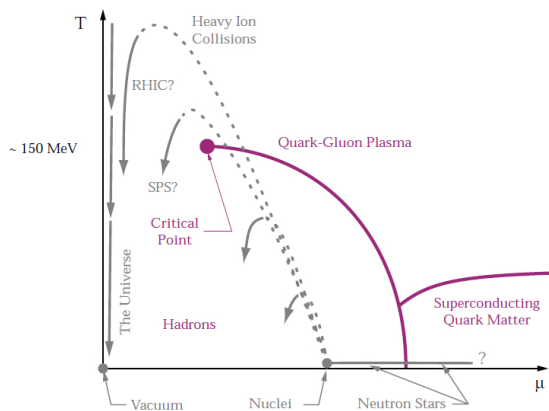


Figure 1: A schematic outline for the phase diagram of QCD matter at ultra-high density and temperature. The quark chemical potential μ that is on the x-axis represents the imbalance between quarks and antiquarks. At zero temperature this corresponds to the number of quarks but at higher temperatures there are also additional pairs of quarks and antiquarks. Along the horizontal axis the temperature is zero, and the density is zero up to the onset transition where it jumps to nuclear density, and then rises with increasing μ . Neutron stars are in this region of the phase diagram, although it is not known whether their cores are dense enough to reach the quark matter phase. Along the vertical axis the temperature rises, taking us through the crossover from a hadronic gas to the quark-gluon plasma. This is the regime explored by high-energy heavy-ion colliders. [27]

313 theories at finite temperature and zero chemical potential. This suggests that the
 314 the matter created goes through a phase where it is close to the critical point of
 315 QCD.

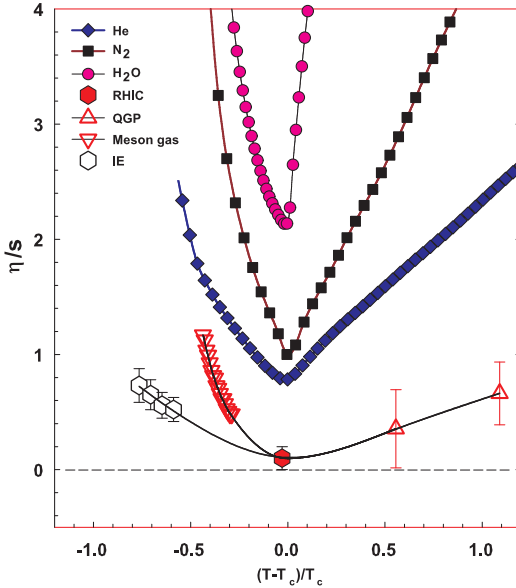


Figure 2: η/s as a function of $(T - T_c)/T_c$ for several substances as indicated. The calculated values for the meson-gas have an associated error of $\sim 50\%$. The lattice QCD value $T_c = 170$ MeV is assumed for nuclear matter. The lines are drawn to guide the eye. [29]

316 1.2 Heavy ion physics

317 The Quark Gluon Plasma (QGP) is experimentally accessible by colliding heavy
318 ions at high energies. Nowadays research of Heavy-Collisions is mainly performed
319 at two particle colliders; the The Relativistic Heavy Ion Collider (RHIC) at BNL
320 in New York, USA and he Large Hadron Collider (LHC) at CERN in Switzer-
321 land. Energy densities at these colliders should be enough to produce QGP and
322 convincing evidence of the creation has been seen at both colliders.

323 The development of heavy ion physics is strongly connected to the development
324 of particle colliders. Experimental study of relativistic heavy ion collisions has been
325 carried out for three decades, beginning with the Bevalac at Lawrence Berkeley
326 National Laboratory (LBNL) [30], and continuing with the AGS at Brookhaven
327 National Laboratory (BNL) [31], CERN SPS [32], RHIC at BNL and LHC at
328 CERN. The first colliders could not produce enough energy to create QGP matter
329 so they could only probe the hadronic state.

330 The collective motion of matter in a heavy-ion collision has been modeled using
331 several models e.g. the Blast wave Model [33] has been used successfully. Another
332 model growing in popularity is the hydrodynamical approach which is further
333 discussed in section 1.3.3.

334 1.2.1 History

335 The first heavy-ion collisions were done at the Bevalac experiment at the Lawrence
336 Berkeley National Laboratory [30] and at the Joint Institute for Nuclear Research
337 in Dubna [34] at energies up to 1GeV per nucleon. In 1986 the Super Proton
338 Synchrotron (SPS) at CERN started to look for QGP signatures in O+Pb col-
339 lisions. The center-of-mass energy per colliding nucleon pair ($\sqrt{s_{NN}}$) was 19.4
340 GeV [32]. These experiments did not find any decisive evidence of the existence
341 of QGP. In 1994 a heavier lead (Pb) beam was introduced for new experiments
342 at $\sqrt{s_{NN}} \approx 17$ GeV. At the same time the Alternating Gradient Synchrotron
343 (AGS) at BNL, Brookhaven collided ions up to ^{32}S with a fixed target at energies
344 up to 28GeV [31]. Although the discovery of a new state of matter was reported
345 at CERN, these experiments provided no conclusive evidence of QGP. Now SPS
346 is used with 400 GeV proton beams for fixed-target experiments, such as the SPS
347 Heavy Ion and Neutrino Experiment (SHINE) [35], which tries to search for the
348 critical point of strongly interacting matter.

349 The Relativistic Heavy Ion Collider (RHIC) at BNL in New York, USA started
350 its operation in 2000. The top center-of-mass energy per nucleon pair at RHIC, 200
351 GeV, was reached in the following years. The results from the experiments at RHIC
352 have provided a lot of convincing evidences that QGP was created [1,2,36,37]. The
353 newest addition to the group of accelerators capable of heavy-ion physics is the

³⁵⁴ Large Hadron Collider (LHC) at CERN, Switzerland. LHC started operating in
³⁵⁵ November 2009 with proton-proton collisions. First Pb-Pb heavy ion runs started
³⁵⁶ in November 2010 with $\sqrt{s_{NN}} = 2.76$ TeV, over ten times higher than at RHIC.
³⁵⁷ Among the six experiments at LHC, the Large Ion Collider Experiment (ALICE)
³⁵⁸ is dedicated to heavy ion physics. Also CMS and ATLAS have active heavy ion
³⁵⁹ programs.

360 **1.3 Features of Heavy-Ion Collisions**

361 **1.3.1 Collision Geometry**

362 In contrast to protons atomic nuclei are objects with considerable transverse size.
363 The properties of a heavy-ion collision depend strongly on the impact parameter
364 b which is the vector connecting the centers of the two colliding nuclei at their
365 closest approach. One illustration of a heavy-ion collision is shown in Fig. 3.

366 Impact parameter defines the reaction plane which is the plane spanned by b
367 and the beam direction. Ψ_{RP} gives the angle between the reaction plane and some
368 reference frame angle. Experimentally the reference frame is fixed by the detector
369 setup. Reaction plane angle cannot be directly measured in high energy nuclear
 collisions, but it can be estimated with the event plane method [38].

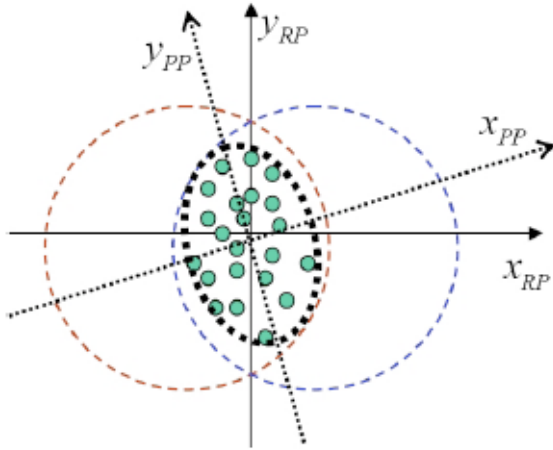


Figure 3: The definitions of the Reaction Plane and Participant Plane coordinate systems [39]. The dashed circles represent the two colliding nuclei and the green dots are partons that take part in the collision. x_{PP} and x_{RP} are the participant and reaction planes. The angle between x_{RP} and x_{PP} is given by Eq. (4). y_{PP} and y_{RP} are lines perpendicular to the participant and reaction planes.

370
371 Participant zone is the area containing the participants. The distribution of
372 nucleons in the nucleus exhibits time-dependent fluctuations. Because the nucleon
373 distribution at the time of the collision defines the participant zone, the axis of
374 the participant zone fluctuates and can deviate from the reaction plane. The angle
375 between the participant plane and the reaction plane is defined by [40]

$$\psi_{PP} = \arctan \frac{-2\sigma_{xy}}{\sigma_y^2 - \sigma_x^2 + \sqrt{(\sigma_y^2 - \sigma_x^2)^2 + 4\sigma_{xy}^2}}, \quad (4)$$

376 where the σ -terms are averaged over the energy density.

$$\sigma_y^2 = \langle y^2 \rangle - \langle y \rangle^2, \sigma_x^2 = \langle x^2 \rangle - \langle x \rangle^2, \sigma_{xy} = \langle xy \rangle - \langle x \rangle \langle y \rangle \quad (5)$$

377 The impact parameter is one way to quantize the centrality of a heavy-ion
 378 collision but it is impossible to measure in a collision. It can be estimated from
 379 observed data using theoretical models, but this is always model-dependent and
 380 to compare results from different experiments one needs an universal definition for
 381 centrality. The difference between central and peripheral collisions is illustrated
 382 in Fig. 4. In a central collision the overlap region is larger than in a peripheral
 383 collision. Larger overlap region translates into a larger number of nucleons partici-
 384 pating in the collision, which in turn leads to a larger number of particles produced
 385 in the event.

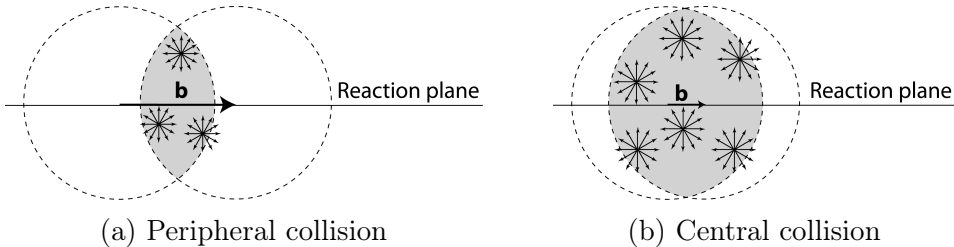


Figure 4: Interaction between partons in central and peripheral collisions. The snowflakes represent elementary parton-parton collisions. When the impact parameter b is large the number of elementary collisions is small. Particle production is small. Smaller impact parameter increases the number of elementary collisions. This increases particle production.

386 Usually centrality is defined by dividing collision events into percentile bins by
 387 the number participants or experimentally by the observed multiplicity. Centrality
 388 bin 0-5% corresponds to the most central collisions with the highest multiplicity
 389 and higher centrality percentages correspond to more peripheral collisions with
 390 lower multiplicities. A multiplicity distribution from ALICE measurements [41]
 391 illustrating the centrality division is shown in Fig. 5. The distribution is fitted
 392 using a phenomenological approach based on a Glauber Monte Carlo [42] plus a
 393 convolution of a model for the particle production and a negative binomial distri-
 394 bution.

395 1.3.2 Nuclear Geometry

396 To model heavy-ion collisions one must first have a description as good as possible
 397 of the colliding objects. Atomic nuclei are complex ensembles of nucleons. The
 398 nuclei used in heavy-ion physics have in the order of 200 nucleons. Mostly used

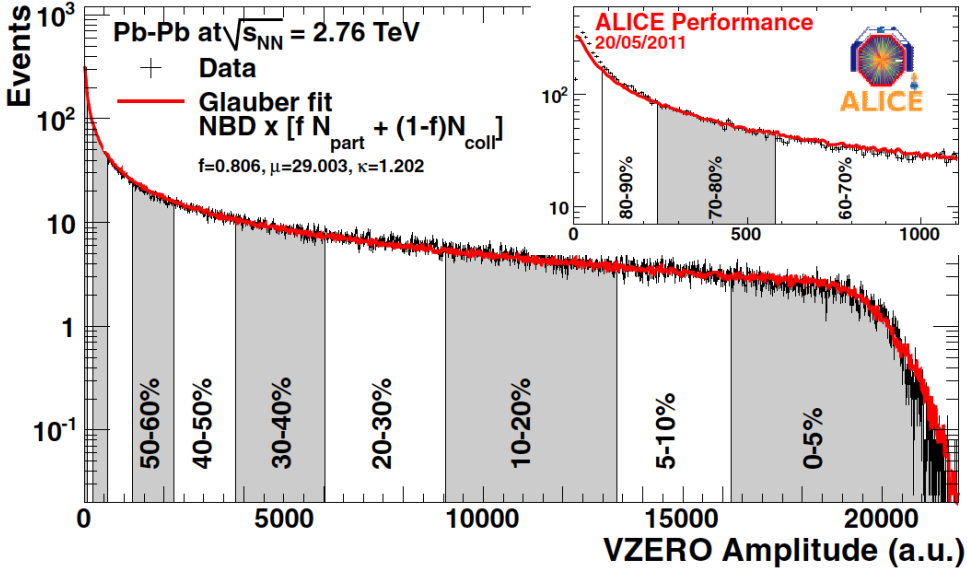


Figure 5: An illustration of the multiplicity distribution in ALICE measurements. The red line shows the fit of the Glauber calculation to the measurement. The data is divided into centrality bins [41]. The size of the bins corresponds to the indicated percentile.

³⁹⁹ nuclei are ²⁰⁸Pb at LHC and ¹⁹⁷Au at RHIC. The distribution of these nucleons
⁴⁰⁰ within a nucleus is not uniform and is subject to fluctuations in time.

⁴⁰¹ Nuclear geometry in heavy-ion collisions is often modelled with the Glauber
⁴⁰² Model. The model was originally developed to address the problem of high energy
⁴⁰³ scattering with composite particles. Glauber presented his first collection of papers
⁴⁰⁴ and unpublished work in his 1958 lectures [43]. In the 1970's Glauber's work
⁴⁰⁵ started to have utility in describing total cross sections. Maximon and Czyz applied
⁴⁰⁶ it to proton-nucleus and nucleus-nucleus collisions in 1969 [44].

⁴⁰⁷ In 1976 [45] Białas, Bleszyński, and Czyz applied Glauber's approach to
⁴⁰⁸ inelastic nuclear collisions. Their approach introduced the basic functions used in
⁴⁰⁹ modern language including the thickness function and the nuclear overlap function.
⁴¹⁰ Thickness function is the integral of the nuclear density over a line going through
⁴¹¹ the nucleus with minimum distance s from its center

$$T_A(s) = \int_{-\infty}^{\infty} dz \rho(\sqrt{s^2 + z^2}). \quad (6)$$

⁴¹² This function gives the thickness of the nucleus, i.e. the amount material seen by
⁴¹³ a particle passing through it.

⁴¹⁴ Overlap function is an integral of the thickness functions of two colliding nuclei
⁴¹⁵ over the overlap area. This can be seen as the material that takes part in the
⁴¹⁶ collision. It is given as a function of the impact parameter b

$$T_{AB}(b) = \int ds^2 T_A(\bar{s}) T_B(\bar{s} - \bar{b}) \quad (7)$$

⁴¹⁷ The average overlap function, $\langle T_{AA} \rangle$, in an A-A collisions is given by [46]

$$\langle T_{AA} \rangle = \frac{\int T_{AA}(b) db}{\int (1 - e^{-\sigma_{pp}^{inel} T_{AA}(b)}) db}. \quad (8)$$

⁴¹⁸ Using $\langle T_{AA} \rangle$ one can calculate the mean number of binary collisions

$$\langle N_{coll} \rangle = \sigma_{pp}^{inel} \langle T_{AA} \rangle, \quad (9)$$

⁴¹⁹ where the total inelastic cross-section, σ_{pp}^{inel} , gives the probability of two nucleons
⁴²⁰ interacting. The number of binary collisions is related to the hard processes in a
⁴²¹ heavy-ion collision. Each binary collision has equal probability for direct produc-
⁴²² tion of high-momentum partons. Thus the number of high momentum particles is
⁴²³ proportional to $\langle N_{coll} \rangle$.

⁴²⁴ Soft production on the other hand is related to the number of participants.
⁴²⁵ It is assumed that in the binary interactions participants get excited and further
⁴²⁶ interactions are not affected by previous interactions because the time scales are
⁴²⁷ too short for any reaction to happen in the nucleons. After the interactions ex-
⁴²⁸ cited nucleons are transformed into soft particle production. Production does not
⁴²⁹ depend on the number of interactions a nucleon has gone through. The average
⁴³⁰ number of participants, $\langle N_{part} \rangle$ can also be calculated from the Glauber model

$$\begin{aligned} \langle N_{part}^{AB}(b) \rangle &= \int ds^2 T_A(\bar{s}) \left[1 - \left[1 - \sigma_{NN} \frac{T_B(\bar{s} - \bar{b})}{B} \right]^B \right] \\ &+ \int ds^2 T_B(\bar{s}) \left[1 - \left[1 - \sigma_{NN} \frac{T_A(\bar{s} - \bar{b})}{A} \right]^A \right]. \end{aligned} \quad (10)$$

⁴³¹ Glauber calculations require some knowledge of the properties of the nuclei.
⁴³² One requirement is the nucleon density distribution, which can be experimen-
⁴³³ tally determined by studying the nuclear charge distribution in low-energy elec-
⁴³⁴ tron scattering experiments [42]. The nucleon density is usually parametrized by
⁴³⁵ a Woods-Saxon distribution

$$\rho(r) = \frac{\rho_0}{1 + \exp\left(\frac{r-R}{a}\right)}, \quad (11)$$

where ρ_0 is the nucleon density in center of the nucleus, R is the nuclear radius and a parametrizes the depth of the skin. The density stays relatively constant as a function of r until around R where it drops to almost 0 within a distance given by a .

Another observable required in the calculations is the total inelastic nucleon-nucleon cross-section $\sigma_{\text{inel}}^{\text{NN}}$. This can be measured in proton-proton collisions at different energies.

There are two often used approaches to Glauber calculations. The optical approximation is one way to get simple analytical expressions for the nucleus-nucleus interaction cross-section, the number of interacting nucleons and the number of nucleon-nucleon collisions. In the optical Glauber it is assumed that during the crossing of the nuclei the nucleons move independently and they will be essentially undeflected.

With the increase of computational power at hand the Glauber Monte Carlo (GMC) approach has emerged as a method to get a more realistic description of the collisions. In GMC the nucleons are distributed randomly in three-dimensional coordinate system according to the nuclear density distributions. Also nuclear parameters, like the radius R can be sampled from a distribution. A heavy-ion collision is then treated as a series of independent nucleon-nucleon collisions, where in the simplest model nucleons interact if their distance in the plane orthogonal to the beam axis, d , satisfies

$$d < \sqrt{\sigma_{\text{inel}}^{\text{NN}}} \quad (12)$$

The average number of participants and binary collisions can then be determined by simulating many nucleus-nucleus collisions. The results of one GMC Pb-Pb event with impact parameter $b = 9.8\text{fm}$ is shown in Fig. 6

1.3.3 Hydrodynamical Modelling

The relativistic version of hydrodynamics has been used to model the deconfined phase of a heavy-ion collision with success. Heavy-ion collisions produce many hadrons going into all directions. It is expected that tools from statistical physics would be applicable to this complexity [47]. The power of relativistic hydrodynamics lies in its simplicity and generality. Hydrodynamics only requires that there is local thermal equilibrium in the system. In order to reach thermal equilibrium the system must be strongly coupled so that the mean free path is shorter than the length scales of interest [48].

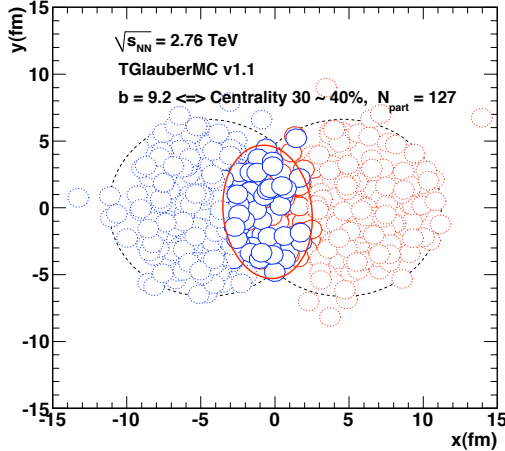


Figure 6: The results of one Glauber Monte Carlo simulation. Big circles with black dotted boundaries represent the two colliding nuclei. The participant zone is highlighted with the solid red line. Small red and blue circles represent nucleons. Circles with thick boundaries are participants i.e. they interact with at least one nucleon from the other nucleus. Small circles with dotted boundaries are spectators which do not take part in the collision.

469 The use of relativistic hydrodynamics in high-energy physics dates back to
 470 Landau [49] and the 1950's, before QCD was discovered. Back then it was used
 471 in proton-proton collisions. Development of hydrodynamics for the use of heavy-
 472 ion physics has been active since the 1980's, including Bjorken's study of boost-
 473 invariant longitudinal expansion and infinite transverse flow [?]. Major steps were
 474 taken later with the inclusion of finite size and and dynamically generated trans-
 475 verse size [?, ?], a part of which was done at the University of Jyväskylä. The role
 476 of hydrodynamics in heavy-ion physics was strengthened when QGP was observed
 477 to behave like a liquid by RHIC [1].

478 The evolution of a heavy-ion event can be divided into four stages. A schematic
 479 representation of the evolution of the collisions is shown in Fig. 7. Stage 1 follows
 480 immediately the collision. This is known as the pre-equilibrium stage. Hydrody-
 481 namic description is not applicable to this regime because thermal equilibrium is
 482 not yet reached. The length of this stage is not known but it is assumed to last
 483 about $1 \text{ fm}/c$ in proper time τ .

484 The second stage is the regime where thermal equilibrium or at least near-
 485 equilibrium is reached. In this stage hydrodynamics should be applicable if the
 486 temperature is above the deconfinement temperature [48]. This lasts about $5 -$
 487 $10 \text{ fm}/c$ until the temperature of the system sinks low enough for hadronization to

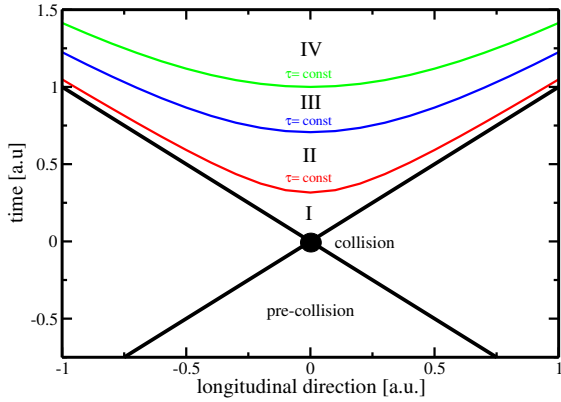


Figure 7: Schematic representation [48] of a heavy-ion collision as the function of time and longitudinal coordinates z . The various stages of the evolution correspond to proper time $\tau = \sqrt{t^2 - z^2}$ which is shown as hyperbolic curves separating the different stages.

488 occur. Now the system loses its deconfined, strongly coupled, state and hydrodynamics
 489 can no longer be used. The third stage is the hadron gas stage where the
 490 hadrons still interact. This ends when hadron scattering becomes rare and they
 491 no longer interact. In the final stage hadrons are free streaming and they fly in
 492 straight lines until they reach the detector.

493 The hydrodynamical approach treats the ensemble of particles as a fluid. It
 494 uses basic equations from hydrodynamics and thermodynamics but with a few
 495 modifications to account for the relativistic energies. The calculation is based
 496 on a collection of differential equations connecting the local thermal variables like
 497 temperature, pressure etc. to local velocities of the fluid. One also needs equations
 498 of state that connect the properties of the matter, e.g. temperature and pressure
 499 to density. Given initial conditions and equations of state the calculation gives the
 500 time-evolution of the system.

501 At first only ideal hydrodynamics was used. Ideal hydrodynamics does not
 502 include viscosity but it is a relatively good approximation and it could predict
 503 phenomena like elliptic flow. For more detailed calculations also viscosity must be
 504 considered and viscosity itself is an interesting property of QGP.

505 In this thesis I compare my results of identified particle flow to calculations from
 506 two hydrodynamical models; VISHNU model by Song *et al.* [50] and calculations
 507 by Niemi *et al.* [51].

508 1.4 Flow

509 In a heavy-ion collision the bulk particle production is known as flow. The pro-
 510 duction is mainly isotropic but a lot of studies including my thesis focus on the
 511 small anisotropies. After the formation of the QGP, the matter begins to expand
 512 as it is driven outwards by the strong pressure difference between the center of the
 513 collision zone and the vacuum outside the collision volume. The pressure-driven
 514 expansion is transformed into flow of low-momentum particles in the hadroniza-
 515 tion phase. Since the expansion is mainly isotropic the resulting particle flow is
 516 isotropic with small anisotropic corrections that are of the order of 10% at most.
 517 The isotropic part of flow is referred to as radial flow.

518 The transverse momentum spectra dN/dp_T in heavy-ion collisions is shown

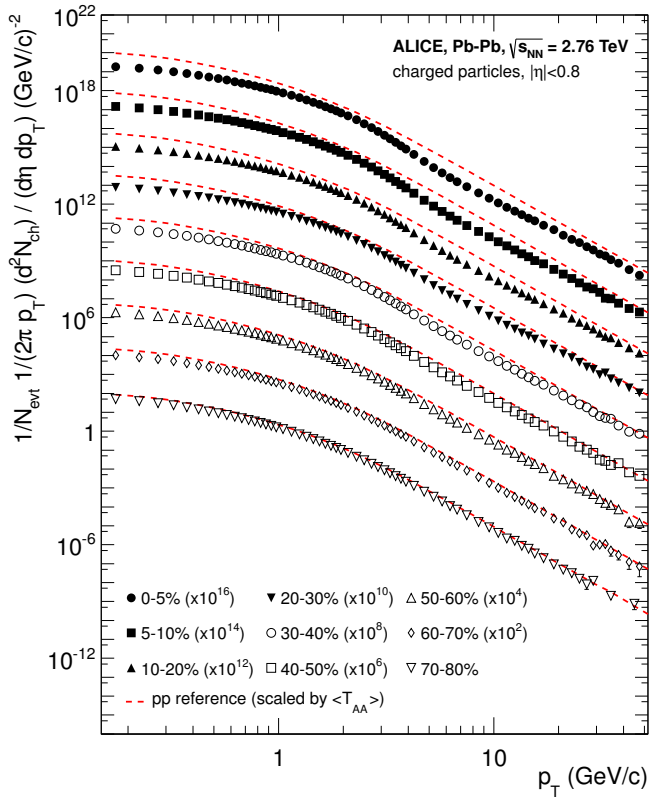


Figure 8: Charged particle spectra measured by ALICE [52] for the 9 centrality classes given in the legend. The distributions are offset by arbitrary factors given in the legend for clarity. The distributions are offset by arbitrary factors given in the legend for clarity. The dashed lines show the proton-proton reference spectra scaled by the nuclear overlap function determined for each centrality class and by the Pb-Pb spectra scaling factors [52].

519 in Fig. 8. The vast majority of produced particles have small p_T . The difference
 520 between the yield of 1 GeV/c and 4 GeV/c particles is already 2-3 orders of mag-
 521 nitude. Any observables that are integrated over p_T are therefore dominated by
 522 the small momentum particles.

523 1.4.1 Anisotropic Flow

524 In a non-central heavy-ion collision the shape of the impact zone is almond-like.
 525 In peripheral collisions the impact parameter is large which means a strongly
 526 asymmetric overlap region. In a central collision the overlap region is almost
 527 symmetric in the transverse plane. In this case the impact parameter is small.
 528 Collisions with different impact parameters are shown in Fig. 4.

529 The pressure gradient is largest in-plane, in the direction of the impact pa-
 530 rameter b , where the distance from high pressure, at the collision center, to low
 531 pressure, outside the overlap zone, is smallest. This leads to stronger collective
 532 flow into in-plane direction, which in turn results in enhanced thermal emission
 533 through a larger effective temperature into this direction, as compared to out-of-
 534 plane [3, 4, 53]. The resulting flow is illustrated in Fig. 9. Flow with two maxima
 535 in the direction of the reaction plane is called elliptic flow. This is the dominant

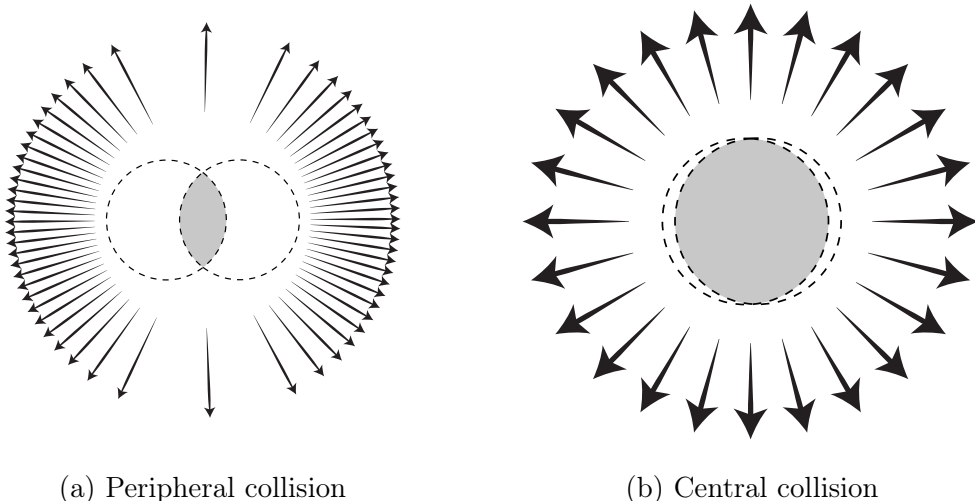


Figure 9: Illustration of flow in momentum space in central and peripheral collisions. The density of the arrows represent the magnitude of flow seen at a large distance from the collision in the corresponding azimuthal direction. In a peripheral collision momentum flow into in-plane direction is strong and flow into out-of-plane direction is weak. In a central collision anisotropy in flow is smaller, but the total yield of particles is larger.

part of anisotropic flow. Also more complex flow patterns can be identified. The most notable of these is the triangular flow, which is mainly due to fluctuations in the initial conditions.

Flow is nowadays usually quantified in the form of a Fourier composition

$$E \frac{d^3N}{dp^3} = \frac{1}{2\pi p_T} \frac{d^2N}{dp_T d\eta} \left(1 + \sum_{n=1}^{\infty} 2v_n(p_T, \eta) \cos(n(\phi - \Psi_n)) \right), \quad (13)$$

where the coefficients v_n give the relative strengths of different anisotropic flow components and the overall normalisation gives the strength of radial flow. Elliptic flow is represented by v_2 and v_3 represents triangular flow. The first coefficient, v_1 , is connected to directed flow. This will however in total be zero because of momentum conservation. It can be nonzero in some rapidity or momentum regions but it must be canceled by other regions.

The first approaches to quantifying the anisotropy of flow did not use the Fourier composition. Instead they approached the problem with a classic event shape analysis using directivity [54] or sphericity [3, 55] to quantify the flow.

The first experimental studies of anisotropy were performed at the AGS [56] in 1993. They noted that the anisotropy of particle production in one region correlates with the reaction plane angle defined in another region.

The first ones to present the Fourier decomposition were Voloshin and Zhang in 1996 [57]. This new approach was useful for detecting different types of anisotropy in flow, since the different Fourier coefficients give different harmonics in flow. They also show the relative magnitude of each harmonic compared to radial flow.

Some parts of the Fourier composition approach were used for Au-Au collisions at $\sqrt{s_{NN}} = 11.4\text{GeV}$ at AGS in 1994 [58]. This analysis still focused on event shapes but they constructed these shapes using Fourier composition from different rapidity windows.

1.4.2 High p_T Phenomena

The measurement of anisotropic flow coefficients can be extended to very high transverse momenta p_T . High p_T measurements of v_2 from CMS [59] are shown in Fig. 16. For high transverse momenta v_2 values are positive and they decrease slowly as a function of p_T . At high transverse momentum the v_2 values don't, however, represent flow.

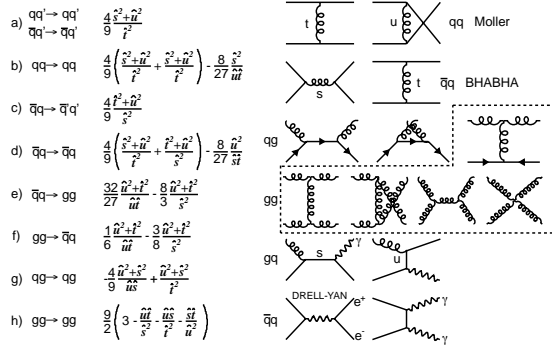


Figure 10: The basic pQCD processes and their quadratic matrix elements

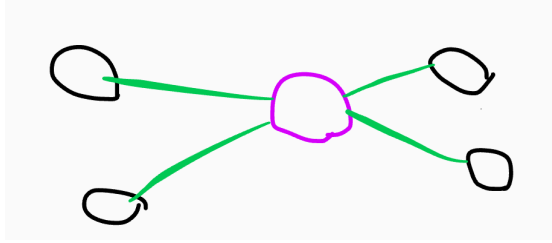


Figure 11: Schematic view of hard scattering process of $p + p \rightarrow 2 \text{jets}$

566 1.5 Hard processes

567 1.5.1 pQCD factorization

The term Hard Scattering is used in connection with the scattering of two point-like constituents (partons) of colliding nucleons, when the momentum transfer Q^2 is large ($Q \gg \Lambda_{\text{QCD}}$). Figure ?? shows the incoming partons, quarks or gluons, as they exchange a space-like virtual gluon and produce two highly virtual outgoing partons. The outgoing partons will eventually fragment into collimated showers of partons, referred to as jets

Jet fragmentation can be factorised into three components; the parton distribution functions f_a , f_b that give the probability of getting a parton with momentum fraction x of the proton, the cross section of the elementary scattering $ab \rightarrow cd$ (Fig. 10) and the fragmentation functions that give the probability of getting hadron h from the parton.

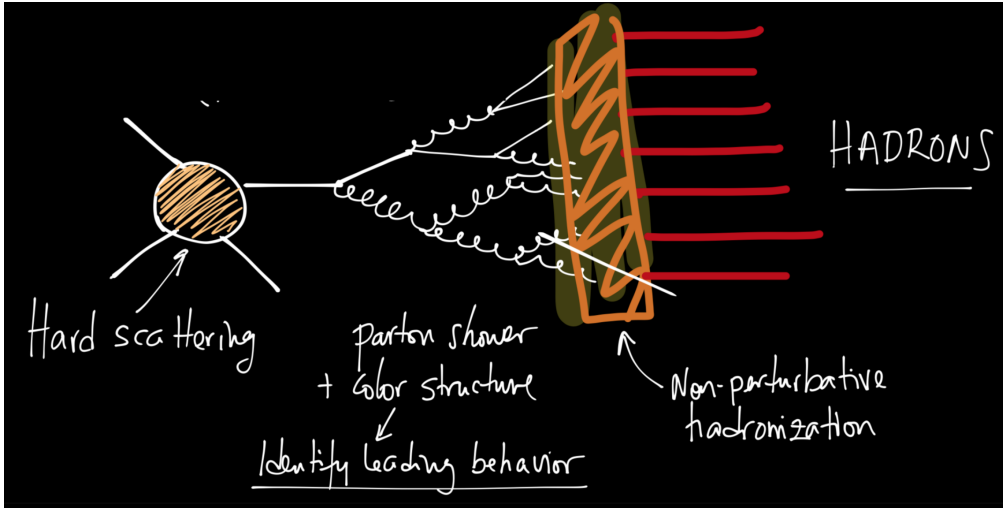


Figure 12: REPLACE FIGURE An illustration of jet showering. The highly virtual parton from the hard scattering will produce a shower of softer partons. When the virtuality is low enough the shower will go through a hadronisation process that produces the hadrons, which will be eventually observed in the detector.

$$\frac{d\sigma_{pp}^h}{dy d^2 p_T} = K \sum_{abcd} \int dx_a dx_b f_a(x_a, Q^2) f_b(x_b, Q^2) \frac{d\sigma}{dt} (ab \rightarrow cd) \frac{D_{h/c}^0}{\pi z_c}$$

$$x_a = \frac{|p_a|}{|p_{proton}|}$$

⁵⁷⁹ Parton Distribution Function

⁵⁸⁰ Parton Distribution Functions (PDFs) are essential to calculate the scattering cross
⁵⁸¹ section. They are extracted from comprehensive global analysis of experimental
⁵⁸² results from a variety of fixed-target and collider experiments. PDFs $f_a(x)$ give the
⁵⁸³ differential probability for parton a to carry momentum fraction x of the proton
⁵⁸⁴ momentum.

⁵⁸⁵ PDFs cannot be calculated from first principles. In practice the PDFs are
⁵⁸⁶ measured in Deeply Inelastic Scattering (DIS) experiments and are extrapolated
⁵⁸⁷ to the relevant momentum scales at LHC using the Dokshitzer-Gribov-Lipatov-
⁵⁸⁸ Altarelli-Parisi (DGLAP) evolution scheme [?] 14.

$$\mu_F^2 \frac{\partial f_i(x, \mu_F^2)}{\partial \mu_F^2} = \sum_j \frac{\alpha_s(\mu_F)}{2\pi i} \int_x^1 \frac{dz}{z} P_{ij}(z) f_j\left(\frac{x}{z}, \mu_F^2\right), \quad (14)$$

589 where μ_F is a factorization scale. The splitting functions P_{ij} describe a probability to radiate parton i from parton j as a function of the momentum fraction z carried away by the offspring parton.

592 The final component in the factorization, fragmentation functions, describe
 593 the distribution of the fractional momenta of particles radiated from the outgoing
 594 parton. Fragmentation function are given with respect to the momentum fraction
 595 z which is defined as the longitudinal momentum fraction of jet momentum p_{jet}
 596 carried away by the jet fragment p_{part}

$$z = \frac{\bar{p}_{\text{part}} \cdot \bar{p}_{\text{jet}}}{p_{\text{jet}}^2} = \frac{p_{\text{part}}}{p_{\text{jet}}} \Big|_{\bar{p}_{\text{part}} \times \bar{p}_{\text{jet}} = 0} \quad (15)$$

597 Fragmentation function $D(z)$ then gives the average multiplicity m of jet fragments having $z > z_0$ [].

$$m(z_0) = \int_{z_0}^1 D(z) dz \Rightarrow m(0) \equiv \langle m \rangle = \int_0^1 D(z) dz \quad (16)$$

599 Because of momentum conservation the sum of all jet fragments must be equal
 600 to the jet momentum, i.e.

$$\sum p_{i,\text{part}} = p_{\text{jet}} \Rightarrow \sum z_i = 1 \Rightarrow \int_0^1 z D(z) dz = 1 \quad (17)$$

601 A natural consequence is that the average momentum fraction is the inverse of
 602 the average multiplicity

$$\langle z \rangle = \frac{\int_0^1 z D(z)}{\int_0^1 D(z)} = \frac{1}{\langle m \rangle} \quad (18)$$

603 1.5.2 Jet hadronisation

604 When the parton shower reaches a scale close to Λ_{QCD} , the perturbative description
 605 is no longer valid. Thus the hadronisation stage must be described in a
 606 non-perturbative manner. One simple scenario that is used in several theory calculations
 607 is the so-called local parton-hadron duality [?]. In the local parton-hadron
 608 duality hypothesis it is assumed that there exists a low virtuality scale Q_0 in which
 609 the hadronisation happens, that is independent of the scale of the primary hard
 610 process. At this scale the partons are transformed into hadrons, assuming that the
 611 flow of momentum and quantum numbers for the hadrons can be directly obtained
 612 from those of partons introducing only small normalising constants.

613 Hadronisation is assumed to be universal, i.e. it shouldn't depend on the
 614 collision energy or system.

615 **Lund string model**

616 One common implementation in MC generators is the Lund string fragmentation
 617 algorithm [?]. The string model is based on the fact that in QCD linear confinement
 618 is expected over large distances [?]. This can be modelled by imagining a colour
 619 flux tube being stretched between the outgoing partons. The left side of Fig. 14
 620 illustrates this point for a $q\bar{q}$ -pair. The tube is assumed to have a uniform fixed
 621 transverse size of about 1 fm along its length, which leads to a linearly rising
 622 potential $V(r) = \kappa r$, where the string constant κ describes the amount of energy
 623 per unit length. A value of $\kappa \approx 1\text{GeV/fm} \approx 0.2\text{GeV}^2$ can be obtained from hadron
 624 mass spectroscopy.

625 The evolution of string fragmentation is illustrated schematically on the right
 626 side of Fig. 14. This figure is drawn in a light cone presentation, so the initial
 627 quark and antiquark are going to separate directions at the speed of light, which
 628 assumes them as massless. The string between them, illustrated in the figure by
 629 the red line, stretches until its potential energy becomes high enough that it can
 630 break, forming a new quark-antiquark pair. If the original pair was $q\bar{q}$ and the
 631 new pair $q'\bar{q}'$, now two new pairs $q\bar{q}'$ and $q'\bar{q}$ have formed. As these particles
 632 are also moving away from each other, the strings between them can stretch and
 633 break, creating yet more pairs. The process continues until the invariant mass of
 634 the system connected by the string becomes small enough and a final state meson
 635 is formed.

636 To mathematically model the string one can use a massless relativistic string
 637 with no transverse degrees of freedom. The gluons are represented as energy and
 638 momentum carrying kinks on the string with incoherent sums of one colour charge
 639 and one anticolour charge. When this string breaks, it is classically required that
 640 the created quark and antiquark are produced at a certain distance if they are to
 641 have any mass or transverse momentum. However, taking into account quantum
 642 mechanics, the pair must be created at one point and then tunnel out to the
 643 classically allowed region. Thus the probability to create a new quark-antiquark
 644 pair becomes proportional to the tunnelling probability [?].

$$P_{\text{tunnelling}} \propto \exp\left(\frac{-\pi m_\perp^2}{\kappa}\right) = \exp\left(\frac{-\pi m^2}{\kappa}\right) \left(\frac{-\pi p_\perp^2}{\kappa}\right), \quad (19)$$

645 where the transverse mass m_\perp is defined as $m_\perp^2 = m^2 + p_\perp^2$. The transverse
 646 momentum is now defined to be transverse to the string axis. This formula gives
 647 flavour-independent Gaussian p_\perp -distribution for the created $q\bar{q}$ pairs.

648 As explained above the string fragmentation would only produce mesons in
 649 the final state, but we know that also baryons are created in the process. In the
 650 string fragmentation model baryon production is included by adding a probability
 651 that a diquark-antidiquark pair is created instead of a quark-antiquark pair when

652 a string breaks.

653 The kinematics of each string breaking are determined iteratively. Since there
654 is no natural ordering, the string breaking can be considered in any order and
655 the answer obtained must be the same. One can start from the q leg and work
656 one's way to the \bar{q} leg, or vice versa. This give a left-right symmetry of the
657 string fragmentation. In the Lund model this is taken into account by defining a
658 symmetric fragmentation function

$$f(z) \propto \frac{1}{z} (1-z)^a \exp\left(-\frac{bm_{\perp}^2}{z}\right) \quad (20)$$

659 to break the string into a hadron and a remainder system. In the function z is
660 the fraction of light-cone momentum p^+ given to the hadron in the string breaking,
661 m_{\perp} is the transverse mass of the hadron and a and b are tuneable parameters of
662 the model. For heavy quarks this has to be modified as

$$f(z) \propto \frac{1}{z^{1+bm_Q^2}} (1-z)^a \exp\left(-\frac{bm_{\perp}^2}{z}\right) \quad (21)$$

663 The process can be thought as follows: first start from the q-leg of a $q\bar{q}$ system
664 and choose to consider the breaking to new $q'\bar{q}'$ pair closest to this leg. Now the
665 breaking will produce a hadron $q\bar{q}'$ and a remainder system spanning from $q'\bar{q}$.
666 Then the process is continued until the \bar{q} -leg is reached. A small detail here is
667 that in equation (20) it is assumed that the mass of the remainder system is large.
668 Thus some patching up is needed for the last two hadrons coming from a string.
669 The patching up is done such that the place where it happens looks as closely like
670 any other string break as possible.

671 One additional possibility one must consider is that a string can have such a
672 low mass that it cannot break at all. In this case a single hadron is generated out
673 of the string and if necessary energy and momentum are exchanged with other
674 partons in the event.

675 After all the hadrons are produced, the short-lived ones can still decay before
676 the set of final state particles in the simulation is obtained []

677 Cluster model

678 Instead of a string model HERWIG [] uses a cluster model [?] for hadronisation.
679 The advantage of cluster models is that they require a smaller number of param-
680 eters than string models. The model is based on the preconfinement property of
681 parton showers, i.e. the colour structure of the shower at any evolution scale Q_0 is
682 such that colour singlet combinations of partons can be formed with an asymptot-
683 ically universal invariant mass distribution. The invariant mass does not depend

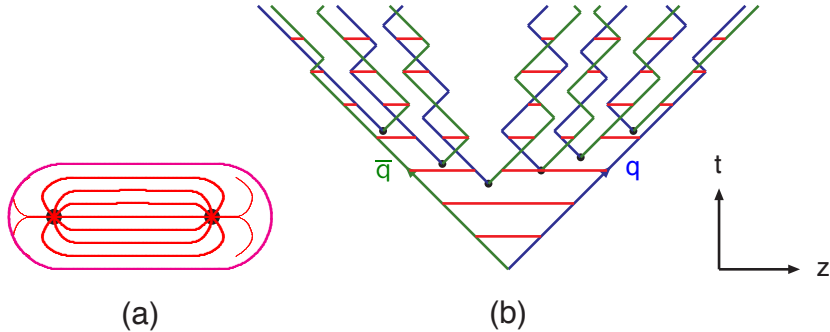


Figure 13: (a) A flux tube spanned between a quark and an antiquark. (b) The motion and breakup of a string system, with the two transverse degrees of freedom suppressed (diagonal lines are (anti)quarks, horizontal ones snapshots of the string field). [?]

684 on the initial hard process scale Q , but only on Q_0 and the QCD scale Λ_{QCD} , when
 685 $Q \gg Q_0$.

686 The cluster model starts from transforming all gluons non-perturbatively into
 687 $q\bar{q}$ pairs, which requires that the gluons get a mass, which must be at least twice
 688 the lightest quark mass. After the gluons are transformed into quarks, the adjacent
 689 colour lines can be clustered together to colour singlet states with mesonic quantum
 690 numbers. The momentum of these clusters is defined to be the sum of the momenta
 691 of the clustering partons. According to preconfinement, the mass distribution of
 692 these clusters is independent of the details of the hard scattering. Additionally the
 693 clusters can be regarded as highly excited hadron resonances and decayed into the
 694 final state hadrons.

695 Some of these initial clusters are too heavy to reasonably describe an excited
 696 state of a hadron. These must be split before they are allowed to decay. The
 697 cluster C is split if its mass fulfills the condition []

$$M_C^p \geq M_{\max}^p + (m_1 + m_2)^p, \quad (22)$$

698 where $m_{1,2}$ are the masses of the constituents partons of the cluster and M_{\max}
 699 and p are the main parameters of the model. These have to be chosen separately
 700 for clusters containing light, charmed and bottom quarks. When a cluster is split,
 701 a pair of light quarks is generated from the vacuum and two new clusters are made,
 702 both containing one quark from the original cluster and one from the newly gen-
 703 erated pair. The splitting is continued until no clusters with masses M_C fulfilling
 704 the equation 22 remains.

705 When are clusters are light enough, they decay into final state hadrons. If
 706 the mass of the cluster is high enough for decaying into a baryon-antibaryon pair,

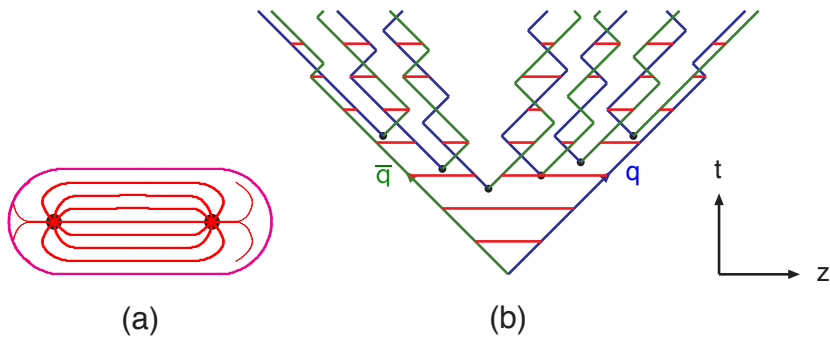


Figure 14: Colour structure of a parton shower to leading order in N_c . [?]

there is a parameter deciding whether the cluster undergoes mesonic or baryonic decay. For a mesonic decay a quark-antiquark pair is created from the vacuum and for the baryonic decay a diquark-antidiquark pair is made. Then the exact decay products are chosen and the cluster decays isotropically in the rest frame of the cluster. If there are partons produced in the perturbative phase involved in the decay, they retain their original direction in the cluster rest frame, up to some Gaussian smearing. If the cluster mass is too low to decay into a pair of mesons, it decays into the lightest possible hadron and some energy and momentum is exchanged with the adjacent clusters. At the end we are left with the final state hadrons, some of which might still decay until the end of the simulation if they are very short-lived. []

1.5.3 Jet energy loss

"Jet quenching in heavy-ion collisions evolves multi-scale problems [?, ?]. The elementary scattering and the subsequent branching process down to non-perturbative scales are dominated by hard scales in the vacuum as well as in the medium. Soft scales, of the order of the temperature of the medium, characterise the interactions of soft partons produced in the shower with the QGP. Soft scales also rule hadronisation, which is expected to take place in vacuum for sufficiently energetic probes, even though some modifications can persist from modifications of color flow [?, ?, ?]. Understanding the contributions from the different processes to the jet shower evolution in medium and their scale dependence is crucial to constrain the dynamics of jet energy loss in the expanding medium, the role of colour coherence [?], and fundamental medium properties like temperature dependent transport coefficient [?, ?]. "

High momentum particles are very rare and they are only produced in the initial collisions. After they are created they escape the medium before a thermal equilibrium is reached. Thus they are not part of the pressure-driven collective

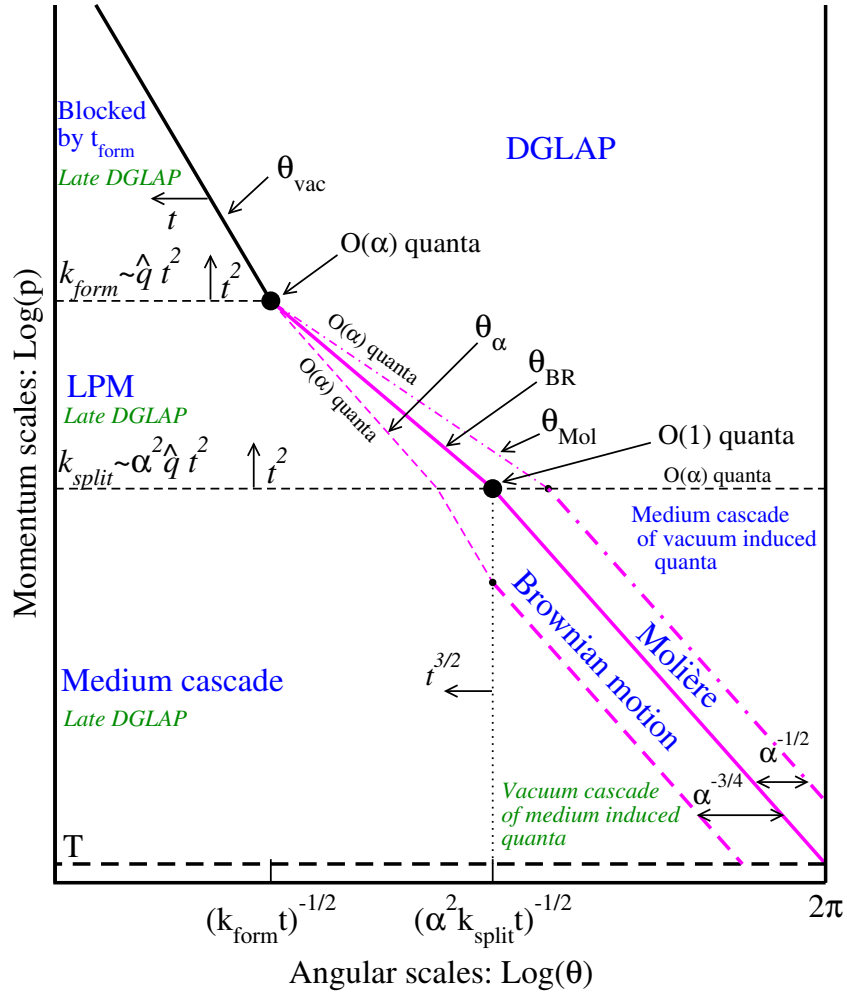


Figure 15: Parametrically accurate picture of how a medium-modified parton cascade fills the phase space. At time t , quanta can be formed up to momentum scale k_{form} and they are formed with $O(1)$ probability per $\log p$ at lower scale k_{split} . Quanta below k_{split} split further and their energy cascades to the thermal scale T in less than an epoch t . Transverse Brownian motion moves quanta up to the angle $\theta_{\text{BR}}(p)$ denoted by the thick purple line. The Molière region at larger θ is dominated by rare large angle scattering. At even larger angle, there are $O(\alpha_s)$ quanta per double logarithmic phase space from DGLAP ‘vacuum’ radiation, and for momenta below k_{split} these cascade within time t to T . After the jet escapes the medium, the jet and the emitted fragments will undergo vacuum radiation. This late time vacuum radiation emitted by the original parton dominates at sufficiently small $\log \theta$ (regions marked “late DGLAP” and bounded by θ_{vac} and θ_α), whereas the late time radiation of the fragments dominates in the region denoted by “Vacuum cascade of the medium induced quanta”. [?].

⁷³⁴ expansion. Instead high momentum yield is suppressed because of energy loss in
⁷³⁵ the medium. When propagating through the medium these partons lose energy as
⁷³⁶ they pass through the medium. This is referred to as jet quenching. Jet quenching
⁷³⁷ depends on the path lengths through the medium. Thus anisotropy in this region
⁷³⁸ is mainly dependent on the collision geometry and density of medium.

⁷³⁹ The energy loss of partons in medium is mainly due to QCD bremsstrahlung
⁷⁴⁰ and to elastic scatterings between the parton and the medium.

⁷⁴¹ The radiative energy loss mechanism is given in terms of the transport coef-
⁷⁴² ficient $\langle \hat{q} \rangle$, which describes the average momentum transfer between the medium
⁷⁴³ and parton [?]. The exact definition of this depends on the theoretical formalism
⁷⁴⁴ used to describe the energy loss mechanism.

⁷⁴⁵ Many of the energy loss models exploit the analogy between the QCD inter-
⁷⁴⁶ action of parton propagating through the colored medium and the QED energy
⁷⁴⁷ loss of electron propagating through material. An electron propagating through
⁷⁴⁸ matter loses its energy by photon Bremsstrahlung radiation. In the simplest case,
⁷⁴⁹ each individual scattering center results in a single emission of a photon. This is
⁷⁵⁰ known as the Bethe-Heitler regime [?]. The energy spectrum of radiated photons
⁷⁵¹ dN/dE is, in this case, proportional to $1/E$. However, the Bremsstrahlung photon,
⁷⁵² can be radiated only when the distance between the scattering centers is larger
⁷⁵³ than the formation length. In the limit, when the scattering centers are closer
⁷⁵⁴ than the formation length, the Bremsstrahlung process is suppressed. This phe-
⁷⁵⁵ nomenon is known as the Landau-Pomeranchuk-Migdal (LPM) [?, ?] suppression.
⁷⁵⁶ The radiated spectrum in this regime is proportional to $1/\sqrt{E}$.

⁷⁵⁷ Lower energy photons are further suppressed by the destructive interference
⁷⁵⁸ leading to the suppression of Bremsstrahlung photons of $E < \gamma\omega_p$, where ω_p is
⁷⁵⁹ the plasma frequency of the radiator. This is known as Dielectric suppression.
⁷⁶⁰ The photon energy distribution in this regime is proportional to the energy of the
⁷⁶¹ photon. A schematic view of the effect of these three regimes is shown in Fig. 17.

⁷⁶² The simplest energy loss process is elastic QCD scattering off the medium par-
⁷⁶³ tons. In elastic scatterings the recoil energy of the scattered partons are absorbed
⁷⁶⁴ by the thermal medium, which reduces the energy of the initial parton. The mean
⁷⁶⁵ energy loss from elastic scatterings can be estimated by

$$\langle \Delta E \rangle_{\text{el}} = \sigma \rho L \langle E \rangle_{1\text{scatt}} \propto L, \quad (23)$$

⁷⁶⁶ where σ is the interaction cross section and $\langle E \rangle_{1\text{scatt}}$ is the mean energy transfer
⁷⁶⁷ of one individual scattering [60]. This assumption holds if the mean energy is
⁷⁶⁸ independent of the total energy of the parton (E). The transport coefficient of
⁷⁶⁹ elastic scattering, $\langle \hat{q}_{\text{el}} \rangle = \langle \Delta E \rangle / L$, is defined as the mean energy loss per unit path
⁷⁷⁰ length.

⁷⁷¹ Another energy loss mechanism is medium-induced radiation. In QCD this

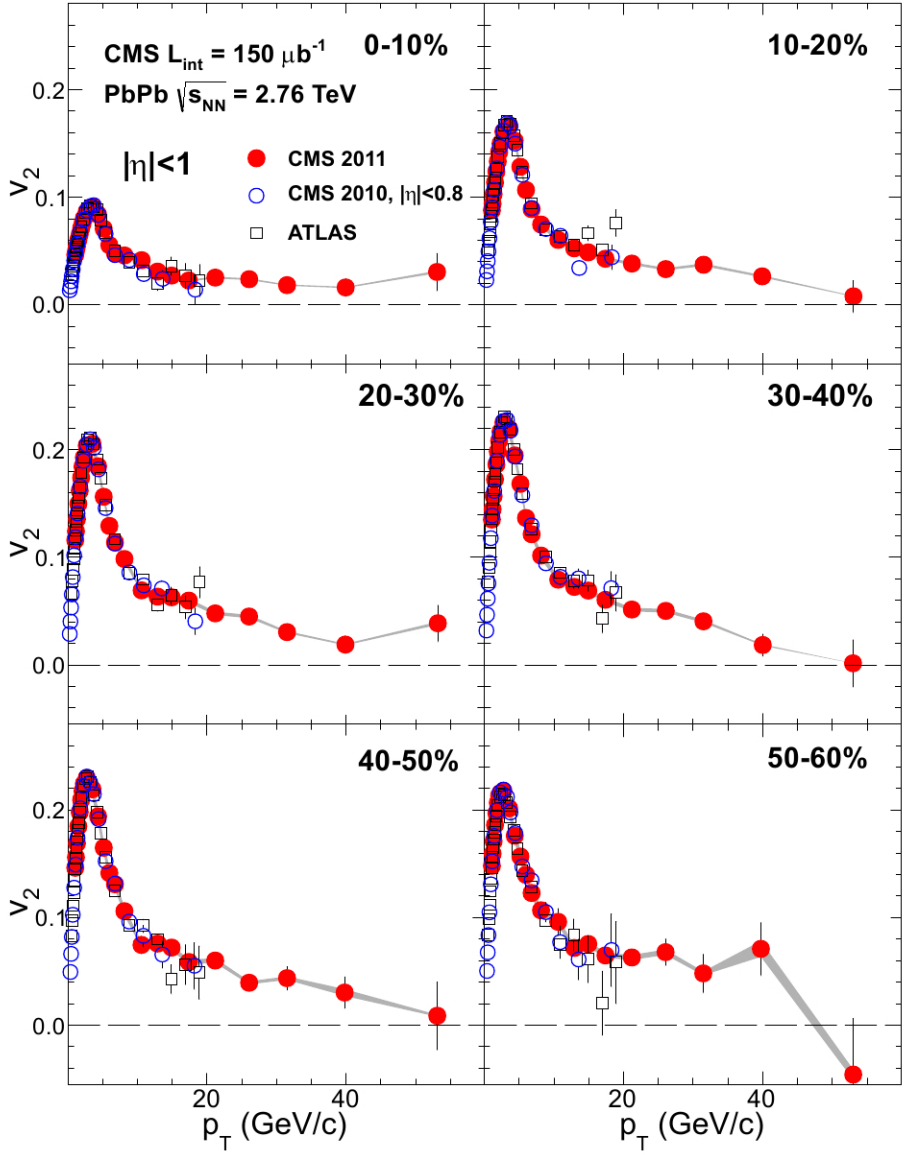


Figure 16: Elliptic flow, v_2 , as a function of the charged particle transverse momentum from 1 to 60 GeV/c with $|\eta| < 1$ for six centrality ranges in Pb-Pb collisions at $\sqrt{s_{NN}} = 2.76 \text{ TeV}$, measured by the CMS experiment. [59].

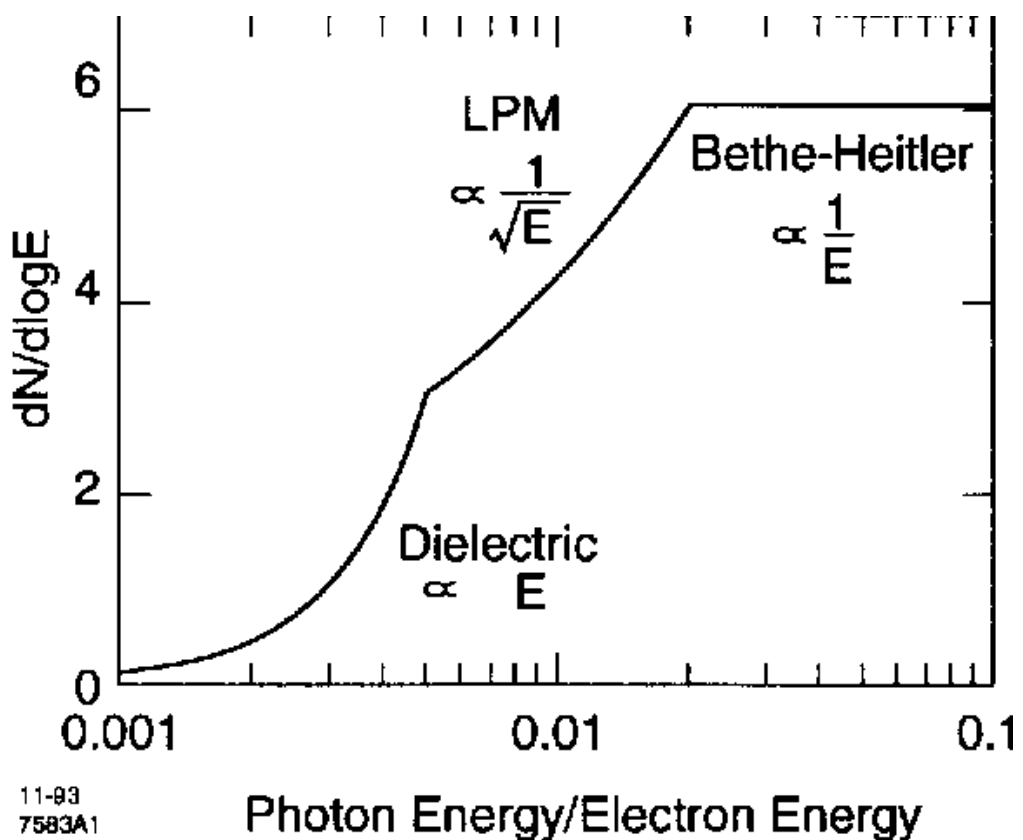


Figure 17: The expected bremsstrahlung spectrum for a electron propagating through material. [?].

772 radiation is mainly due to the elementary splitting processes, $q \rightarrow qg_r$ and $g \rightarrow gg_r$.
773 Assuming that the parton is moving with the speed of light radiation energy loss
774 can be estimated by

$$\langle \Delta E \rangle_{rad} \propto T^3 L^2, \quad (24)$$

775 where L is the length of the medium and T is its temperature [61]. The differ-
776 ent exponents of L in equations 23 and 24 indicate that radiative energy loss is
777 dominant over elastic energy loss.

778 There are several models that attempt to describe the nature of the energy loss
779 mechanism. The most used models can be divided into four formalisms.

780 In the Gyulassy-Levai-Vitev (GLV) [62] opacity expansion model the radiative
781 energy loss is considered on a few scattering centers N_{scatt} . The radiated gluon
782 is constructed by pQCD calculation as summing up the relevant scattering am-
783 plitudes in terms of the number of scatterings. Another approach into opacity
784 expansion is the ASW model by Armesto, Salgado and Wiedermann [63].

785 Thermal effective theory formulation by Arnold, Moore and Yaffe (AMY) [64]
786 uses dynamical scattering centers. It is based on leading order pQCD hard thermal
787 loop effective field theory. This model assumes that because of the high temper-
788 ature of the plasma the strong coupling constant can be treated as small. The
789 parton propagating through the medium will lose energy from soft scatterings and
790 hard scatterings.

791 The above models calculate the energy loss while the parton propagates through
792 the medium, focusing on the pQCD part. The higher twist (HT) approach by Wang
793 and Guo [65] implements the energy loss mechanism in the energy scale evolution
794 of the fragmentation functions.

795 The last category is formed by the Monte Carlo methods. The PYTHIA event
796 generator [66] is widely used in high-energy particle physics. Two Monte Carlo
797 models based on PYTHIA describing the energy loss mechanism are PYQUEN [67]
798 and Q-Pythia [68]. Other Monte Carlo models include JEWEL [69] and Ya-
799 JEM [70].

800 Jet quenching in heavy-ion collisions is usually quantized with the nuclear
801 modification factor R_{AA} , which is defined as

$$R_{AA}(p_T) = \frac{(1/N_{AA}^{evt}) dN^{AA}/dp_T}{\langle N_{coll} \rangle (1/N_{pp}^{evt}) dN^{pp}/dp_T} \quad (25)$$

802 where dN^{AA}/dp_T and dN^{pp}/dp_T are the yields in heavy-ion and proton-proton
803 collisions, respectively and $\langle N_{coll} \rangle$ is the average number of binary nucleon-nucleon
804 collisions in one heavy-ion event. The number of binary collisions can be calculated
805 from the Glauber model as shown in Sec. 1.3.2. From the point of view of direct

806 production a heavy-ion collision can be estimated relatively well to be only a series
 807 of proton-proton collisions.

808 If the medium has no effect on high p_T particles the nuclear modification factor
 809 should be 1. At RHIC and LHC this has been observed to be as low as 0.2 because
 810 of jet quenching. Measurements of R_{AA} from different sources are shown in Fig. 18

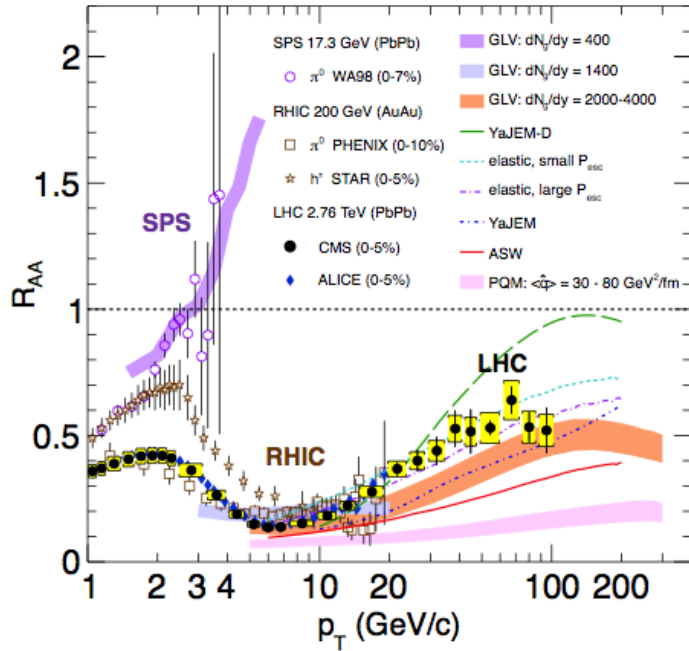


Figure 18: Measurements of the nuclear modification factor R_{AA} in central heavy-ion collisions at three different center-of-mass energies, as a function of p_T , for neutral pions (π^0), charged hadrons (h^\pm), and charged particles [71–75], compared to several theoretical predictions [32, 76–80]. The error bars on the points are the statistical uncertainties, and the yellow boxes around the CMS points are the systematic uncertainties. The bands for several of the theoretical calculations represent their uncertainties [81].

811 The nuclear modification factor can also be used to quantify anisotropy. In
 812 the study of anisotropy R_{AA} in-plane and out-of-plane can be compared. The
 813 distance traveled through medium is largest out-of-plane which leads to stronger
 814 suppression in this direction. The nuclear modification factor as a function of
 815 $\Delta\phi = \phi - \psi_n$ is given by

$$\begin{aligned}
R_{AA}(\Delta\phi, p_T) &= \frac{(1/N_{AA}^{evt}) d^2 N^{AA} / d\Delta\phi dp_T}{\langle N_{coll} \rangle (1/N_{pp}^{evt}) dN^{pp} / dp_T} \approx \frac{dN^{AA} / dp_T (1 + 2 \cdot v_2 \cos(2\Delta\phi))}{\langle N_{coll} \rangle dN^{pp} / dp_T} \\
&= R_{AA}^{incl}(p_T) (1 + 2 \cdot v_2 \cos(2\Delta\phi)). \tag{26}
\end{aligned}$$

816 The yield of proton-proton collisions is independent of the reaction plane and
817 the yield in heavy-ion collisions is modulated by the second harmonics. In Eq. (26)
818 R_{AA} is approximated only up to the second harmonics. From Eq. (26) it follows
819 that

$$\frac{R_{AA}(0, p_T) - R_{AA}(\pi/2, p_T)}{R_{AA}^{incl}(p_T)} \approx \frac{R_{AA}^{incl}(p_T) (1 + 2 \cdot v_2 - (1 - 2 \cdot v_2))}{R_{AA}^{incl}(p_T)} = 4 \cdot v_2 \tag{27}$$

820 The observed $R_{AA}(\Delta\phi, p_T)$ from PHENIX measurements in Au-Au collisions at
821 $\sqrt{s} = 200\text{GeV}$ [82] is compared to R_{AA} using v_2 via Eq. (26) in Fig. 19. They
822 agree very well within the statistical errors for all centrality and p_T bins.

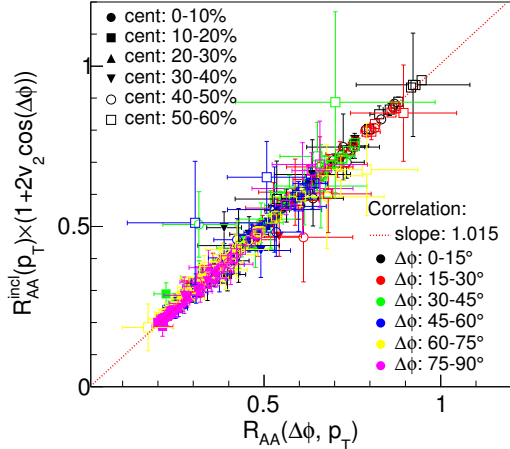


Figure 19: A comparison between observed $R_{AA}(\Delta\phi, p_T)$ and R_{AA} using v_2 from PHENIX measurements of Au-Au collisions at $\sqrt{s} = 200\text{GeV}$. On the X-axis is the measured $R_{AA}(\Delta\phi, p_T)$. On the y-axis is the inclusive R_{AA} multiplied by $1 + 2v_2 \cos(\Delta\phi)$ [82].

822 At high- p_T , the pQCD processes are dominant, hence the v_n (or $R_{AA}(\Delta\phi, p_T)$)
823 characterize the pathlength-dependence of the energy loss process.
824

825 Jet quenching is not the only high p_T phenomenon studied in heavy-ion collisions.
826 Another property is jet fragmentation. The high momentum parton created
827 in the initial collision fragments into a number of partons with smaller p_T . Jet
828 fragmentation occurs also in proton-proton collisions in the vacuum, but it can
829 be modified due to the presence of the medium. In order to study the jet frag-
830 mentation function ($D(z)$, where $z = p_T^h/p_T^{part}$) modification due the medium, we
831 use the two-particle correlations. The particle yield can be extracted from the
832 correlation function. The background from the flow processes is correlated and
833 needs to be subtracted to get the particle yield associated only with the jet. The
834 ratio of the jet yields in Au-Au and p-p collision $I_{AA} = Y^{Au+Au}/Y^{p+p}$ character-
835 izes the jet fragmentation modification [83]. I_{AA} probes the interplay between the
836 parton production spectrum, the relative importance of quark-quark, gluon-gluon
837 and quark-gluon final states, and energy loss in the medium.

838 **1.5.4 Monte Carlo Implementations**

839 **1.6 QGP in Small systems**

840 After the existence of QGP in heavy ion collisions has been established, attention
841 has been turned to small systems. Proton-proton (pp) and proton-Lead (pPb)
842 collisions have been studied at LHC and RHIC has studied a host of different
843 collision systems; namely proton-Gold (pAu), deuteron-Gold (dAu) and Helium³-
844 Gold (He³Au) collisions starting in 2000.

845 Already before the era of modern colliders, collective behaviour in proton-
846 proton collisions was considered by names like Heisenberg, Fermi and Bjorken. [84]
847 Eventually there were some experimental searches of QGP in pp and $p\bar{p}$ collisions
848 in E735 at Tevatron [85] and MiniMAX [86]. However no conclusive evidence was
849 found.

850 In the early years of RHIC these small systems were mostly considered as con-
851 trol measurement, for example in constraining nuclear modified parton distribution
852 functions (nPDFs) that determine the initial gluon distributions that determine
853 the first epoch of heavy ion collisions [87, 88].

854 In 2010 ultrahigh-multiplicity pp collisions were studied at CMS. The study
855 found that particles had a weak but clear preference to be emitted along a common
856 transverse ϕ angle across all rapidities [89]. This seemed like behaviour were sim-
857 ilar to AA collisions, but it was argued that it could as well come from momentum
858 correlations present in the earliest moments of the collision.

859 In 2012 LHC ran its first pPb data taking period. Around the same time
860 dAu data was reexamined at RHIC. Now it was revealed that most of the flow
861 signatures attributed to hydrodynamic expansion in AA collisions also existed in
862 smaller systems.

863 -Sub nucleonic structure needed to describe intial conditions in pA, pp

864 **1.6.1 Collective phenomena**

865 The most rugged analysis of collective behaviour concerns the two (or more) parti-
 866 cle correlations, often parametrised via the relative azimuthal angle and pseudora-
 867 pidity differences, $\Delta\phi$ and $\Delta\eta$ respectively. Figure 21 shows two-particle correla-
 868 tions measurements in PbPb, pPb and pp collisions at the LHC. In PbPb collisions
 869 long-range correlations dominate over short-range phenomena. This shows in the
 870 two ridges at $\Delta\phi = 0$ and $\Delta\phi = \pi$. At $\Delta\phi \approx \Delta\eta \approx 0$, there is a peak coming from
 871 single jet fragmentation. Since the away-side jet can be spread out in $\Delta\eta$, this
 872 contribution disappears when compared to the flow contribution at the away side
 873 ridge. In pPb, and pp the near side peak is more distinguished and the away-side
 874 jet contribution starts to show. Still, one can see long-range correlations that seem
 875 like flow-like collective behaviour in both systems.

876 In addition to the two particle correlations, correlations have been observed in
 877 the form of v_n coefficients both at LHC and at RHIC. The results have also been
 878 described with hydrodynamical models, although the applicability of said models
 879 is questionable, because of the large Reynolds numbers in small systems. Figure
 880 20 shows results for v_2 in different collisions systems at RHIC as measured by
 881 PHENIX. These different systems provide also different initial geometries. dAu
 882 collisions naturally have an ellipsoidal form, while a He3 collision has a triangular
 883 form and thus produces larger triangular flow, v_3 components.

884 Other observations that produce flow-like results include mass ordered v_2 coeffi-
 885 cients and higher order harmonics coming from fluctuations in the initial geometry.

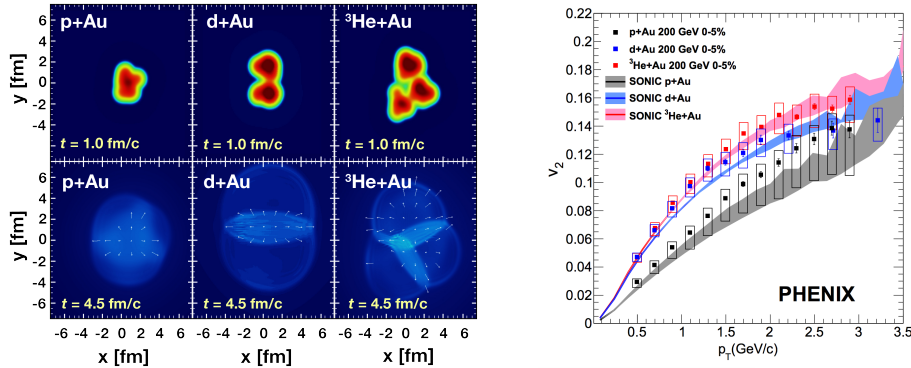


Figure 20: Calculations of the intial energy density in small collision systems at RHIC and the resulting hydrodynamic evolution.

886 Thus all the major collective flow phenomena observed in heavy-ion collisions have
 887 been also identified in small systems.

888 One open question is identifying the point the point, where flow-like correlations
 889 end. The question has proved challenging since low multiplicity events are
 890 dominated by non-flow phenomena. This makes observations in low multiplicity
 891 events model/method dependant. Different methods assess non-flow contributions
 892 differently. Thus some methods fail to observe a signal in cases, where others do
 893 and it is unclear whether this is true collective motion or it comes from non-flow
 894 contributions.

895 1.6.2 Absence of jet quenching

896 In A+A collisions, an important confirmation of the standard model comes from
 897 the energy loss of high p_T partons traversing the medium, referred to as jet quench-
 898 ing [90–92]. In 2003 the jet quenching effect was observed to disappear in d+Au
 899 collisions. This was taken as an indication that no QGP was created. Similarly at
 900 LHC no jet modification has been observed in pPb collisions. Fig. 22 shows the
 901 nuclear modification factor R_{pA} in pPb collisions as measured at the LHC.

902 The lack of jet modification seems surprising considering the multitude of flow
 903 observations supporting the existence of QGP in small systems. One possible
 904 explanation is simply the size of medium. In PbPb collision partons traversing
 905 through the medium lose energy to the medium. If the medium is very small there
 906 is limited time for interaction with the medium.

907 Calculations indicate that there should be modification in the most central
 908 pPb collisions, but selecting these in the analysis is complicated. In PbPb colli-
 909 sions most of the particle production comes from the medium and thus the total
 910 multiplicity is a good indicator of centrality. In pPb collisions, however the total
 911 multiplicity is smaller and is more strongly influenced by jet phenomena. Events

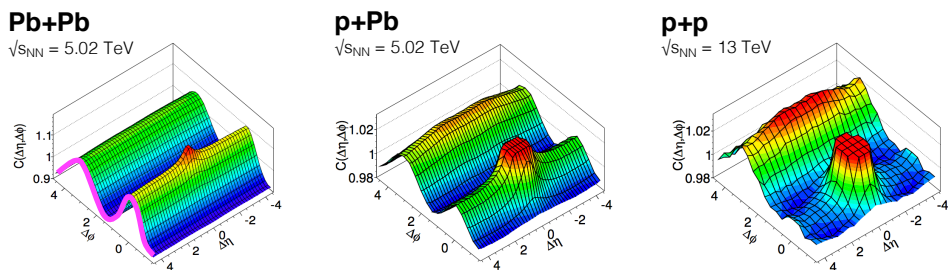


Figure 21: Two-particle correlation results in PbPb, pPb, and pp collisions at the LHC [1].

912 with jets have naturally larger multiplicities and are more likely to be classified as
 913 central events.

914 So far the only observable indicative of jet quenching in pPb collisions is the
 915 high $p_T v_2$. In heavy-ion collisions this is not explained by hydrodynamics. Instead
 916 it is assumed to come from jet quenching with different path lengths through the
 917 medium in different directions. In Fig.22 ATLAS and CMS measurements of v_2 in
 918 pPb and PbPb collisions are shown. The pPb results seem to follow a very similar
 919 pattern. But

Table 1: Summary of observations in small system

Observable	PbPb	pPb	pp
Jet RpA/RAA	Modified	No modification	-
Hadron RpA/RAA	Modified	No modification	-
Heavy flavors			
Jet shape	Broadening	No observations	-
Two-particle correlations	Ridge	Ridge	Ridge
v_2	Observed	Observed	Observed
Mass ordered flow			
Higher ordered harmonics			
High $p_T v_2$	Observed	Maybe	-

920 1.6.3 Centrality determination in small systems

921 In lead-lead collisions the total multiplicity of the event is a good indicator of the
 922 centrality of the collision. In proton-lead collisions the connection of multiplicity

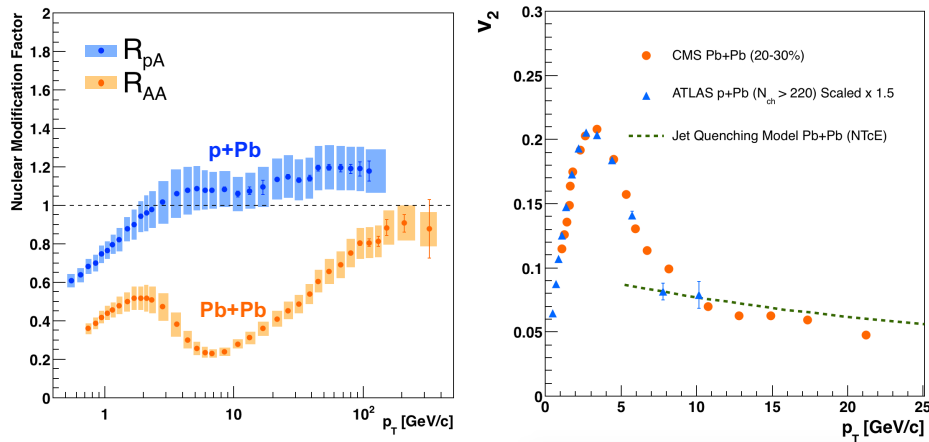


Figure 22: RpA in proton-lead collisions

ity and centrality is less clear. In p–Pb collisions the impact parameter is only loosely correlated to N_{part} or N_{coll} . Hence, although one uses traditionally the term centrality to refer to these measurements, the relevant parameters are N_{part} and N_{coll} [?].

The Glauber model [?] is generally used to calculate geometrical quantities of nuclear collisions (A–A or p–A). In this model, the impact parameter b controls the average number of participating nucleons N_{part} and the corresponding number of collisions N_{coll} . It is expected that variations of the amount of matter overlapping in the collision region will change the number of produced particles, and parameters such as N_{part} and N_{coll} have traditionally been used to describe those changes quantitatively, and to relate them to pp collisions.

The problem in p–Pb collisions, is that fluctuations in multiplicity coming from for example hard scatterings are of the same order as the differences in multiplicity between centrality classes. In Pb–Pb collisions these multiplicity fluctuations have little influence on the centrality determination, the range of N_{part} or N_{coll} is large and $P(M|v)$ converges quickly to a Gaussian with a small width relative to the range of v .

Thus in practice selecting high multiplicity one chooses not only large average N_{part} , but also positive multiplicity fluctuations leading to deviations from the binary scaling of hard processes. These fluctuations are partly related to qualitatively different types of collisions. High multiplicity nucleon-nucleon collisions show a significantly higher particle mean transverse momentum. They can be understood as harder collisions with larger momentum transfer Q^2 or as nucleon-nucleon collisions where multiple parton-parton interactions (MPI) take place.

Of particular interest are estimators from kinematic regions that are causally disconnected after the collision. The measurement of a finite correlation between them unambiguously establishes their connection to the common collision geometry. Typically these studies are performed with observables from well separated pseudorapidity (η) intervals, e.g. at zero-degree (spectators, slow-nucleons, deuteron break-up probability) and multiplicity in the rapidity plateau.

One centrality selection that is argued not to induce a bias on the binary scaling of hard processes is provided by the energy measurement with the Zero Degree Calorimeters (ZDC) in ALICE, due to their large η -separation from the central barrel detectors. They detect the "slow" nucleons produced in the interaction by nuclear de-excitation processes or knocked out by wounded nucleons.

-Multiplicity vs. centrality? -Auto-correlations in jet studies

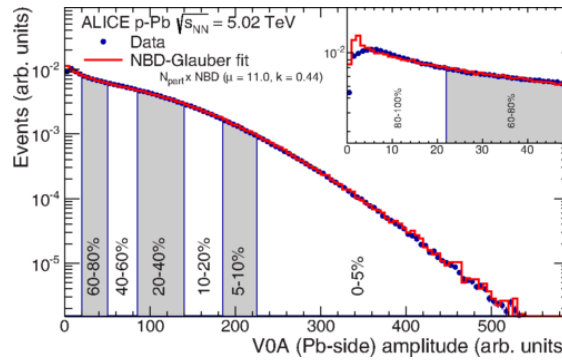


Figure 23: Distribution of the sum of amplitudes in the V0A hodoscopes (Pb-going), as well as the NBD-Glauber fit (explained in the text). Centrality classes are indicated by vertical lines. The inset shows a zoom-in on the most peripheral events. [?]

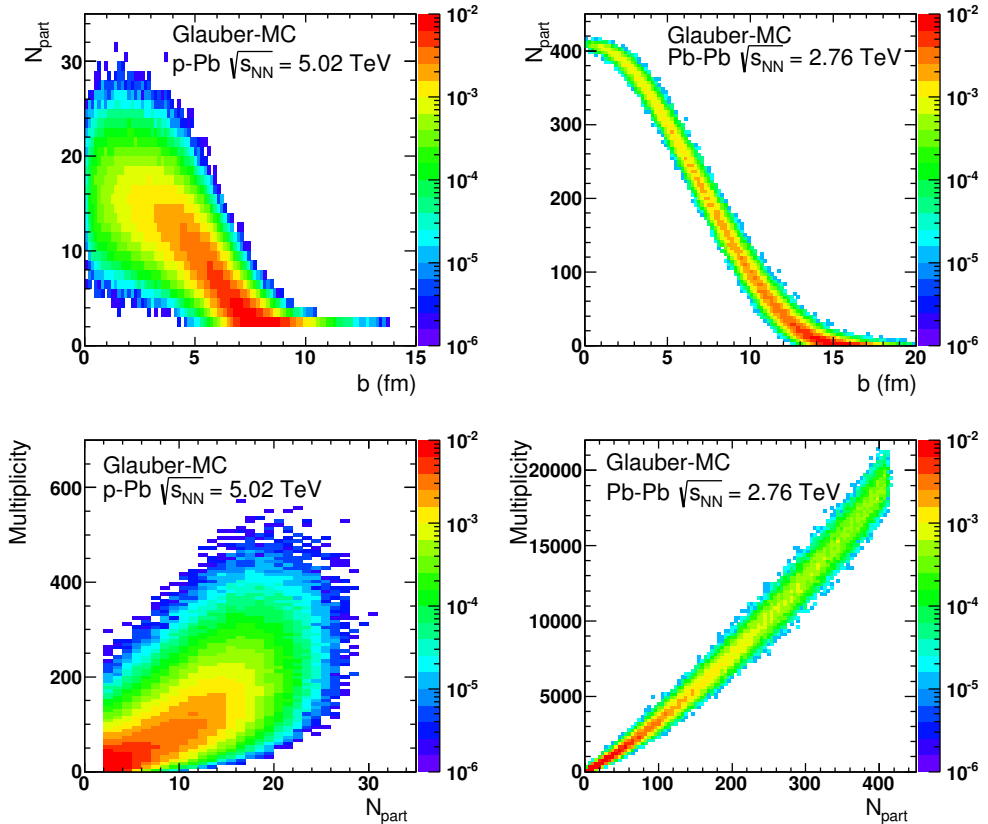


Figure 24: Top: Scatter plot of number of participating nucleons versus impact parameter; Bottom: Scatter plot of multiplicity versus the number of participating nucleons from the Glauber fit for V0A. The quantities are calculated with a Glauber Monte Carlo of p-Pb (left) and Pb-Pb (right) collisions. [?]

959 2 Experimental setup and data samples

960 The $\sqrt{s_{\text{NN}}} = 5.02$ TeV p–Pb ($1.3 \cdot 10^8$ events, $\mathcal{L}_{\text{int}} = 620 \text{ nb}^{-1}$) collisions were
961 recorded in 2013 by the ALICE detector [93]. The details of the performance of
962 the ALICE detector during LHC Run 1 (2009–2013) are presented in Ref. [94].

963 The analysis uses charged tracks that are reconstructed with the Inner Tracking
964 System (ITS) [95] and the Time Projection Chamber (TPC) [96]. These detectors
965 are located inside the large solenoidal magnet, that provides a homogeneous mag-
966 netic field of 0.5 T. Tracks within a pseudorapidity range $|\eta| < 0.9$ over the full
967 azimuth can be reconstructed. The ITS is made up of the innermost Silicon Pixel
968 Detector (SPD), the Silicon Drift Detector (SDD) and the outermost Silicon Strip
969 Detector (SSD). Each of these consists of two layers. The TPC is a cylinder filled
970 with gas. Gas is ionised along the path of charged particles. Liberated electrons
971 drift towards the end plates of the cylinder where they are detected. Combining
972 the information from the ITS and the TPC provides a resolution ranging from 1
973 to 10 % for charged particles with momenta from 0.15 to 100 GeV/c. For tracks
974 without the ITS information, the momentum resolution is comparable to that
975 of ITS+TPC tracks below transverse momentum $p_T = 10$ GeV/c, but for higher
976 momenta the resolution reaches 20 % at $p_T = 50$ GeV/c [94, 97].

977 Neutral particles used in jet reconstruction are reconstructed by the Electro-
978 magnetic Calorimeter (EMCAL) [98]. The EMCAL covers an area with a range
979 of $|\eta| < 0.7$ in pseudorapidity and 100 deg in azimuth. EMCAL is complimented
980 with the Dijet Calorimeter (DCal) [99] and Photon Spectrometer (PHOS) [100]
981 that are situated opposite of the EMCAL in azimuth. PHOS covers 70 degrees
982 in azimuth and $|\eta| < 0.12$. The DCal is technologically identical to EMCal. The
983 DCal coverage spans over 67 degrees in azimuth, but in pseudorapidity the mid
984 region is occupied by the PHOS. In between PHOS and DCal active volumes, there
985 is a gap of 10 cm. DCal is fully back-to-back with EMCal.

986 The combination of charged tracks with $p_T > 0.15$ GeV/c and neutral particles
987 with $p_T > 0.30$ GeV/c is used to construct jets.

988 The V0 detector [101] provides the information for event triggering. The V0
989 detector consists of two scintillator hodoscopes that are located on either side of
990 the interaction point along the beam direction. It covers the pseudorapidity region
991 $-3.7 < \eta < -1.7$ (V0C) and $2.8 < \eta < 5.1$ (V0A). For the 2013 p–Pb collisions
992 events are required to have signals in both V0A and V0C. This condition is used
993 later offline to reduce the contamination of the data sample from beam-gas events
994 by using the timing difference of the signal between the two stations [94].

995 EMCAL is also used to provide the jet trigger used in triggered datasets. EM-
996 CAL can be used to trigger on single shower deposits or energy deposits integrated
997 over a larger area. Latter case is used for jet triggers. The EMCAL trigger defini-

tion in the 2013 p–Pb collisions requires an energy deposit of either 10 GeV for the low threshold trigger or 20 GeV for the high threshold trigger in a 32×32 patch size.

In p–Pb collisions the tracks are selected following the hybrid approach [102] which ensures a uniform distribution of tracks as a function of azimuthal angle (φ). The momentum resolutions of the two classes of particles are comparable up to $p_T \approx 10$ GeV/ c , but after that, tracks without ITS requirements have a worse resolution [94, 97].

3 Experimental Details

3.1 CERN

The European Organization for Nuclear Research (CERN) is the largest particle physics laboratory in the world. CERN was founded in 1954. In 2019 CERN consists of 22 member states. Additionally CERN has contacts with a number of associate member states and various individual institutions. Some 12000 visiting scientists from over 600 institutions in over 70 countries come to CERN for their research. CERN itself is located near Geneva at the border of France and Switzerland and itself employs about 2500 people.

The laboratory includes a series of accelerators, which are used to accelerate the particle beams used. A schematic view of the complex as of 2019 is shown in Figure ???. In the framework of this thesis the main component is the Large Hadron Collider (LHC), the largest collider at CERN. LHC will be discussed in the chapter in more detail. Other accelerators in the series are used to inject the particle beam into LHC, but they are also used in itself for various experimental studies.

The second largest accelerator is the super proton synchrotron (SPS). It is final step before the particle beam is injected into LHC. Commissioned in 1976, it was the largest accelerator at CERN until the the Large Electron-Positron Collider (LEP) was finished in 1989. Originally it was used as a proton-antiproton collider and as such provided the data for the UA1 and UA2 experiments, which resulted in the discovery of the W and Z bosons. At the moment there are several fixed target experiments utilising the beam from SPS. These study the structure (COMPASS) and properties (NA61/SHINE) of hadrons, rare decays of kaons (NA62) and radiation processes in strong electromagnetic fields (NA63). Additionally the AWAKE and UA9 experiments are used for accelerator research and development.

-PS

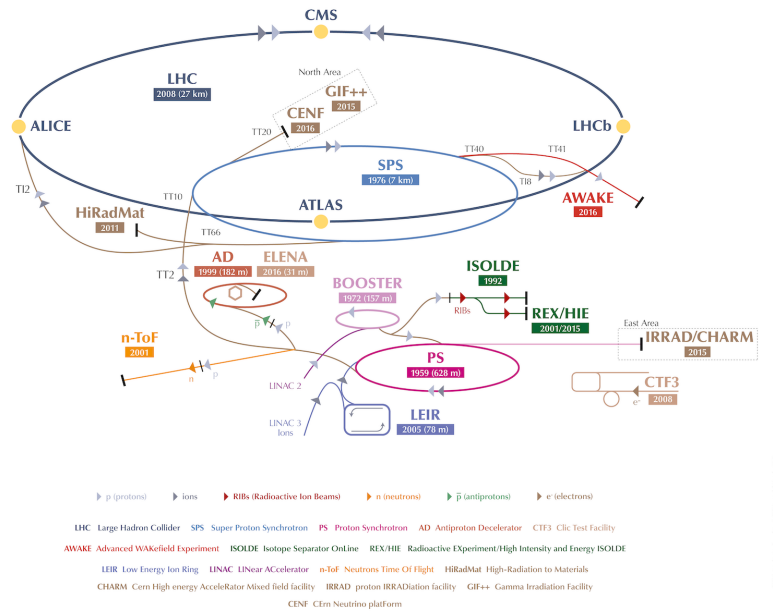


Figure 25: A schematic view of the accelerator complex at CERN. Before particles can be injected into the LHC they require a series of preliminary? acceleterarors. Until 2018 protons start their journey in LINAC2 (Linear Accelerator) and continue through the Booster, Proton Synchrotron (PS) and Super Proton Synchrotron (SPS). Between 2019 and 2020 LINAC2 will be replaced by LINAC4 [?]

₁₀₃₃ **3.2 Large Hadron Collider**

₁₀₃₄ The Large Hadron Collider (LHC) is the largest accelerator at CERN and the
₁₀₃₅ largest particle collider ever built. The LHC is designed to accelerate protons
₁₀₃₆ up to an energy of 8 TeV and lead ions up to 2.76 TeV per nucleon [?]. The design
₁₀₃₇ luminosity of the LHC is $10^{34} \text{ cm}^{-2} \text{s}^{-1}$. In 20xx it achieved a record peak luminosity
₁₀₃₈ of xxx. For lead beams the design luminosity is xxx. All this is achieved with a
₁₀₃₉ ring of 26.7 km, that consists of 1232 superconducting dipole magnets that keep
₁₀₄₀ particles in orbit.

₁₀₄₁ The particles are accelerated through the use of radio-frequency (RF) cavities.
₁₀₄₂ The RF are build such that the electromagnetic waves become resonant and build
₁₀₄₃ up inside the cavity. Charges passing through the cavity feel the overall force
₁₀₄₄ and are pushed forward along the accelerator. As they consist of electromagnetic
₁₀₄₅ waves, the field in the RF cavity oscillates. Thus particles must enter the cavity at
₁₀₄₆ the correct phase of oscillation to receive a forward push. When timed correctly,
₁₀₄₇ the particles will feel zero accelerating voltage when they have exactly the correct
₁₀₄₈ energy. Particles with higher energies will be decelerated and particles with lower
₁₀₄₉ energies will be accelerated. This focuses particles in distinct bunches. The RF
₁₀₅₀ oscillation frequency at the LHC is 400.8 MHz. Thus RF "buckets" are separated
₁₀₅₁ by 2.5 ns. However only 10 % are actually filled with particles, so the bunch
₁₀₅₂ spacing in the LHC is 25 ns, at a bunch frequency of 40 MHz.

₁₀₅₃ With 7 TeV proton beams the dipole magnets used to bend the beam must
₁₀₅₄ produce a magnetic field of 8.33 T. This can be only achieved through making
₁₀₅₅ the magnets superconducting, which requires cooling them down with helium to a
₁₀₅₆ temperature of 1.9 K. The 1232 dipole magnets make up roughly 2/3 of the LHC
₁₀₅₇ circumference. The remaining part is made up of RF cavities, various sensors and
₁₀₅₈ higher multipole magnets used to keep the beam focused. The most notable of
₁₀₅₉ these are the 392 quadrupole magnets.

₁₀₆₀ The LHC is divided into octants, where each octant has a distinct function.
₁₀₆₁ Octants 2 and 8 are used to inject beam into the LHC from SPS. The 2 beams
₁₀₆₂ are crossed in octants 1,2,5 and 8. The main experiments are built around these
₁₀₆₃ crossing points. Octants 3 and 7 are used for beam cleansing. This is achieved
₁₀₆₄ through collimators that scatter particles with too high momentum or position
₁₀₆₅ offsets off from the beam. The RF cavities used for acceleration are located in
₁₀₆₆ octant 4 and octant 6 is used for dumping the beam. The beam dump is made
₁₀₆₇ up of two iron septum magnets, one for each beam, that will kick the beam away
₁₀₆₈ from machine components into an absorber when needed.

1069 **3.2.1 LHC experiments**

1070 As of 2018 there are four main experiments at the LHC; ALICE, ATLAS, CMS
1071 and LHCb and three smaller ones LHCf, TOTEM and MoEDAL. ALICE will be
1072 covered in section 3.3.

1073 ATLAS (A Toroidal LHC ApparatuS) and CMS (Compact Muon Solenoid) are
1074 the two largest experiments at the LHC. They are both multipurpose experiments
1075 designed to be sensitive to many different possible new physics signals. The biggest
1076 discovery made by these so far is the discovery of the Standard Model Higgs boson,
1077 which was simultaneously published by the experiments in 2012 [?, ?].

1078 The LHCb (LHC beauty) experiment [?] is made for studying the bottom
1079 (beauty) quark. Main physics goals include measurement of the parameters of CP
1080 violation with decays of hadron containing the bottom quark. One of the most
1081 important results published by LHCb is the first measurement of $B_s^0 \rightarrow \mu^+ \mu^-$
1082 decay, which was found to be in line with the Standard Model.

1083 In addition to the four large experiments there are three smaller experiments
1084 along the LHC ring. LHCf (LHC forward) is located at interaction point 1 with
1085 ATLAS. It aims to simulate cosmic rays by the particles thrown forwards by the
1086 collisions in ATLAS.

1087 TOTEM (TOTal Elastic and diffractive cross section Measurement) is located
1088 near the CMS experiment at point 5. This allows it to measure particles emerging
1089 from CMS with small angles. The main goals is to measure the total, elastic and
1090 inelastic cross-sections in pp collisions [?].

1091 The MoEDAL (Monopole and Exotics Detector At the LHC) experiment is
1092 located at the interaction point 8 together with the LHCb experiment. MoEDAL
1093 tries to measure signatures of hypothetical particles with magnetic charge, mag-
1094 netic monopoles.

1095 **3.3 ALICE**

1096 ALICE (A Large Ion Collider Experiment) [?] is the dedicated heavy ion exper-
1097 iment at the LHC. ALICE was designed to cope with the expected very high
1098 multiplicity environment of heavy ion collisions. The design allows measurement
1099 of a large number of low momentum tracks. The different detector subsystems are
1100 optimised to provide high momentum resolution and excellent particle identifica-
1101 tion capabilities over a broad range of momentum.

1102 A schematic view of the ALICE detector in 2018 is presented in Figure 26.
1103 This section will go through the composition of ALICE as it has been during
1104 run 2 between 2014 and 2018. The detector will go through significant upgrades
1105 during Long Shutdown 2 in 2019-2020. As in all the major high energy physics
1106 experiments the positioning of the detectors follows a layered structure. Closest to

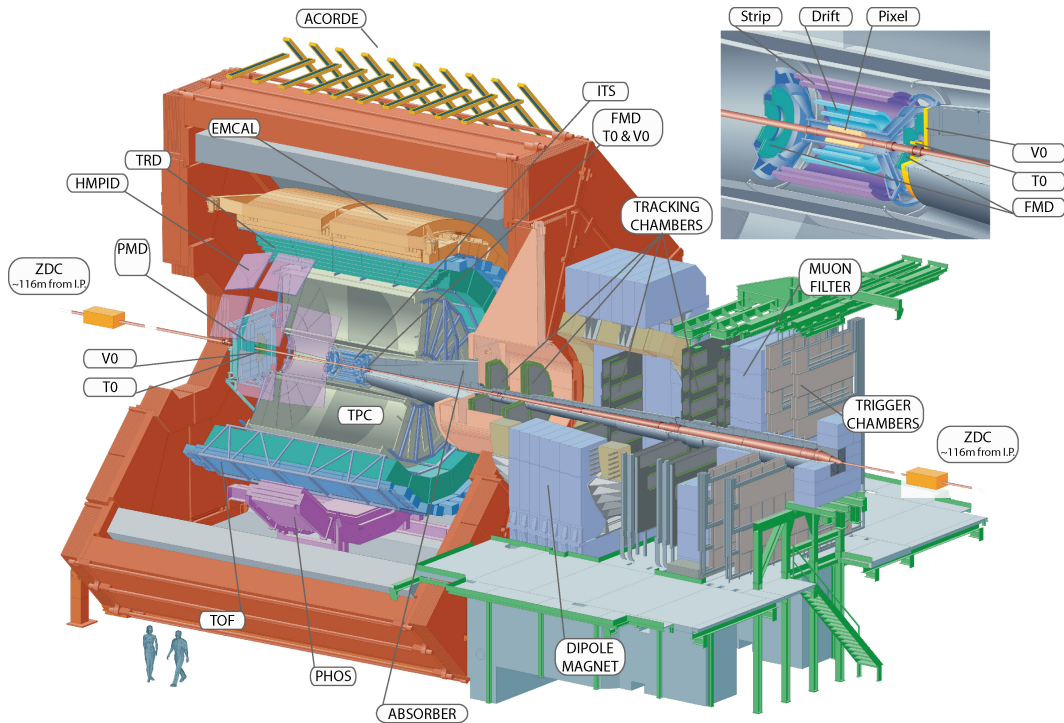


Figure 26: Schematic view of ALICE

the interaction point are the tracking detectors. The main task of these detectors is to locate the position of the primary interaction vertex accurately and to record the tracks of charged particles. To achieve this they need a very good spatial resolution close to the interaction point. Tracking detectors do not significantly alter the tracks of traversing particles. Thus they can be located in the innermost layers.

Calorimeters are designed to stop any particles hitting them and use the absorption to measure the energy of the particles. Thus they must be located behind the tracking detectors. ALICE has two separate calorimeter systems, the electromagnetic calorimeters measure mainly electrons and photons, while the muon detection system measures muons.

3.3.1 Tracking

The main design guideline for the tracking detectors in ALICE was the requirement to have good track separation and high granularity in the high multiplicity environment of heavy ion collisions. Before LHC was built the wildest estimates put the particle density at 8000 charged particles per unit of rapidity [1]. In reality the particle density turned out to be significantly smaller, about 1600 charged

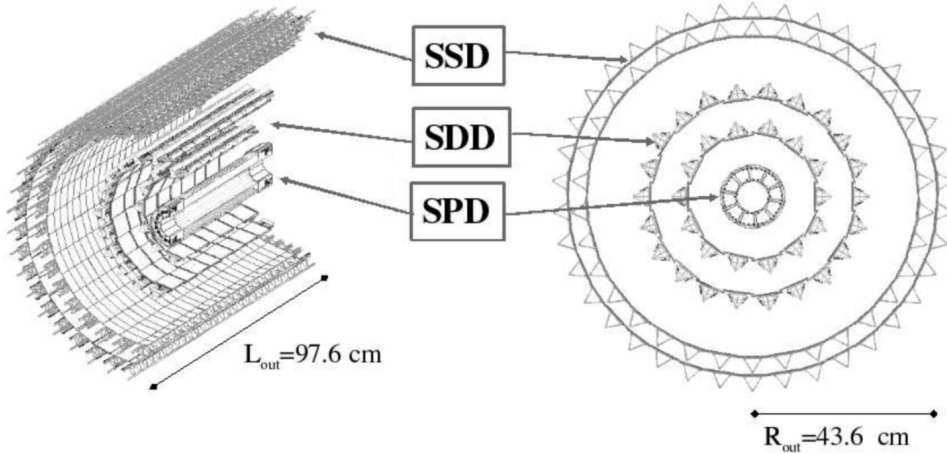


Figure 27: Schematic view of ALICE Inner Tracking System

1124 particles per rapidity unit. []

1125 The main tracking detector in ALICE is the Time Projection Chamber (TPC),
1126 discussed in more detail in section 3.3.2

1127 Between TPC and the beam pipe there is an array of six layers of silicon detec-
1128 tors, called the inner tracking system (ITS) [?]. The main tasks of the ITS are to
1129 locate the primary vertex with a resolution better than $100 \mu m$, to reconstruct the
1130 secondary vertices from decaying particles, to track and identify particles with mo-
1131 menta below 200 MeV and to compliment the momentum and angle measurements
1132 of TPC. During long shutdown 2 in 2019-2020 the entire ITS will be replaced [?].
1133 As of 2018 the two innermost layers are made of the silicon pixel detector (SPD).
1134 As it's the closest detector to the interaction point it requires are very high spatial
1135 resolution. Thus the choice of pixel technology is natural. In heavy ion collisions
1136 the particle density is around 50 particles per cm^2 .

1137 The next two layers are the silicon drift detector (SDD), which is made out of
1138 homogeneous neutron transmutation doped silicon. It is ionized when a charged
1139 particle goes through the material. The generated charge then drifts to the col-
1140 lection anodes, where it is measured. The maximum drift time in SDD is about 5
1141 μs . This design gives very good multitrack capabilities and provides two out of the
1142 four dE/dx samples in the ITS.

1143 The two remaining layers in the ITS are the silicon strip detector (SSD). The
1144 strips work in a similar way as silicon pixels, but by itself one layer only provides
1145 good resolution in one direction. Combining two crossing grids of strips provides 2
1146 dimensional detection. Each charged particle will hit two intervening strips. The
1147 position of the hit can be deduced from the place where the strips cross each other.

1148 **3.3.2 TPC**

1149 Time projection chamber (TPC) is a cylindrical detector filled with $88m^3$ of
1150 Ne – CO₂ (90/10 %) gas mixture. The gas is contained in a field cage that provides
1151 an uniform electric field of $400V/cm$ along the z-axis (along the beam direction).
1152 Charged particles traversing through the TPC volume will ionise the gas along
1153 their path. This liberates electors that drift towards the end plates of the cylin-
1154 der.

1155 The field cage is separated into two detection volumes by the central high
1156 voltage electrode. Both sides have a drift length of 2.5 m and inner/outer diameters
1157 of 1.2/5 m. This means the central electrode must provide a maximum potential
1158 of 100 kV to achieve the design field magnitude. The maximum time required for
1159 electrons to drift through the chamber is about $90 \mu s$.

1160 When electrons reach the end of the main cylinder they enter the readout
1161 chambers. The readout section of both sides consists of 18 outer chambers and
1162 18 inner chambers. Each of them are made of multiwire proportional chambers
1163 with cathode pad readout. This design is used in many TPCs before. During
1164 Long Shutdown 2 in 2019-2020, the multiwire chambers will be replaced by Gas
1165 Electron Multipliers (GEMs, see section 3.3.3).

1166 The relatively slow drift time of $90 \mu s$ is the limiting factor for the luminosity
1167 ALICE can take. The occupancy of the TPC must be kept in a manageable level.

1168 **3.3.3 TPC upgrade**

1169 During long shutdown 2 in 2019-2020 ALICE will go through significant modifica-
1170 tions. The goal is to be able have continuous readout [?] in heavy ion collisions at
1171 an interaction rate of 50 kHz. I have made a personal contribution to the quality
1172 assurance of the new GEM readout of TPC.

1173 ALICE will add a new Forward Interaction trigger (FIT) to replace the V0 and
1174 T0 detectors.

1175 Additionally the current inner tracking system (ITS) will be completely re-
1176 placed. The current layered structure with three different technologies will be
1177 replaced by an all pixel detector with significantly reduced pixel size. Additionally
1178 the first layer will be brought closer to the beam pipe. The new ITS will have
1179 better tracking efficiency and better impact parameter resolution.

1180 The muon detection will be complimented by the Muon Forward Tracker (MFT) [?].
1181 Based on the same technology as the new ITS, MFT will be placed before the
1182 hadron absorber that sits in front of the existing muon spectrometer. MFT should
1183 significantly increase the signal/background ratio in heavy quark measurements.

1184 Many subdetectors will make small improvements to enhance the readout rate.
1185 The central trigger processor will be replaced and ALICE will introduce a new

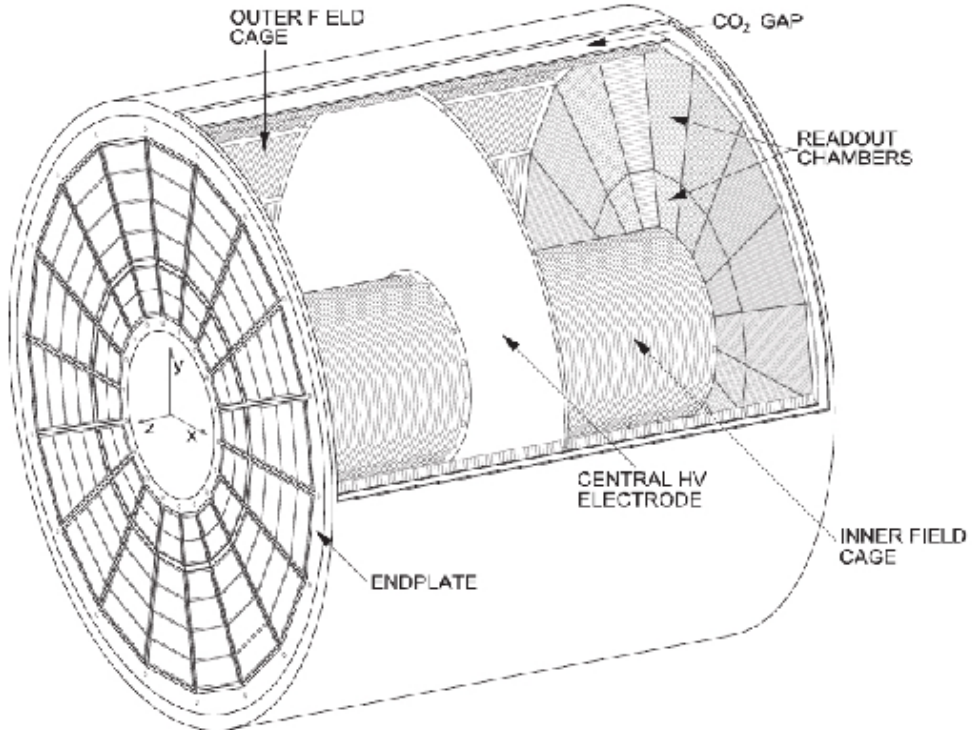


Figure 28: Schematic view of ALICE Time Projection Chamber

1186 framework O^2 that combines both online data acquisition and offline analysis.

1187 The detector restricting the readout the most at the moment is the TPC. The
 1188 current wire chamber based system limits the readout rate to 3.5 kHz. To achieve
 1189 the 50 kHz readout rate goal the wire chambers will be replaced by a Gas Electron
 1190 Multiplier (GEM) based system.

1191 TPC has a total of 36 inner and 36 outer readout chambers. Each of these will
 1192 consist of 4 layers of GEM foils. The inner chambers will only have one foil for
 1193 each layer. The outer chambers are separated into three sections, each with its
 1194 own layer of foils. Each gem foil is made up of a $50\ \mu\text{m}$ thick resistive capton layer,
 1195 coated on both sides by $5\mu\text{m}$ thick layers of copper. Each foils is separated into a
 1196 number (20-24) of distinct active areas. The active areas are pierced quite densely,
 1197 they have 50-100 holes in the area of a single mm^2 . The density of holes changes
 1198 from layer to layer. The two middle layers of foils have a larger (double) pitch
 1199 (smaller hole density) while the top and bottom layers have a smaller (normal)
 1200 pitch (larger hole density).

1201 The holes have a conical shape which they acquire during a two step chemical
 1202 etching process.

1203 The working principle of these foils is based on electrodynamics. **elaborate** There
1204 is a large potential difference (140-400 V) applied to the two sides of the foil, which
1205 results in large field in each hole. This acts both as a lens and an amplifier for
1206 the electrons. The amplification happens inside the holes where the field is the
1207 strongest.

1208 The GEMs are designed to minimize ion backflow to allow continuous, ungated
1209 and untriggered readout.

1210 3.3.4 Particle identification

1211 One guiding principle in the design of ALICE was to achieve good particle iden-
1212 tification (PID) over a large part of phases space and for several different particle
1213 types. In ALICE there are several detectors taking part in the identification of
1214 particles.

1215 One of the particle identification detectors is the transition radiation detector
1216 (TRD) [?]. Its main task is identifying electors with momenta larger than 1 GeV.
1217 Transition radiation is produced when highly relativistic particles traverse the
1218 boundary between to media having different dielectric constants. The average
1219 energy of the emitted photon is approximately proportional to the Lorentz factor γ
1220 of the particle, which provides an excellent way of discriminating between electrons
1221 and pion. ALICE TRD is made of a composite layer of foam and fibres. The
1222 emitted photons are then measured in six layers of Xe/CO₂ filled time expansion
1223 wire chambers.

1224 The time of flight (TOF) detector uses a very simple physics principle, i.e.
1225 calculating the velocity of the particle using the time of flight between two points.
1226 Combining this with the momentum of particle, obtained from the tracking de-
1227 tectors, one can calculate the mass of the particle, which identifies particles. The
1228 TOF detector consists of multigap resistive wire chambers. These are stacks of
1229 resistive plates spaced equally. They allow time of flight measurements in large
1230 acceptance with high efficiency and with a resolution better than 100 ps.

1231 The third specific particle identification detector is the high momentum particle
1232 identification (HMPID) detector. The HMPID uses a ring imaging Cherenkov
1233 counter to identify particles with momenta larger than 1 GeV. Particles moving
1234 through a material faster than the speed of light in the material will produce
1235 Cherenkov radiation. The velocity of the particle determines the angle at which
1236 the radiation is emitted. Measuring this angle gives the velocity of the particle.
1237 This can be again used to calculate the mass of the particle, if the momentum is
1238 known. In HMPID the material is a liquid radiator and the photons are measured
1239 with multiwire proportional chambers in conjunction with photocathodes.

1240 In addition to the specific particle identification detectors, the general purpose
1241 tracking detectors can be used for identification through the use of specific energy

loss of charged particles traversing through a medium and the transition radiation emitted by charged particles when crossing the boundary between two materials.

dE/dx measurements are provided by the last four layers of the ITS detector, i.e. the SDD and the SSD, thanks to their analog readout. [?] ITS provides particle identification in the low p_T region, up to 1GeV, and pions reconstructed in the standalone mode can be identified down to 100 MeV. Similar to ITS the TPC detector provides specific energy loss measurements. TPC can identify charged hadrons up to p_T 1 – 2GeV as well as light nuclei, He3 and He4.

3.3.5 Electromagnetic Calorimeter

Calorimeters are designed to measure the energy of particles. Electromagnetic calorimeters specialise in detecting particles that interact primarily through the electromagnetic interaction, namely photons and electrons. They are required in many neutral meson and direct photon analyses. In addition the energy information enhance jet measurements.

ALICE has two electromagnetic calorimeters, the photon spectrometer (PHOS) [?] and the electromagnetic calorimeter (EMCal) [?]. PHOS is a homogeneous calorimeter that consists of scintillating PbWO₄ crystals, which generate a bremsstrahlung shower and produce scintillation light. The energy of the particle determines the amount of light produced. To improve the charged particle rejection, PHOS includes a charged particle veto detector (CPV) [?]. PHOS is built to have a very fine granularity, making it well suited for measuring direct photons and neutral mesons.

EMCal is a sampling calorimeter. It consists of layers of lead and scintillator tiles. The lead tiles produce the shower and scintillator tiles the light. The signal is then read with wavelength shifting fibres. The acceptance of EMCal in the azimuthal angle is 80 deg < ϕ < 187 deg. During long shutdown 1 in 2013-2015, EMCal was extended with the di-jet calorimeter (DCal) [?], giving an additional acceptance region of 260 deg < ϕ < 320 deg. This provides partial back-to-back coverage. In comparison to PHOS, EMCal has coarser granularity, but a significantly larger acceptance, making it suitable for jet physics.

3.3.6 Forward detectors

ALICE includes a few small and specialised detectors of importance. The event time is determined with very good precision (< 25 ns) by the T0 detector [?]. T0 consists of two sets of Cherenkov counters that are mounted around the beam pipe on both sides of the interaction point. T0 gives the luminosity measurement in ALICE.

Another small detector in the forward direction is the V0 detector [?]. This

1279 consists of two arrays of segmented scintillator counters located at $-3.7 < \eta <$
1280 -1.7 and $2.8 < \eta < 5.1$. V0 is used as a minimum bias trigger and for rejection
1281 of beam-gas background. Particle multiplicity in the forward direction can be
1282 related to the event centrality. Thus V0 is the main detector used in centrality
1283 determination in PbPb collisions.

1284 The multiplicity measurement of V0 is complimented by the forward multi-
1285 plicity detector (FMD) [?]. FMD includes five rings of silicon strip detectors that
1286 make up the FMD. FMD gives acceptance in the range $-3.4 < \eta < -1.7$ and
1287 $1.7 < \eta < 5.0$.

1288 During long shutdown 2 in 2019-2020, V0 and T0 will be replaced by the Fast
1289 Interaction Trigger (FIT) detector [?]. For historical reasons elements of FIT are
1290 also referred to as V0+ and T0+. FIT will allow centrality, event plane, luminosity
1291 and interaction time determination in the continuous readout mode, that ALICE
1292 will operate in after 2020.

1293 For photon multiplicity measurement ALICE has the photon multiplicity de-
1294 tector (PMD) [?]. PMD uses two planes of gas proportional counters with a
1295 cellular honeycomb structure. PMD gives the multiplicity and spatial distribution
1296 of photons in the region $2.3 < \eta < 3.7$.

1297 On top of the ALICE magnet there is an array of 60 large scintillators called
1298 the ALICE cosmic ray detector (ACORDE) [?]. ACORDE is used as a trigger
1299 for cosmic rays for calibration and alignment.

1300 The only hadronic calorimeters in ALICE are the zero degree calorimeters
1301 (ZDC) [?], which are located next to the beam pipe in the machine tunnel about
1302 116 m from the interaction point. There are two sets of calorimeters. One is
1303 made of tungsten, specialising in measuring neutrons, while the other, made of
1304 brass, is specialised in measuring protons. In heavy ion and especially in proton-
1305 lead collisions, ZDC gives information about the centrality of the event. ZDC is
1306 meant to detect spectators, i.e. parts of the colliding ions that do not take part
1307 in the interaction. If there are more spectators, the collisions is likely to be more
1308 peripheral.

1309 A new detector installed during the long shutdown 1 is the ALICE diffractive
1310 detector (AD) [?]. AD consists of two assemblies, one in each side of the interaction
1311 point, both made of two layers of scintillators. These assemblies are situated about
1312 17 m and 19.5 m away from the interaction points. The pseudorapidity coverage is
1313 $-6.96 < \eta < -4.92$ and $4.78 < \eta < 6.31$. AD greatly enhances ALICE's capability
1314 for diffractive physics measurements that require a large pseudorapidity gap.

1315 3.3.7 Muon spectrometer

1316 Outside the main magnet, ALICE has a spectrometer dedicated to measuring
1317 muons [?]. In heavy ion physics muons are mainly used to measure the production

1318 of the heavy quark resonances J/ψ , Ψ' , Υ , Υ' and Υ'' .

1319 The muon spectrometer consists of three parts, the absorber, the muon tracker
1320 and the muon trigger. The absorber is meant to remove the hadronic background
1321 as efficiently as possible. After the absorber there are ten plates of thin cathode
1322 strip tracking stations with high granularity, the muon tracker. After the muon
1323 tracker there is a layer of iron to filter out any remaining particles, other than
1324 muons. The muon trigger is located behind this layer. The trigger consists of four
1325 resistive plate chambers.

1326 **3.3.8 Trigger**

1327 4 Event and track selection

1328 5 Analysis method

1329 5.1 Jet Finding

1330 The analysis is performed by analysing jet constituents. In each collision event, the
1331 jets are reconstructed using FastJet [103] with the anti- k_T algorithm [104]. Jets for
1332 $R=0.4$ are selected in $|\eta| < 0.25$ to satisfy the fiducial acceptance of the EMCAL. In
1333 jet reconstruction both charged tracks with $p_T > 0.15 \text{ GeV}/c$ and neutral cluster
1334 with $p_T > 0.30 \text{ GeV}/c$ are considered. In the analysis, results are presented in
1335 terms of the jet transverse momentum $p_{T,\text{jet}}$.

1336 5.1.1 Anti k_T algorithm

1337 Jets are reconstructed using the anti- k_T algorithm [104]. The algorithm works by
1338 trying to undo the splittings through combining pseudojets/tracks.

$$k_{T,i}^2 = p_{T,i}^{2p}$$

1339 For each pair of protojets the distance measure is calculated as

$$k_{T,(i,j)}^2 = \min(p_{T,i}^{2p}, p_{T,j}^{2p}) \frac{\Delta R_{i,j}^2}{D^2},$$

1340 where

$$R_{i,j} = (\phi_i - \phi_j)^2 + (y_i - y_j)^2$$

1341 If $k_{T,i}$ is the smallest quantity then the protojet is a jet and it is removed
1342 from further consideration. If $k_{T,(i,j)}$ is the smallest quantity the two protojets are
1343 merged. Iterate until no protojets are left.

1344 The choice of the power p in the distance measure depends on the algorithm
1345 used

- 1346 • $p = 1$: k_T algorithm
- 1347 • $p = 0$: Cambridge Aachen algorithm
- 1348 • $p = -1$: anti- k_T algorithm

1349 With the choice $p = -1$ in anti- k_T algorithm, the softest splittings are undone
1350 first.

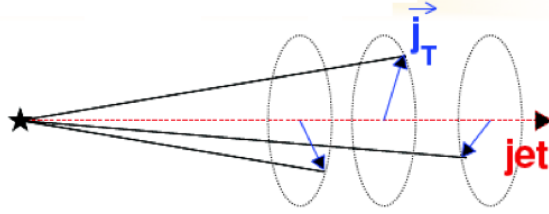


Figure 29: Illustration of \vec{j}_T . The jet fragmentation transverse momentum, \vec{j}_T , is defined as the transverse momentum component of the track momentum, \vec{p}_{track} , with respect to the jet momentum, \vec{p}_{jet} .

1351 5.2 j_T

1352 The jet fragmentation transverse momentum, j_T , is defined as the component of
1353 the constituent particle momentum, \vec{p}_a , transverse to the jet momentum, \vec{p}_{jet} . The
1354 resulting \vec{j}_T is illustrated in Fig. 29. The length of the \vec{j}_T vector is

$$j_T = \frac{|\vec{p}_{\text{jet}} \times \vec{p}_{\text{track}}|}{|\vec{p}_{\text{jet}}|}. \quad (28)$$

1355 It is commonly interpreted as a transverse kick with respect to the initial hard
1356 parton momentum that is given to a fragmenting particle during the fragmentation
1357 process, which is a measure of the momentum spread of the jet fragments [].

1358 The reconstructed jet axis is used for j_T reference. Any charged track within
1359 a fixed cone with radius R is taken as a jet constituent, as opposed to using the
1360 constituent list provided by the jet algorithm. Anti- k_T produces jets that are
1361 very circular in shape. Thus this doesn't change the constituent list considerably.
1362 Neutral tracks are used only in jet reconstruction.

1363 5.2.1 1 over j_T

j_T results are shown as

$$\frac{1}{j_T} \frac{dN}{dj_T}$$

1364 distributions. The logic behind this is that j_T is inherently a two-dimensional
1365 observable, comprised of j_{Tx} and j_{Ty} components. So the actual physical observable
1366 would be

$$\frac{d^2N}{dj_{Tx} dj_{Ty}}$$

1367 Changing into polar coordinates with $j_{\text{Tr}} = j_{\text{T}}$ and θ gives

$$\frac{d^2N}{j_{\text{T}} dj_{\text{T}} d\theta},$$

1368 where j_{T} over the azimuth θ should stay constant and it can be integrated over
1369 giving

$$\frac{1}{2\pi} \frac{dN}{j_{\text{T}} dj_{\text{T}}}.$$

1370 5.3 Unfolding

1371 Extend unfolding

1372 The resulting j_{T} distributions are corrected for the detector inefficiency using
1373 the unfolding method. The response matrix for the unfolding is obtained from a
1374 PYTHIA [105] simulation.

Measured distributions are affected by two main factors; Limited acceptance -
The probability to observe a given event is less than one and limited resolution -
Quantity x cannot be determined exactly, but there is a measurement error. True
 $f(x)$ and measured $g(y)$ distributions are connected by a convolution integral.
Including statistical fluctuations this becomes

$$\hat{g}(y) = \int_a^b A(y, x) f(x) dx + \epsilon(y),$$

where A is the detector response obtained by Monte Carlo simulations and $\epsilon(y)$
is the term coming from statistical fluctuations. If x and y are discrete variables
we have

$$\hat{g}_i = \sum_{j=1}^m A_{ij} f_j + \epsilon_i,$$

Or in matrix form

$$\hat{g} = Af + \epsilon$$

If the only detector effect is limited acceptance, A is a diagonal matrix. In a
general discrete case the (naive) solution is obtained by the inverse matrix

$$\hat{f} = A^{-1} \hat{g}$$

1375 However this usually leads to oscillating solutions and determining the inverse
1376 matrix can be difficult.

1377 Two common methods to perform this inversion are Bayesian and SVD unfold-
1378 ing methods. Often the solution requires some additional *a priori*. For example
1379 the solution should be smooth in most cases.

1380 **5.3.1 Bayesian unfolding**

The bayesian (iterative) method is based on the Bayes formula [].

$$P(C_i|E_j) = \frac{P(E_j|C_i) P_0(C_i)}{\sum_{l=1}^{n_C} P(E_j|C_l) P_0(C_l)},$$

1381 i.e. Probability of Cause ("truth") C_i given Effect ("observed") E_j is proportional to the probability of observing E_j given C_i (response matrix) and the truth distribution $P_0(C_i)$.

At first P_0 is given some starting distribution, either a uniform distribution or some guess of the final distribution. Taking into account the inefficiency this gives

$$\hat{n}(C_i) = \frac{1}{\epsilon_i} \sum_{j=1}^{n_E} n(E_j) P(C_i|E_j),$$

where

$$P(C_i|E_j) = \frac{P(E_j|C_i) P_0(C_i)}{\sum_{l=1}^{n_C} P(E_j|C_l) P_0(C_l)},$$

and

$$\hat{n}(C_i) = \frac{1}{\epsilon_i} \sum_{j=1}^{n_E} n(E_j) P(C_i|E_j).$$

First $P(C_i|E_j)$ is calculated with the uniform distribution or best guess of the shape of the distribution. This is then used to calculate the new distribution $\hat{P}(C_i)$

$$\hat{N}_{true} = \sum_{i=1}^{n_C} \hat{n}(C_i), \hat{P}(C_i) = P(C_i|n(E)) = \frac{\hat{n}(C_i)}{\hat{N}_{true}}$$

1384 P_0 is then replaced with \hat{P} and the procedure is repeated until an acceptable solution is found.

1386 **5.3.2 Toy Monte Carlo**

remove? A toy Monte Carlo simulation was performed to see the performance in an ideal case. Sample jet p_T values from observed p_T distribution. Starting from this p_T start creating tracks with

$$p_{track} = z_{track} p_{T,jet}$$

1387 where z_{track} is sampled from the observed z distribution. All tracks below 0.15GeV 1388 are discarded. Sampling is continued until the sum of the track transverse momenta

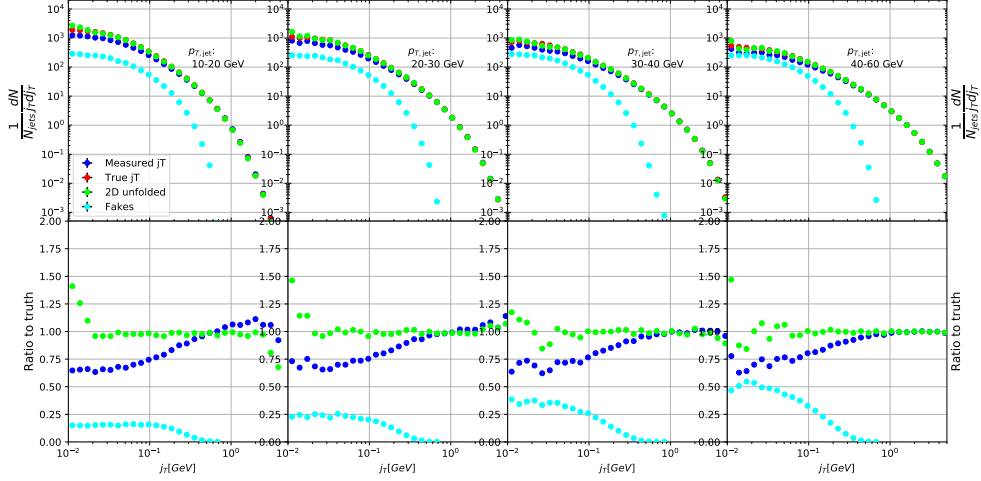


Figure 30: Results from unfolding in Toy Monte Carlo

1389 exceeds the jet transverse momentum. Jet is then defined as the sum of the track
 1390 momenta.

1391 Simultaneously a p_T dependant observation efficiency is applied to the tracks
 1392 and a separate observed jet is calculated using only the observed tracks. Addi-
 1393 tionally a set of fake tracks is added to the observed jet. Tracks are always either
 1394 observed or not at the true momentum. No smearing is added to the observed
 1395 momentum.

Afterwards the tracks are looped over for j_T calculation. For observed tracks we calculate j_T with respect to both the true jet axis and the observed jet. 2D Response matrix is filled with

$$(j_{T,\text{obs}}, p_{T,\text{jet},\text{obs}}, j_{T,\text{true}}, p_{T,\text{jet},\text{true}})$$

1396 In practice this is done with a set of 3D histograms, where $p_{T,\text{jet},\text{true}}$ determines
 1397 the histogram index and the remaining three values the bin in the 3D histogram.

1398 After creating the response matrices, an identical procedure is carried out the
 1399 create testing data. Now instead of filling response matrices, 2D histograms are
 1400 filled with $(j_{T,\text{obs}}, p_{T,\text{jet},\text{obs}})$ and $(j_{T,\text{true}}, p_{T,\text{jet},\text{true}})$

1401 The observed distributions are unfolded using RooUnfold's 2D Bayesian (iter-
 1402 ative) algorithm. Results are shown in figure 30.

1403 5.3.3 Pythia Response matrices

1404 Response matrices are filled through correlation between MC detector and particle
 1405 level jets and tracks.

Table 2: j_T and p_T ranges used in unfolding. The same ranges are used for detector and truth level.

	j_T	$p_{T\text{jet}}$
Min	0.01	5
Max	20	500

1406 The ranges of both j_T and $p_{T\text{jet}}$ extend the ranges in end results. These are
1407 shown in Tab. 2. The ranges are the same in detector and particle level.

1408 When calculating j_T for MC particles the code checks whether a corresponding
1409 detector level track exists and if that track had a j_T value. Additionally check
1410 for detector level tracks that don't have corresponding particle level track or that
1411 track does not have j_T value.

1412 Possible cases:

- 1413 • We find a corresponding track with a j_T value, response matrix is filled
1414 normally with $(j_T^{obs}, p_T^{obs}, j_T^{true}, p_T^{true})$
- 1415 • We don't find a corresponding track. Record (j_T^{true}, p_T^{true}) as a miss
- 1416 • We find a corresponding track, but it didn't have j_T value. Most likely
1417 because it was not part of a jet. Similary record (j_T^{true}, p_T^{true}) as a miss
- 1418 • For detector level tracks with no correspondence in particle level set record
1419 cord (j_T^{obs}, p_T^{obs}) as a fake

1420 5.3.4 2D response matrices

1421 In the analysis code the response matrix is made of an array of 3 dimensional
1422 histograms, with $(j_{T,obs}, p_{T,obs}, j_{T,true})$ as axes. The histogram index gives the $p_{T,true}$
1423 value.

1424 5.3.5 Unfolding algorithm

1425 As a primary method unfolding is performed with an iterative (bayesian) algorithm
1426 using the RooUnfold [106] package. The number of iterations used is 4.

1427 5.3.6 Effect of number of iterations

1428 The iterative unfolding algorithm permits the change of number of iterations.
1429 The unfolding was carried out using different numbers of iterations. The results
1430 from these different cases are shown in Fig. 31. The results are compared to the
1431 default unfolding algorithm with 4 iterations. The difference in results between
1432 the different cases is mostly less than 2.5%.

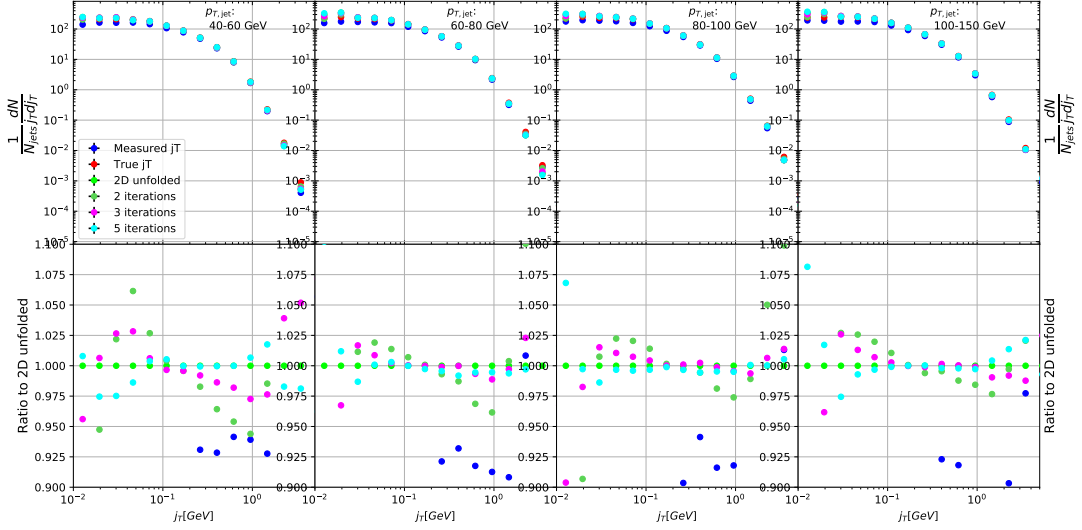


Figure 31: Unfolding with different number of iterations

1433 5.3.7 Effect of different prior

1434 The iterative algorithm requires a prior estimate of the shape of the distribution.
 1435 As a default prior the truth (particle level) distribution is used. To test the effect
 1436 of changing the prior we instead use the unfolded j_T distribution as prior. The
 1437 results are compared to the unfolding algorithm with the default prior. This is
 1438 shown in Fig. 32 The difference in results between the different cases is mostly less
 1439 than 2.5%.

1440 5.3.8 Effect of p_T truncation

1441 5.3.9 Unfolding closure test

1442 Pythia set is divided in 2 halves. First is used to fill the response matrices, as well
 1443 as record missed and fake tracks. Second half is used to test the effectiveness of
 1444 the unfolding method. Jet p_T distributions are shown in figure 34a and response
 1445 matrix are shown in figure 34b.

1446 Response matrices within single jet p_T bins are shown in figure 35. Results
 1447 from the closure test are shown in figure 36. In the lowest jet p_T bins unfolding
 1448 fails to recover the true distribution. The lowest jet p_T bins are dominated by
 1449 combinatorial jets and thus the true detector response is likely not retrieved.

1450 Above jet p_T 30-40 GeV the distribution is recovered well in the mid j_T region.
 1451 At $j_T < 0.1$ there is clear discrepancy. The final results are shown only for $j_T > 0.1$.
 1452 Additionally there is some discrepancy at very high j_T . This is taken into account

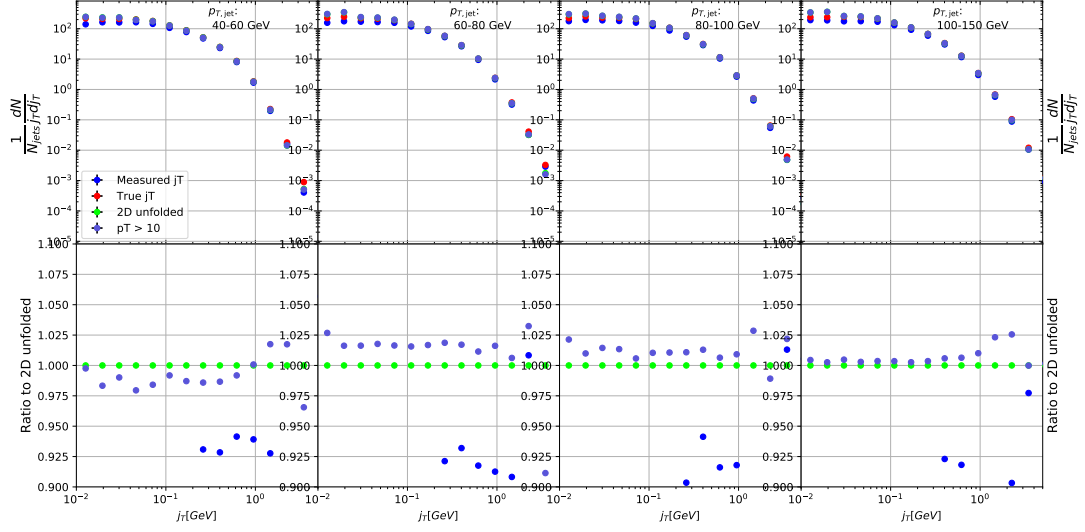


Figure 32: Effect of changing minimum jet p_T used in unfolding from 5 to 10 GeV

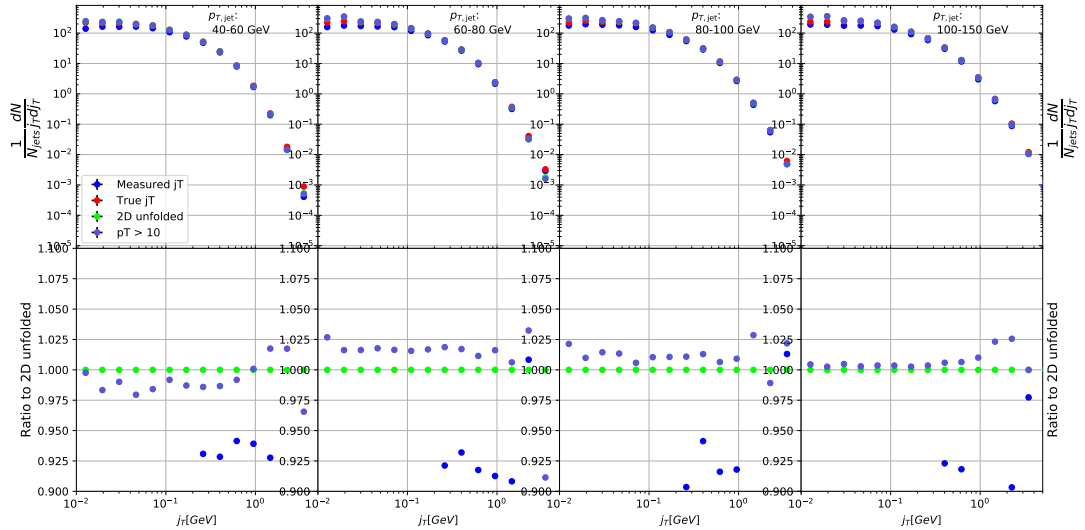
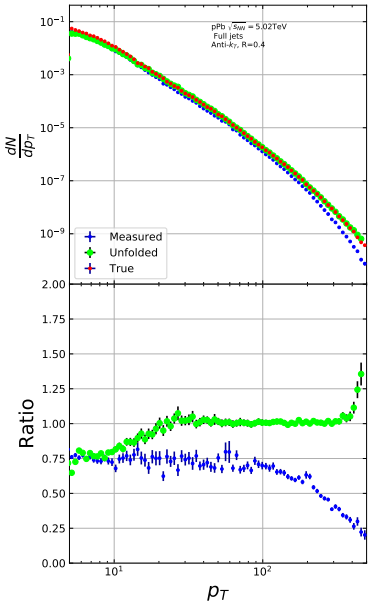
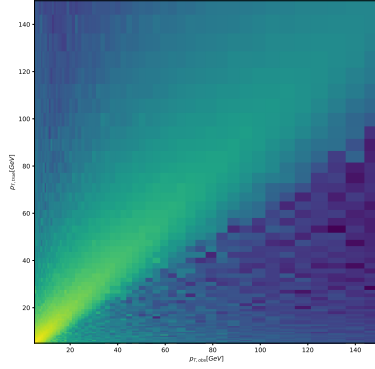


Figure 33: Effect of changing minimum jet p_T used in unfolding from 5 to 10 GeV



(a) Unfolded jet p_T distribution in Pythia
closure test



(b) Jet p_T response matrix from unfolding
closure test

1453 in the unfolding systematics. (TODO: Show this)

1454 5.4 Background

1455 When calculating j_T distribution for jet constituents there is a contribution from
1456 underlying event (UE), i.e. tracks that just happen to be close to the jet axis.
1457 To find the signal coming from the actual jet we need to subtract the background
1458 (UE) contribution. On a jet-by-jet basis this is impossible, so we try to estimate
1459 the background by looking at regions of the detector where there are no tracks
1460 from jets, but only uncorrelated tracks from the underlying event.

1461 The underlying event is estimated by looking at an imaginary jet cone perpen-
1462 dicular to the observed jet axis ($\frac{\pi}{2}$ Rotation in ϕ). j_T is calculated for any tracks
1463 found within this cone. The vector sum of the individual track momentum and
1464 the imaginary jet axis is used as reference for j_T . The background obtained in
1465 this manner is subtracted from the unfolded inclusive j_T distribution, which gives
1466 the resulting signal distribution. To make sure there is no jet contribution in the
1467 background, any events with jets inside the perpendicular cone are not used for
1468 background estimation.

1469 We have two methods for background estimation. In the first we look at the
1470 direction perpendicular to the jet. This is assumed to be the region least likely to
1471 contain jet contributions.

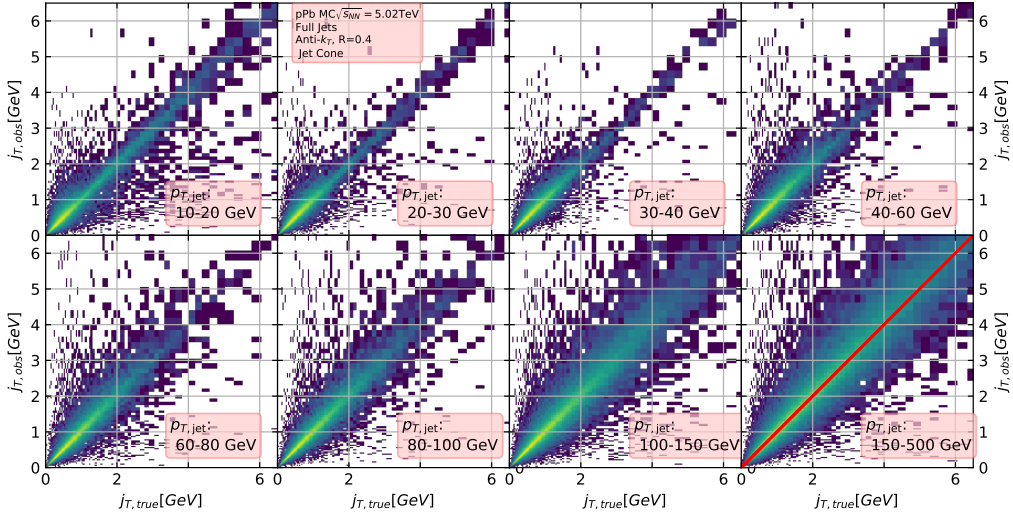


Figure 35: j_T Response matrices in single jet p_T bins

In the second method we randomly assign the tracks of event new ϕ and η values. The result is guaranteed to be uncorrelated.

5.4.1 Perpendicular cone background

After calculating the j_T values for tracks in the jet, we rotate the jet axis by $\frac{\pi}{2}$ in positive ϕ direction. We check that there are no other jets closer than $2R$ to the rotated axis. If there are then background calculation is skipped for this jet. Probability of this happening is 1-2% depending on the jet p_T bin.

If we don't find other jets in the vicinity we move on to estimate the background. We find all tracks within a cone of radius R around the rotated axis and calculate j_T of these tracks with respect to the rotated axis. Auto-correlations are added to match effect to jet. (see 5.4.3)

5.4.2 Random background

In the random background method we look at all tracks in the event, except for tracks close to jets found by the jet algorithm. We randomly assign new η and ϕ values to all tracks using uniform distribution. $|\eta| < 1.0$ p_T values are kept the same. To increase statistics there is a possibility to create a number of random tracks for each actual track. In the analysis we currently do this 10 times for each track. Again the track p_T value is kept the same.

We create a random jet cone from uniform η and ϕ distributions. Here $|\eta| < 0.25$. Now we calculate j_T of the random tracks with respect to the random cone

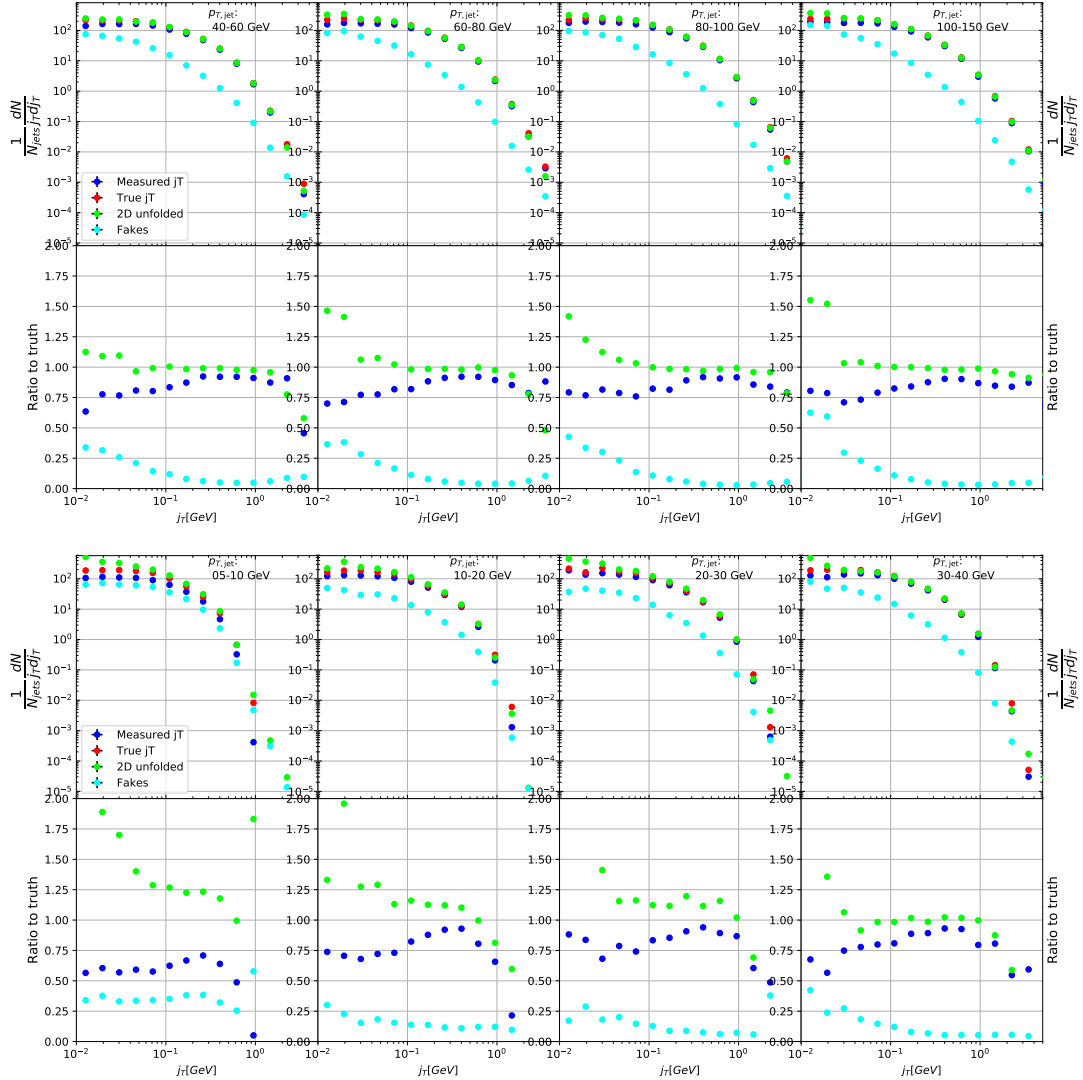
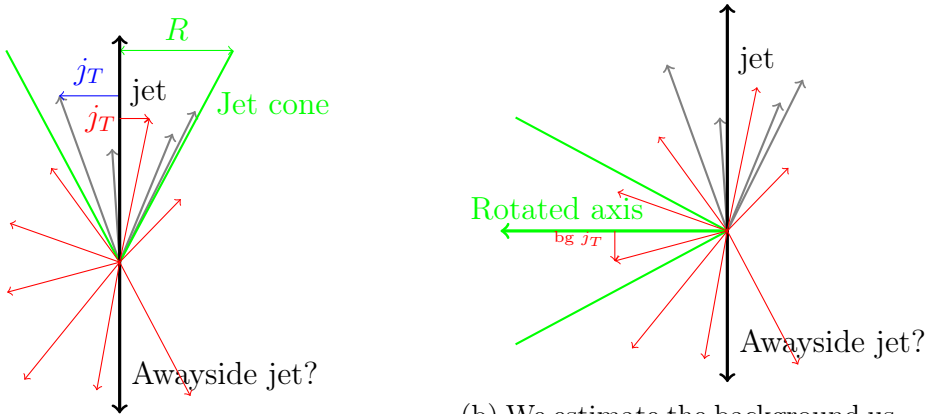
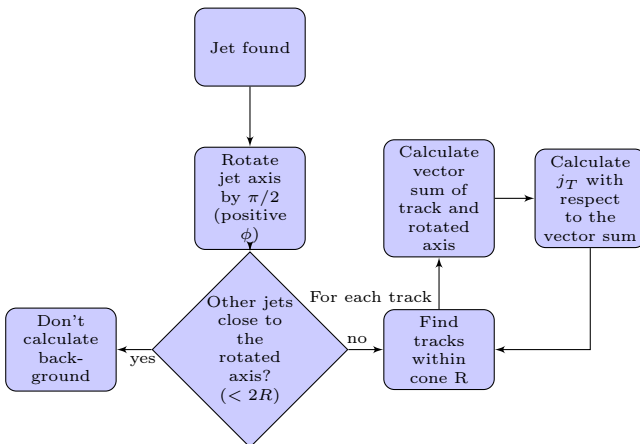


Figure 36: Pythia closure test results. Fake tracks include also tracks that do exist in the true dataset, but for one reason or another were not given j_T values. j_T is only calculated for tracks that are associated with jets



(a) Red is underlying event while gray tracks represent the signal
(b) We estimate the background using a cone where the axis is perpendicular to the jet axis



1492 axis. Auto-correlations are added before calculating j_T (see 5.4.3)

1493 5.4.3 Auto-correlations

1494 Jet axis is simply a vector sum of all its constituents. Thus having an additional
1495 track in the jet from the underlying event moves the jet axis towards this track.
1496 Since the axis is now closer to the track, it has a smaller j_T value. Assuming a 1
1497 GeV background track at the edge of a $R = 0.4$ the j_T value would be 0.4GeV.
1498 If this is added to a 5GeV jet, the j_T value becomes 0.33GeV. In a 50GeV jet it
1499 would be 0.39GeV. This is a region where the inclusive j_T distribution is domi-
1500 nated by background. The distribution is also steeply falling. Overestimating the
1501 background can lead to a situation where the background estimation exceeds the
1502 inclusive distribution.

1503 To take this effect into account we can't use a fixed axis for background, but
1504 it has to behave like a jet would when additional tracks are added. Thus before
1505 calculating j_T values we make a vector sum of the track and the axis used for back-
1506 ground, which is either the perpendicular cone axis or the random axis depending
1507 on the background method. In each case the momentum of this background axis
1508 is assumed to be the same as the jet which initiated the background estimation.

1509 In pPb data there is on average about one underlying event track in a $R = 0.4$
1510 cone.

1511 Extend Background, Perp. cone vs. Random

1512 5.5 Fitting

1513 The resulting signal distribution are fitted with a 2 component function shown in
1514 Eq. 29. Gaussian distribution is used for low j_T and an inverse gamma function is
1515 used for high j_T . The gaussian is taken to have the center at $j_T = 0$. In total this
1516 gives 5 parameters.

$$\frac{1}{N_{\text{jets}} j_T \text{d}j_T} \frac{\text{d}N}{\text{d}j_T} = \frac{B_2}{B_1 \sqrt{2\pi}} e^{-\frac{j_T^2}{2B_1^2}} + \frac{B_3 B_5^{B_4}}{\Gamma(B_4)} \frac{e^{-\frac{B_5}{j_T}}}{j_T^{B_4+1}} \quad (29)$$

1517 To achieve stable results the fitting is performed in two steps. First each
1518 component is fitted separately. Gaussian component is fitted to the low end in j_T .
1519 Inverse gamma component is fitted to j_T above 1 GeV/c. After getting the results
1520 from the individual fits they are combined into a single function with initial values
1521 from the individual results and an additional fit is performed. Fitting only the
1522 gaussian component to the entire distribution produces approximately the same
1523 result as the gaussian component in the two-component model.

1524 After getting the fit function $\sqrt{\langle j_T^2 \rangle}$ (RMS) and yield values are extracted
1525 separately from each component. The narrow component RMS is

$$\sqrt{\langle j_T^2 \rangle} = \sqrt{2}B_1,$$

1526 and the wide component RMS value is calculated as

$$\sqrt{\langle j_T^2 \rangle} = \frac{B_5}{\sqrt{(B_4 - 2)(B_4 - 3)}},$$

1527 where it is required that $B_4 > 3$.

1528 6 Systematic uncertainties

1529 Extend Systematics

1530 The systematic uncertainties in this analysis come from the background esti-
1531 mation, the unfolding procedure and the cuts used to select the tracks. Tracking
1532 uncertainties are estimated from variations of the track selection cuts defined in
1533 Sec. 2. The resulting variations in RMS are shown in Table 4. The uncertainties
1534 from unfolding and background subtraction are of the same magnitude.

1535 The systematics in background estimation were studied using an alternative
1536 method to extract the background, mainly the random background method. The
1537 resulting uncertainty is below 5% for the wide component RMS and below 9% for
1538 the narrow component RMS.

1539 The systematic uncertainty that arises from the unfolding procedure is esti-
1540 mated by performing the unfolding with two separate methods. Data corrected
1541 by the iterative unfolding method are used as the results and the SVD unfolding
1542 method is employed to estimate the uncertainty. In a PYTHIA closure test the
1543 true distribution was in general found to be between the unfolded distributions
1544 from the iterative and SVD method. The difference between the methods when
1545 unfolding data should give a reasonable estimate of the unfolding uncertainty. The
1546 resulting uncertainty is below 8% for both wide and narrow component RMS.

1547 The different source of the systematic uncertainty are considered as uncorre-
1548 lated and the values of each source are summed in quadrature. The resulting
1549 uncertainty is 9 % for the wide component RMS and 12 % for the narrow compo-
1550 nent RMS.

1551 There is no tracking and no unfolding uncertainty in the Monte Carlo simula-
1552 tions.

Table 3: Summary of systematic errors

Systematic	Wide RMS	Narrow RMS
Background	5 %	9 %
Unfolding	8 %	8 %
Tracking	? %	? %
Total	9 %	12%

₁₅₅₃ 7 TPC Upgrade?

1554 8 Systematic errors

1555 8.1 Background subtraction

1556 Fits are performed on both perpendicular cone and random background signals.
 1557 Difference between them is taken as the systematic error. The fits for individ-
 1558 ual bins from the random background method are shown in figure 40. Resulting
 1559 differences between the methods for different components are shown in figure 39.

1560 8.2 Unfolding

1561 Unfolding is performed using both SVD and Bayesian unfolding. Difference be-
 1562 tween the methods is taken as the systematic error. Since SVD unfolding does
 1563 not have a 2 dimensional options, the unfolding is done bin by bin. The resulting
 1564 distributions after SVD unfolding and background subtraction with the perpendic-
 1565 ular cone method are shown in fig ???. Resulting differences between the methods
 1566 for different components are shown in figure 41.

1567 8.3 Tracking

1568 8.4 Combining systematics

1569 Resulting systematic errors are shown in table 4. Systematic errors are combined
 1570 bin-by-bin in quadrature to get the total systematic errors.

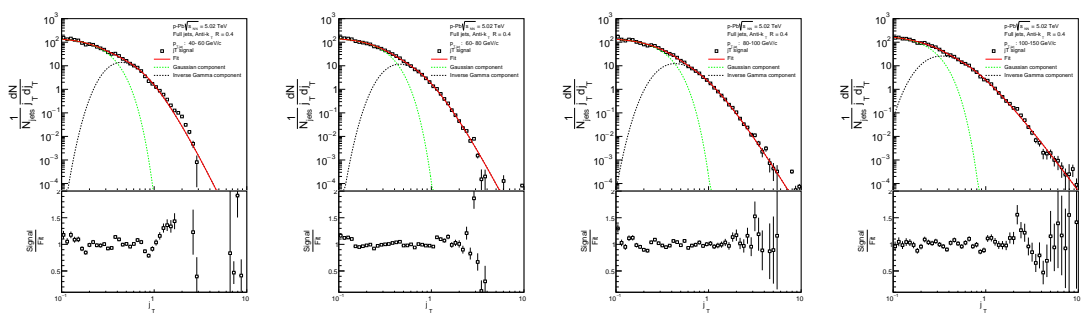


Figure 38: j_T signal with random background subtraction fits in different jet p_T bins

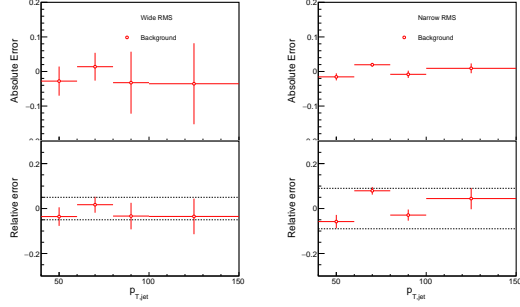


Figure 39: Differences between perpendicular cone and random background subtraction in the resulting RMS values.

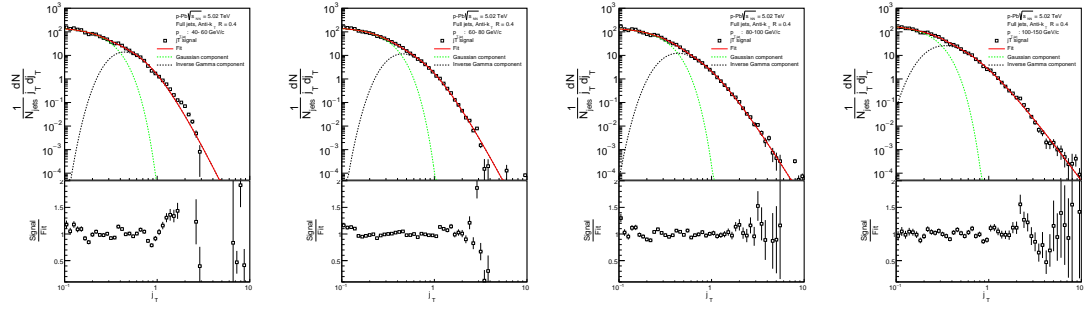


Figure 40: j_T signal with random background subtraction fits in different jet p_T bins

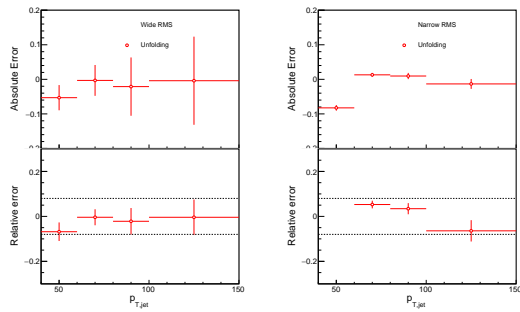


Figure 41: Differences between Bayesian and SVD unfolding in the resulting RMS values

Table 4: Summary of systematic errors

Systematic	Wide RMS	Narrow RMS
Background	5 %	9 %
Unfolding	8 %	8 %
Total	9 %	12%

1571 9 Results

1572 9.1 statistics

1573 Number of jets in different datasets and with different jet finders is shown in table
 1574 5. Background statistics for number of background cones (number of jets minus
 1575 number of discarded cones) are shown in table 6. Ratio of background cones to
 1576 number of jets is shown in table 7. The likelihood of having to discard a jet from
 background calculation is about 1-2%.

Table 5: Number of found jets by dataset and jet p_T bin

Jet p_T	5-10	10-20	20-30	30-40	40-60	60-80	80-100	100-150	150-500
MBFullR04	4969393	621753	32552	5584	1974	310	90	37	5
MBFullR05	4750567	826598	42373	5543	1719	276	73	29	3
MBChargedR04	3144538	673419	37783	4121	1009	148	36	12	1
MBChargedR05	2229247	175763	7961	1270	410	61	12	3	
TriggeredFullR04	187557	115927	78138	51317	39262	8621	2409	1167	171
TriggeredFullR05	99991	77147	48612	34325	28104	6342	1726	794	104
TriggeredChargedR04	37411	29945	18186	13148	11142	2517	675	326	44
TriggeredChargedR05	433155	175031	54789	19776	10626	1983	457	194	15

1577

Table 6: Number of background cones used in perpendicular cone background calculation

Jet p_T	5-10	10-20	20-30	30-40	40-60	60-80	80-100	100-150	150-500
MBFullR04	4947583	617895	32357	5548	1965	310	90	37	5
MBFullR05	4710217	815461	41584	5439	1698	273	73	29	3
MBChargedR04	3117495	661106	36739	4014	988	144	36	12	1
MBChargedR05	2195286	172919	7860	1249	406	61	12	3	
TriggeredFullR04	186574	115376	77949	51216	39196	8603	2405	1167	171
TriggeredFullR05	99102	76462	48320	34216	28038	6334	1722	794	103
TriggeredChargedR04	37160	29543	17988	13099	11129	2515	675	326	44
TriggeredChargedR05	313421	140707	45229	16243	8709	1604	377	154	14

Table 7: Ratio of background cone number to number of jets

MBFullR04	99.56%	99.38%	99.40%	99.36%	99.54%	100.00%	100.00%	100.00%	100.00%
MBFullR05	99.15%	98.65%	98.14%	98.12%	98.78%	98.91%	100.00%	100.00%	100.00%
MBChargedR04	99.14%	98.17%	97.24%	97.40%	97.92%	97.30%	100.00%	100.00%	100.00%
MBChargedR05	98.48%	98.38%	98.73%	98.35%	99.02%	100.00%	100.00%	100.00%	100.00%
TriggeredFullR04	99.48%	99.52%	99.76%	99.80%	99.83%	99.79%	99.83%	100.00%	100.00%
TriggeredFullR05	99.11%	99.11%	99.40%	99.68%	99.77%	99.87%	99.77%	100.00%	99.04%
TriggeredChargedR04	99.33%	98.66%	98.91%	99.63%	99.88%	99.92%	100.00%	100.00%	100.00%
TriggeredChargedR05	72.36%	80.39%	82.55%	82.13%	81.96%	80.89%	82.49%	79.38%	93.33%

1578 9.2 Data

1579 9.3 Inclusive results

1580 Results in figure 42

1581 As outlined in Section ?? the inclusive j_T distributions and corresponding
 1582 backgrounds are obtained for different jet p_T bins starting from $10 \text{ GeV} < p_{T\text{jet}} <$

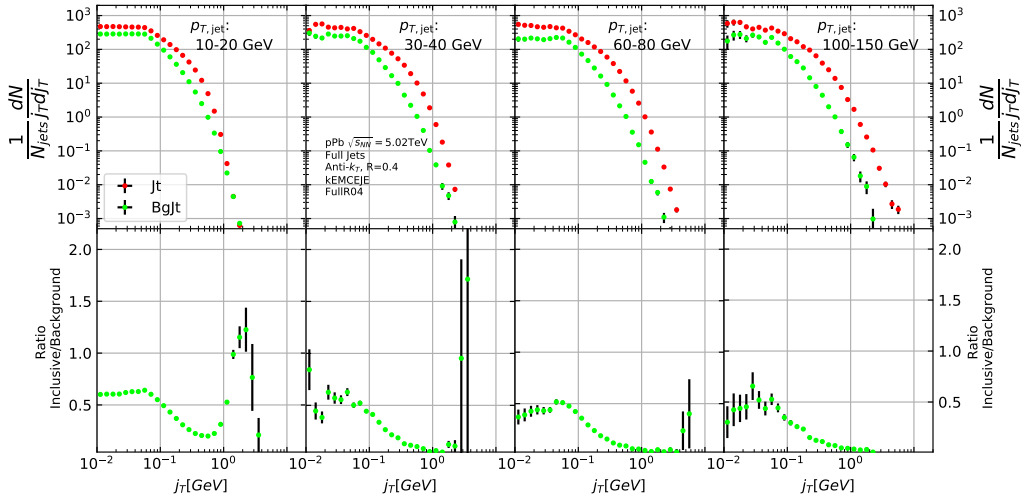


Figure 42: Inclusive j_T with background

20 GeV. Later the lowest p_T bins are omitted because of problems in unfolding and fitting. The results are shown in Fig. 42. The background distribution the figure is obtained by the perpendicular cone method.

9.4 Background

Comparison between perpendicular cone and random background in figure 43. The advantage of the random background method is the added amount of statistics as the procedure can be repeated several times for each event. However, it seems that, especially in the highest $p_{T,jet}$ bins there is some jet contribution left at the high end. One should note that the results from perpendicular cone background show no observable change between $p_{T,jet}$ bins. It is a good indication that the background is actually dominated by the underlying event over the entire j_T region.

9.5 Comparison between A and C side

In 2013 there were some issues with tracking. To rule out effects on j_T distributions a study was performed comparing j_T distributions between A and C side. No systematic differences were observed.

9.6 Subtracted signal

Results in figure 45. Comparison between signals with different backgrounds in figure 46

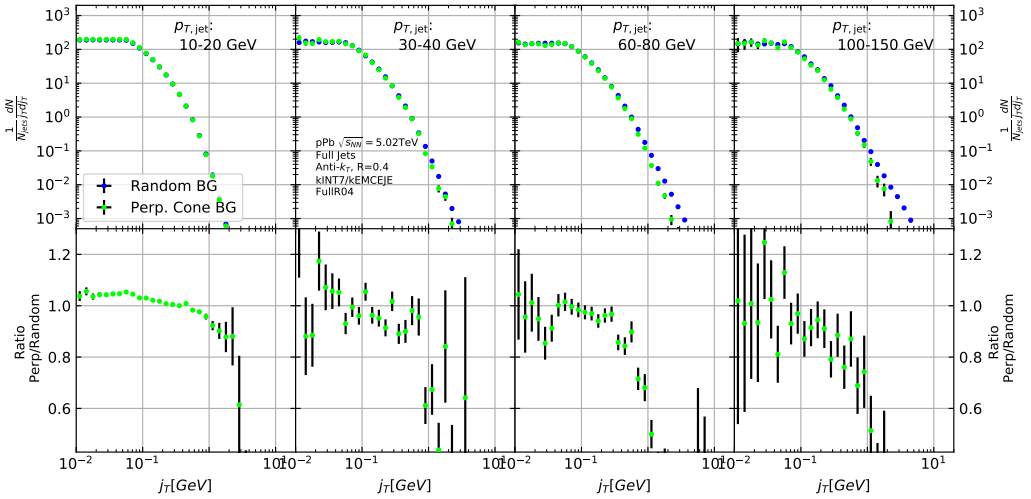


Figure 43: j_T background with two different methods

9.7 Fitting

Fits of j_T distributions in different jet p_T bins with $p_T > 40\text{GeV}$ are shown in figure 47. Additional jet p_T bins are shown in appendix ???. In lowest jet p_T bins the jets are mainly combinatorial which makes background subtraction and unfolding difficult and thus the signal can't be trusted.

The fits describe the data well. There is some fluctuation of the order of 10 % around the fit function. At hight j_T the statistical errors in the signal are large.

9.7.1 Results

RMS and yield results with systematic errors are shown separately in figure 48. Figure 49 shows RMS values for both components combined. The figure also includes results from a PYTHIA simulation.

9.8 Comparison to dihadron results

Comparison to RMS values in dihadron analysis [?] are shown in figure Dihadron results from [?]. For comparison the dihadron trigger p_T bins are converted to jet p_T bins and vice versa. Bin-by-bin comparison is still not possible, but dihadron analysis gives systematically larger RMS values. This could be caused by several kinematical factors. In jet j_T analysis the jet cone limits possible j_T values and thus the width and RMS of the j_T distributions. The effect of this limitation can be studied by changing the cone size as is described in section 9.9.

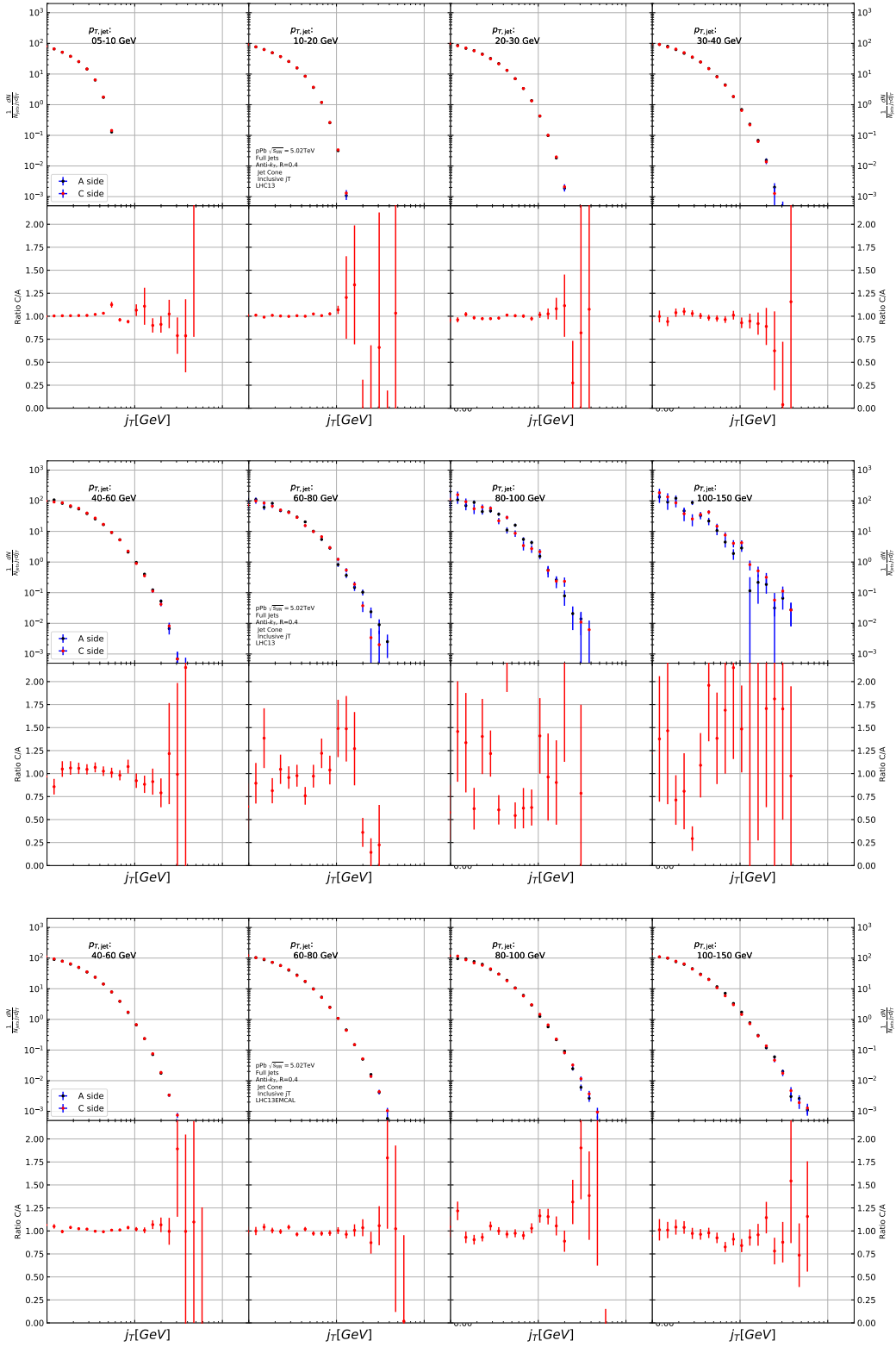


Figure 44: Comparison of inclusive j_{T8} distributions between A and C side for minimum bias and EMCAL triggered data.

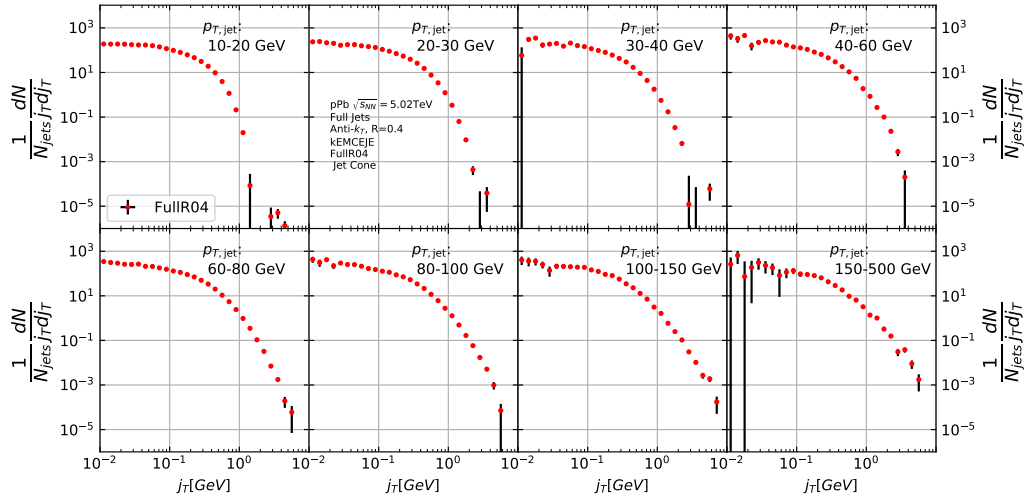


Figure 45: j_T signal with background subtracted

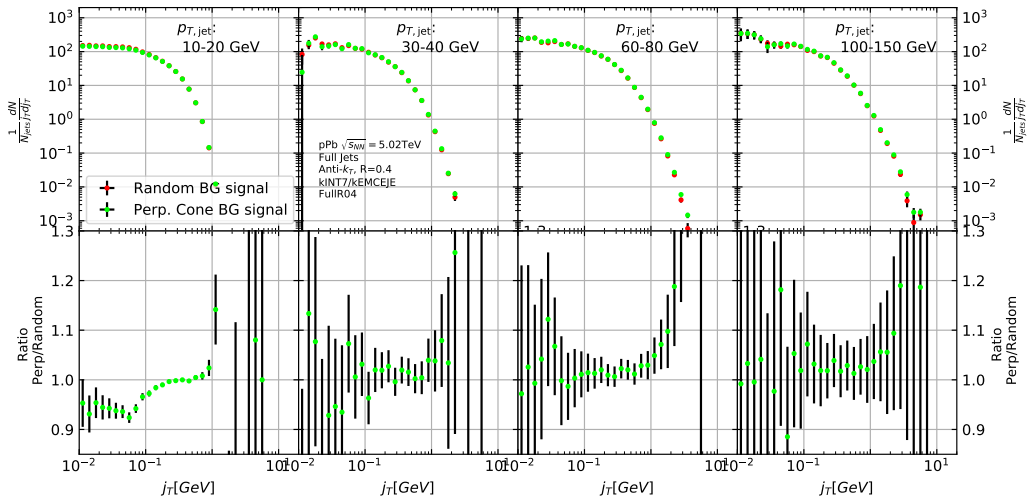


Figure 46: Comparison of the effect of background method on j_T signal.

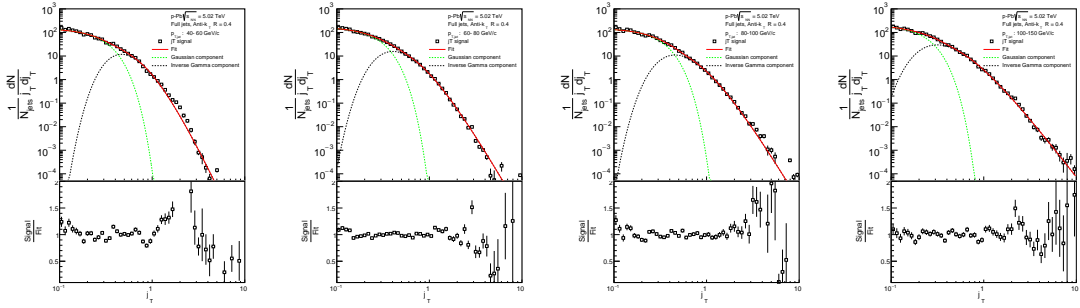


Figure 47: j_T signal fits in different jet p_T bins

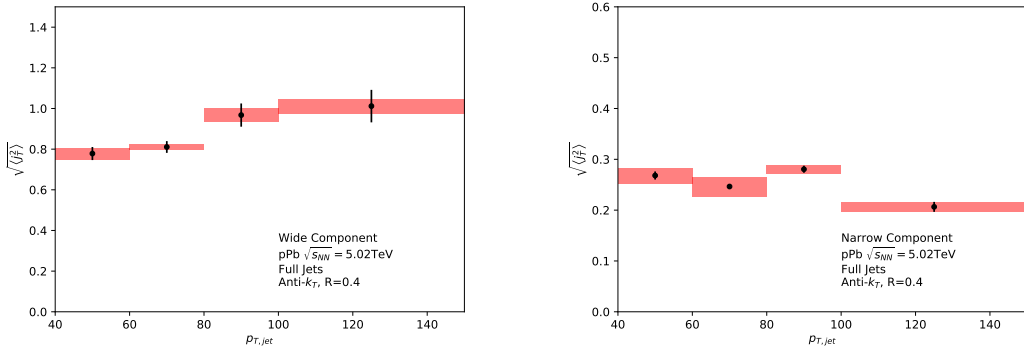


Figure 48: RMS values extracted from the fits for the gaussian (narrow) and inverse gamma (wide) components

1620 Comparison to j_T results from dihadron analysis [?] is shown in figure 55.
 1621 Trigger p_T bins used in dihadron analysis are converted to jet p_T bins using ob-
 1622 served average jet p_T values in leading track momentum bins. Similarly jet p_T bins
 1623 are converted to $p_{T,\text{trigger}}$ bins using average leading track p_T values in $p_{T,\text{jet}}$ bins.

1624 The trends are similar in dihadron and jet j_T results. Wide component RMS
 1625 values tend to increase with increasing $p_{T,\text{trigger}}/p_{T,\text{jet}}$. Narrow component RMS
 1626 increases slightly in dihadron analysis but not in jet j_T , WHY? (Depends on x_{\parallel}
 1627 bin in dihadron)

1628 In general dihadron j_T gives wider distributions with larger RMS values. In
 1629 jet analysis the cone size limits width and thus the RMS values. The effect of this
 1630 limitation can be studied by changing the cone size as is described in section 9.9.

1631 Additionally the leading track is an imperfect estimate of the jet/original par-
 1632 ton. Because the leading track in general is at an angle compared to the jet axis,
 1633 the resulting j_T values are different. In practice the jet axis found by the jet finding
 1634 algorithm tends to minimize the average j_T of jet constituents. Thus the yield at

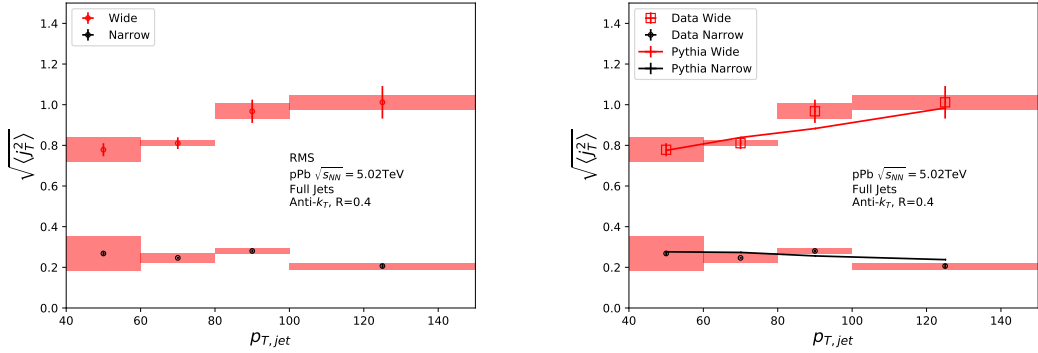


Figure 49: RMS values extracted from the fits for the gaussian (narrow) and inverse gamma (wide) components

1635 high j_T is limited and the RMS values are smaller.

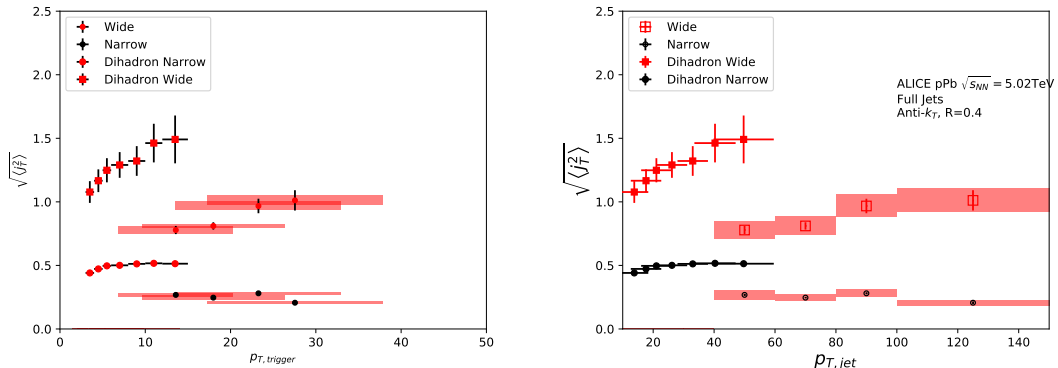


Figure 50: Jet j_T results are compared to results obtained in the dihadron analysis. This is done both in jet p_T and trigger p_T bins by converting between them.

1636 9.9 Different R parameters

1637 Study the effect of cone sizes on j_T distribution in particle level Pythia.

1638 Increasing the cone size of jets gives more room for high j_T tracks. This is seen
1639 in the individual j_T distributions as increased high j_T production. At low j_T there
1640 is no change.

1641 When looking at RMS values from wide component we see an increase/decrease
1642 of about 10% when going from $R = 0.4$ to $R = 0.5/R = 0.3$.

1643 The message from narrow component RMS values is less clear. At low jet p_T
 the behaviour is similar, but at high p_T the order is reversed.

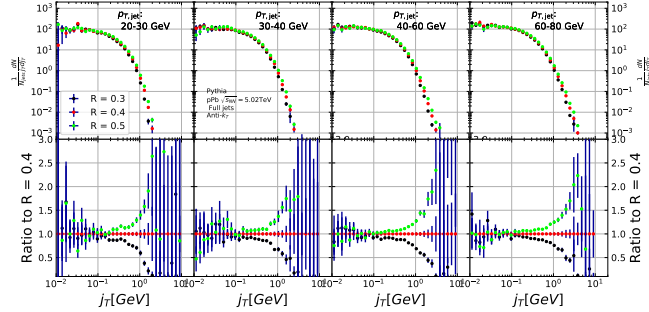


Figure 51: Effect of changing R parameter in jet finding on j_T distributions

1644

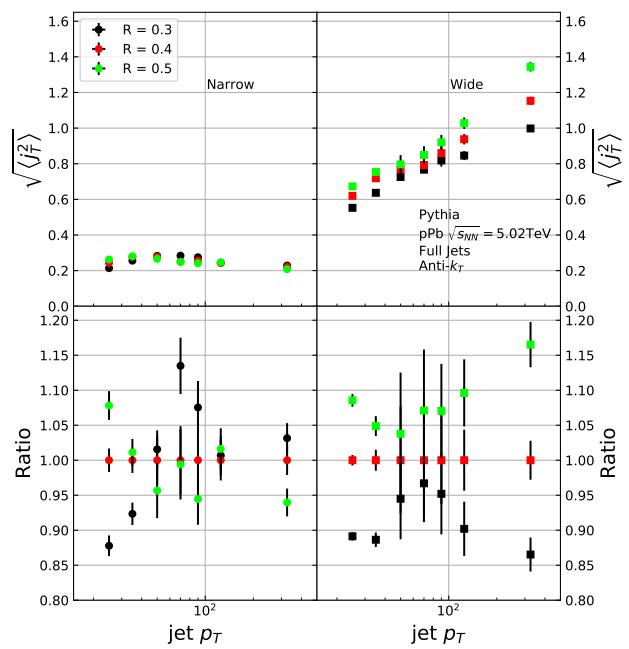


Figure 52: Effect of changing R parameter in jet finding on narrow and wide component RMS values. Wide component RMS values increase with increasing cone size.

1645 10 Discussion

1646 10.1 Discussion

1647 10.1.1 Dihadron j_T

1648 The jet fragmentation transverse momentum j_T has been studied previously at
 1649 ALICE with dihadron correlations [107]. The study took the leading hadron in
 1650 each event and calculated j_T for any near-side tracks with respect to the leading
 1651 hadron. Thus there is no kinematical limit to j_T from the jet cone. In the analysis
 1652 the background shape is estimated using pairs with large $\Delta\eta$. The normalisation of
 1653 the background is done when fitting the j_T distribution. The inclusive and signal
 1654 distributions from the analysis are shown in Fig. 53. The inclusive distribution is
 1655 fitted with a three component function,

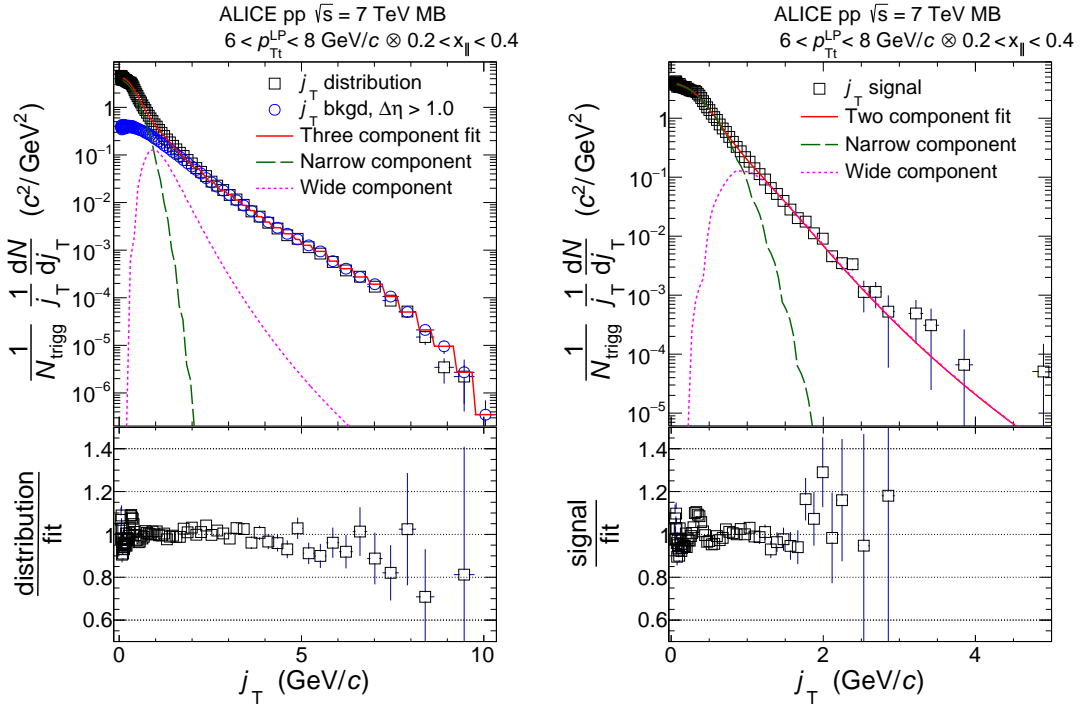


Figure 53: *Left:* Measured j_T distribution including a three-component fit. The three components describe the background (circular symbols), hadronization (long dashed line), and showering (short dashed line). *Right:* The same j_T distribution but with background subtracted.

1656 The analysis was the first to introduce this factorisation of j_T into components.
 1657 At $j_T \approx 0.4$ GeV there is a small bump in the distribution to fit ratio. This
 1658 was attributed to cases where the trigger particle decayed after hadronisation. As

it is difficult to correct for, this bump is included in the systematic errors of the results.

The RMS results from the fitting in both pp and p-Pb collisions are shown in Fig. 54. Qualitatively the results are similar to jet j_T results. The RMS value of the wide component has an increasing trend with respect to p_{Tt}/p_{Tjet} , while the RMS value of the narrow component stays constant. Both components are well described by PYTHIA simulations.

In the dihadron analysis there is no difference between pp and p-Pb results.

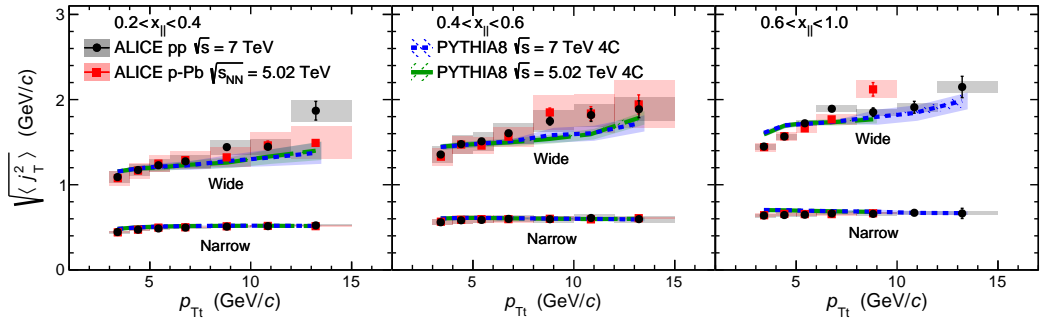


Figure 54: RMS values of the narrow and wide j_T components in the dihadron correlation analysis. Results from pp collisions at $\sqrt{s} = 7$ TeV (circular symbols) and from p-Pb collisions at $\sqrt{s_{NN}} = 5.02$ TeV (square symbols) are compared to PYTHIA 8 tune 4C simulations at $\sqrt{s} = 7$ TeV (short dashed line) and at $\sqrt{s} = 5.02$ TeV (long dashed line). Different panels correspond to different x_{\parallel} bins with $0.2 < x_{\parallel} < 0.4$ on the left, $0.4 < x_{\parallel} < 0.6$ in the middle, and $0.6 < x_{\parallel} < 1.0$ on the right. The statistical errors are represented by bars and the systematic errors by boxes. [107]

Comparison between jet and dihadron j_T results shown in Fig. 55. Trigger p_T bins used in dihadron analysis are converted to jet p_T bins using observed average jet p_T values in leading track momentum bins. Similarly jet p_T bins are converted to $p_{T\text{trigger}}$ bins using average leading track p_T values in $p_{T\text{jet}}$ bins.

In general dihadron j_T gives wider distributions with larger RMS values. There are several factors that could explain this. In jet analysis the cone size limits width and thus the RMS values. With increasing cone size one gets increasing wide RMS values as seen in Fig. 56. This should be the dominant factor.

Effect of the R parameter choice is studied in PYTHIA. Having a fixed cone puts hard limits on the possible j_T values. Increasing the cone size loosens these limits and allows higher j_T values. The results are shown in Fig. 56. Left hand side shows the j_T distributions. There is very little change in low j_T but at high j_T the yield increases.

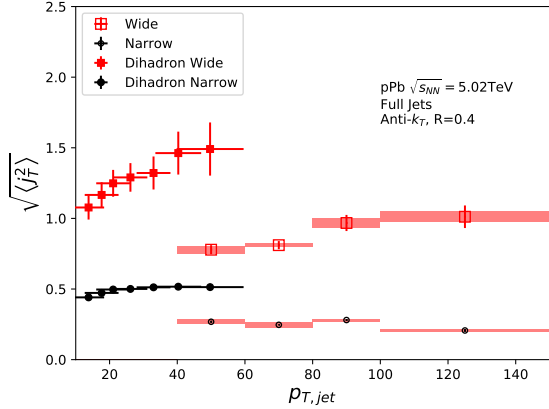


Figure 55: Comparison of results with dihadron j_T results. Dihadron trigger p_T bins are converted to jet p_T bins using observed mean $p_{T,jet}$ values in $p_{T,\text{trigger}}$ bins. Dihadron results are for $0.2 < x_{||} < 0.4$

This is also seen in the RMS values shown in the right hand side of Fig. 56, where the change in wide component RMS is about 10% when going from $R = 0.4$ to $R = 0.3$ or $R = 0.5$. With the narrow component values the situation is less clear. At low jet p_T larger R parameter leads to larger RMS values, but at high $p_{T,jet}$ the situation is reversed; increasing the R parameter decreases RMS values.

Additionally the leading track is an imperfect estimate of the jet/original parton. Because the leading track in general is at an angle compared to the jet axis, the resulting j_T values are different. In practice the jet axis found by the jet finding algorithm tends to minimize the average j_T of jet constituents. Thus the yield at high j_T is limited and the RMS values are smaller.

A PYTHIA study was performed where j_T was calculated with respect to the leading track momentum, instead of the jet axis. The results are shown in Fig. 57. The resulting j_T distributions are significantly wider than j_T distributions from the typical method. The effect seems to be larger than the effect seen in comparing different R values.

Lastly the results from the dihadron analysis are done in $p_{T,\text{trigger}}$ bins. This favours hard jets, i.e. jets where the leading hadron carries a large momentum fraction and the jet multiplicity is small. In $p_{T,jet}$ bins jets are more likely to be soft, i.e. small leading momentum fraction and high multiplicity jets.

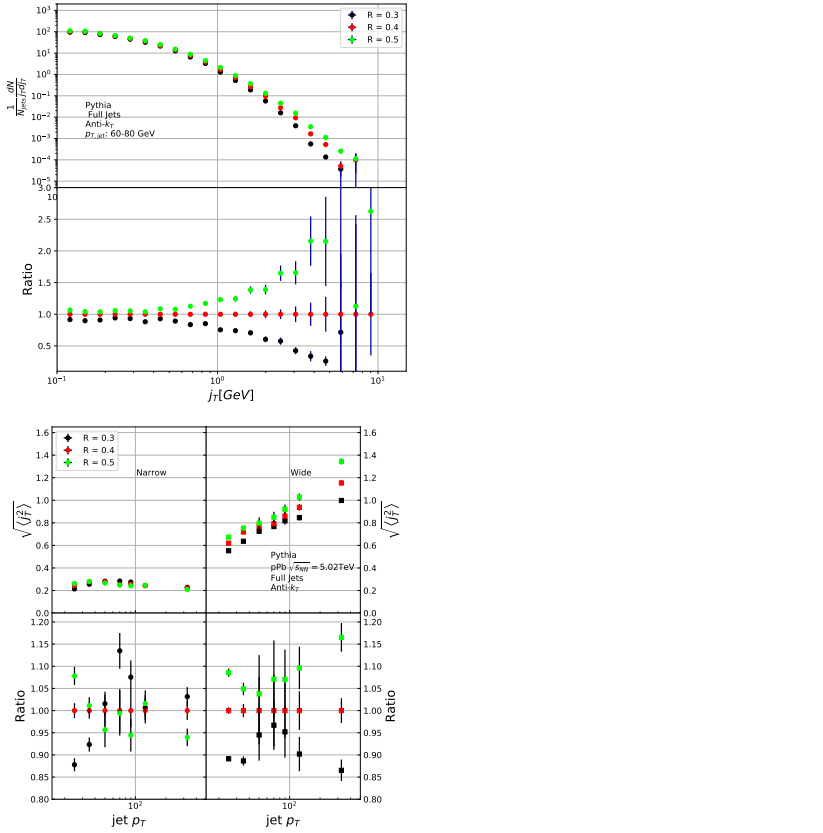


Figure 56: Effect of changing R parameter in jet finding on j_T distributions

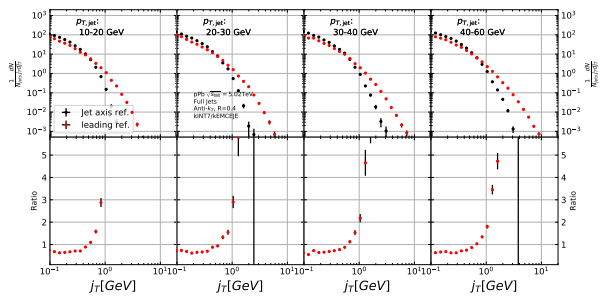


Figure 57: Results of calculating j_T with respect to the jet axis or the leading hadron. The assumption is that because the leading hadron is an imperfect estimate of the jet axis, low j_T tracks should on average be shifted to higher j_T

₁₆₉₉ **11 Summary**

₁₇₀₀ In this work two distinct j_T components were extracted for narrow and wide contri-
₁₇₀₁ butions using jet reconstruction. RMS values for both components were obtained.
₁₇₀₂ The width of the wide component is found to increase for increasing $p_{T\text{jet}}$. This
₁₇₀₃ is in part explained by the changing kinematical limits when going to higher $p_{T\text{jet}}$
₁₇₀₄ which allows higher $p_{T\text{track}}$. Additionally the larger phase space allows stronger
₁₇₀₅ parton splitting. The results are qualitatively compatible with previous studies
₁₇₀₆ that studied j_T using two-particle correlations.

₁₇₀₇ **References**

- ₁₇₀₈ [1] PHENIX Collaboration, K. Adcox *et al.*, Nucl.Phys. **A757**, 184 (2005), nucl-ex/0410003.
- ₁₇₀₉
- ₁₇₁₀ [2] STAR Collaboration, J. Adams *et al.*, Nucl.Phys. **A757**, 102 (2005), nucl-ex/0501009.
- ₁₇₁₁
- ₁₇₁₂ [3] J.-Y. Ollitrault, Phys. Rev. D **46**, 229 (1992).
- ₁₇₁₃ [4] U. Heinz and P. Kolb, Nucl. Phys. **A702**, 269 (2002).
- ₁₇₁₄ [5] E. Shuryak, Prog. Part. Nucl. Phys. **62**, 48 (2009).
- ₁₇₁₅ [6] ATLAS Collaboration, J. Jia, Nucl.Phys.A904-905 **2013**, 421c (2013), 1209.4232.
- ₁₇₁₆
- ₁₇₁₇ [7] R. A. Lacey *et al.*, (2012), 1207.1886.
- ₁₇₁₈ [8] R. Bjorklund, W. Crandall, B. J. Moyer, and H. York, Phys. Review **77**, 213 (1950).
- ₁₇₁₉
- ₁₇₂₀ [9] W. Heisenberg, Zeitschrift für Physik **77**, 1 (1932).
- ₁₇₂₁ [10] M. Gell-Mann, Phys. Rev. **125**, 1067 (1962).
- ₁₇₂₂ [11] M. Gell-Mann, Phys. Lett. **8**, 214 (1964).
- ₁₇₂₃ [12] O. Greenberg, Phys. Rev. Lett. **13**, 598 (1964).
- ₁₇₂₄ [13] Crystal Ball Collaboration, D. Williams *et al.*, Phys.Rev. **D38**, 1365 (1988).
- ₁₇₂₅ [14] W. Krolikowski, Nuovo Cim. **A27**, 194 (1975).
- ₁₇₂₆ [15] D. J. Gross and F. Wilczek, Physical Review Letters **30**, 1343 (1973).
- ₁₇₂₇ [16] H. D. Politzer, Physical Review Letters **30**, 1346 (1973).
- ₁₇₂₈ [17] D. J. Gross and F. Wilczek, Physical Review D **8**, 3633 (1973).
- ₁₇₂₉ [18] D. J. Gross and F. Wilczek, Physical Review D **9**, 980 (1974).
- ₁₇₃₀ [19] H. Georgi and H. D. Politzer, Physical Review D **9**, 416 (1974).
- ₁₇₃₁ [20] H. Fritzsch, M. Gell-Mann, and H. Leutwyler, Physics Letters B **47**, 365 (1973).
- ₁₇₃₂

- ₁₇₃₃ [21] I. Flegel and P. Söding, CERN courier (2004).
- ₁₇₃₄ [22] R. Brandelik *et al.*, Physics Letters B **86**, 243 (1979).
- ₁₇₃₅ [23] J. K. L. MacDonald, Phys. Rev. **43**, 830 (1933).
- ₁₇₃₆ [24] C. Berger *et al.*, Physics Letters B **86**, 418 (1979).
- ₁₇₃₇ [25] J. Collins and M. Perry, Phys. rev. Lett. **34**, 1353 (1975).
- ₁₇₃₈ [26] E. Shuryak, Phys. Reps. **61**, 71 (1980).
- ₁₇₃₉ [27] K. Rajagopal, SLAC Beam Line **31-2**, 9 (2001).
- ₁₇₄₀ [28] P. Kovtun, D. Son, and A. Starinets, Phys.Rev.Lett. **94**, 111601 (2005), hep-th/0405231.
- ₁₇₄₂ [29] R. A. Lacey *et al.*, Phys. Rev. Lett. **98**, 092301 (2007).
- ₁₇₄₃ [30] E. Lofgren, *ACCELERATOR DIVISION ANNUAL REPORTS, 1 JULY 1972 12/31/1974* (, 1975).
- ₁₇₄₅ [31] D. S. Barton, Heavy ion program at bnl: Ags, rhic, in *Proc. 1987 Particle Accelerator Conference, Washington, D.C., March, 1987*.
- ₁₇₄₇ [32] I. Vitev and M. Gyulassy, Phys.Rev.Lett. **89**, 252301 (2002), hep-ph/0209161.
- ₁₇₄₉ [33] S. Choi and K. S. Lee, Phys. Rev. C **84**, 064905 (2011).
- ₁₇₅₀ [34] A. Kovalenko *et al.*, Status of the nuclotron, in *Proceedings of EPAC Vol. 94*, pp. 161–164, 1994.
- ₁₇₅₂ [35] NA61/SHINE, K. Grebieszkow, PoS **CPOD2013**, 004 (2013).
- ₁₇₅₃ [36] BRAHMS Collaboration, I. Arsene *et al.*, Nucl.Phys. **A757**, 1 (2005), nucl-ex/0410020.
- ₁₇₅₅ [37] B. Back *et al.*, Nucl.Phys. **A757**, 28 (2005), nucl-ex/0410022.
- ₁₇₅₆ [38] S. A. Voloshin, A. M. Poskanzer, and R. Snellings, (2008), 0809.2949.
- ₁₇₅₇ [39] S. A. Voloshin, A. M. Poskanzer, A. Tang, and G. Wang, Phys.Lett. **B659**, 537 (2008), 0708.0800.
- ₁₇₅₉ [40] H. Holopainen, H. Niemi, and K. J. Eskola, Phys.Rev. **C83**, 034901 (2011), 1007.0368.

- ₁₇₆₁ [41] ALICE Collaboration, Phys. Rev. C **88**, 044909 (2013).
- ₁₇₆₂ [42] M. L. Miller, K. Reygers, S. J. Sanders, and P. Steinberg, Ann.Rev.Nucl.Part.Sci. **57**, 205 (2007), nucl-ex/0701025.
- ₁₇₆₄ [43] R. Glauber, Lectures in theoretical physics, 1959.
- ₁₇₆₅ [44] W. Czyż and L. Maximon, Annals of Physics **52**, 59 (1969).
- ₁₇₆₆ [45] A. Białłas, M. Bleszyński, and W. Czyż, Nuclear Physics B **111**, 461 (1976).
- ₁₇₆₇ [46] PHENIX Collaboration, S. Afanasiev *et al.*, Phys.Rev. **C80**, 054907 (2009), 0903.4886.
- ₁₇₆₉ [47] J.-Y. Ollitrault, Eur.J.Phys. **29**, 275 (2008), 0708.2433.
- ₁₇₇₀ [48] P. Romatschke, Int.J.Mod.Phys. **E19**, 1 (2010), 0902.3663.
- ₁₇₇₁ [49] L. LD, Izv. Akad. Nauk Ser. Fiz. **17**, 51 (1953).
- ₁₇₇₂ [50] H. Song, S. Bass, and U. W. Heinz, (2013), 1311.0157.
- ₁₇₇₃ [51] H. Niemi, G. Denicol, P. Huovinen, E. Molnar, and D. Rischke, Phys.Rev. **C86**, 014909 (2012), 1203.2452.
- ₁₇₇₅ [52] K. A. *et al.* [ALICE Collaboration], Phys. Rev. Lett **106** (2011), 032301.
- ₁₇₇₆ [53] J.-Y. Ollitrault, Phys.Rev. D **48**, 1132 (1993), hep-ph/9303247.
- ₁₇₇₇ [54] P. Danielewicz and G. Odyniec, Physics Letters B **157**, 146 (1985).
- ₁₇₇₈ [55] P. Danielewicz and M. Gyulassy, Physics Letters B **129**, 283 (1983).
- ₁₇₇₉ [56] T. Abbott *et al.*, Phys. Rev. Lett. **70**, 1393 (1993).
- ₁₇₈₀ [57] S. Voloshin and Y. Zhang, Z.Phys. **C70**, 665 (1996), hep-ph/9407282.
- ₁₇₈₁ [58] E877 Collaboration, J. Barrette *et al.*, Phys.Rev.Lett. **73**, 2532 (1994), hep-ex/9405003.
- ₁₇₈₃ [59] CMS Collaboration, S. Chatrchyan *et al.*, Phys.Rev.Lett. **109**, 022301 (2012), 1204.1850.
- ₁₇₈₅ [60] A. Majumder and M. Van Leeuwen, Prog.Part.Nucl.Phys. **A66**, 41 (2011), 1002.2206.

- ₁₇₈₇ [61] F. Dominguez, C. Marquet, A. Mueller, B. Wu, and B.-W. Xiao, Nucl.Phys. **A811**, 197 (2008), 0803.3234.
- ₁₇₈₉ [62] M. Gyulassy, P. Levai, and I. Vitev, Nucl.Phys. **B571**, 197 (2000), hep-ph/9907461.
- ₁₇₉₁ [63] U. A. Wiedemann, Nucl.Phys. **B588**, 303 (2000), hep-ph/0005129.
- ₁₇₉₂ [64] P. B. Arnold, G. D. Moore, and L. G. Yaffe, JHEP **0112**, 009 (2001), hep-ph/0111107.
- ₁₇₉₄ [65] X.-N. Wang and X.-f. Guo, Nucl.Phys. **A696**, 788 (2001), hep-ph/0102230.
- ₁₇₉₅ [66] T. Sjostrand, S. Mrenna, and P. Z. Skands, Comput.Phys.Commun. **178**, 852 (2008), 0710.3820.
- ₁₇₉₇ [67] I. Lokhtin and A. Snigirev, Eur.Phys.J. **C45**, 211 (2006), hep-ph/0506189.
- ₁₇₉₈ [68] N. Armesto, L. Cunqueiro, and C. A. Salgado, Nucl.Phys. **A830**, 271C (2009), 0907.4706.
- ₁₈₀₀ [69] K. Zapp, G. Ingelman, J. Rathsman, J. Stachel, and U. A. Wiedemann, Eur.Phys.J. **C60**, 617 (2009), 0804.3568.
- ₁₈₀₂ [70] T. Renk, Phys.Rev. **C79**, 054906 (2009), 0901.2818.
- ₁₈₀₃ [71] ALICE Collaboration, K. Aamodt *et al.*, Phys.Lett. **B696**, 30 (2011), 1012.1004.
- ₁₈₀₅ [72] WA98 Collaboration, M. Aggarwal *et al.*, Eur.Phys.J. **C23**, 225 (2002), nucl-ex/0108006.
- ₁₈₀₇ [73] D. G. d'Enterria, Phys.Lett. **B596**, 32 (2004), nucl-ex/0403055.
- ₁₈₀₈ [74] PHENIX Collaboration, A. Adare *et al.*, Phys.Rev.Lett. **101**, 232301 (2008), 0801.4020.
- ₁₈₁₀ [75] STAR Collaboration, J. Adams *et al.*, Phys.Rev.Lett. **91**, 172302 (2003), nucl-ex/0305015.
- ₁₈₁₂ [76] A. Dainese, C. Loizides, and G. Paic, Eur.Phys.J. **C38**, 461 (2005), hep-ph/0406201.
- ₁₈₁₄ [77] I. Vitev, J.Phys. **G30**, S791 (2004), hep-ph/0403089.
- ₁₈₁₅ [78] C. A. Salgado and U. A. Wiedemann, Phys.Rev. **D68**, 014008 (2003), hep-ph/0302184.

- ₁₈₁₇ [79] N. Armesto, A. Dainese, C. A. Salgado, and U. A. Wiedemann, Phys.Rev. **D71**, 054027 (2005), hep-ph/0501225.
- ₁₈₁₉ [80] T. Renk, H. Holopainen, R. Paatelainen, and K. J. Eskola, Phys.Rev. **C84**, 014906 (2011), 1103.5308.
- ₁₈₂₁ [81] CMS Collaboration, S. Chatrchyan *et al.*, Eur.Phys.J. **C72**, 1945 (2012), 1202.2554.
- ₁₈₂₃ [82] PHENIX Collaboration, S. Afanasiev *et al.*, Phys. Rev. C **80**, 054907 (2009).
- ₁₈₂₄ [83] ALICE Collaboration, K. Aamodt *et al.*, Phys.Rev.Lett. **108**, 092301 (2012), 1110.0121.
- ₁₈₂₆ [84] J. L. Nagle and W. A. Zajc, Ann. Rev. Nucl. Part. Sci. **68**, 211 (2018), 1801.03477.
- ₁₈₂₈ [85] E735, T. Alexopoulos *et al.*, Phys. Rev. **D48**, 984 (1993).
- ₁₈₂₉ [86] MiniMax, T. C. Brooks *et al.*, Phys. Rev. **D61**, 032003 (2000), hep-ex/9906026.
- ₁₈₃₁ [87] C. Shen, Z. Qiu, and U. Heinz, Phys. Rev. **C92**, 014901 (2015), 1502.04636.
- ₁₈₃₂ [88] PHENIX, A. Adare *et al.*, Phys. Rev. **C94**, 064901 (2016), 1509.07758.
- ₁₈₃₃ [89] C. A. Salgado and J. P. Wessels, Ann. Rev. Nucl. Part. Sci. **66**, 449 (2016).
- ₁₈₃₄ [90] M. Gyulassy, I. Vitev, X.-N. Wang, and B.-W. Zhang, p. 123 (2003), nucl-th/0302077.
- ₁₈₃₆ [91] E. Norbeck, K. Šafařík, and P. A. Steinberg, Annual Review of Nuclear and Particle Science **64**, 383 (2014), <https://doi.org/10.1146/annurev-nucl-102912-144532>.
- ₁₈₃₉ [92] A. Accardi, F. Arleo, W. K. Brooks, D. D'Enterria, and V. Muccifora, Riv. Nuovo Cim. **32**, 439 (2010), 0907.3534.
- ₁₈₄₁ [93] ALICE, K. Aamodt *et al.*, JINST **3**, S08002 (2008).
- ₁₈₄₂ [94] ALICE, B. B. Abelev *et al.*, Int. J. Mod. Phys. **A29**, 1430044 (2014), 1402.4476.
- ₁₈₄₄ [95] ALICE, K. Aamodt *et al.*, JINST **5**, P03003 (2010), 1001.0502.
- ₁₈₄₅ [96] J. Alme *et al.*, Nucl. Instrum. Meth. **A622**, 316 (2010), 1001.1950.

- ₁₈₄₆ [97] ALICE, B. Abelev *et al.*, JHEP **03**, 053 (2012), 1201.2423.
- ₁₈₄₇ [98] ALICE, P. Cortese *et al.*, (2008).
- ₁₈₄₈ [99] J. Allen *et al.*, Report No. CERN-LHCC-2010-011. ALICE-TDR-14-add-1,
₁₈₄₉ 2010 (unpublished).
- ₁₈₅₀ [100] ALICE, G. Dellacasa *et al.*, (1999).
- ₁₈₅₁ [101] ALICE Collaboration, *Technical Design Report on Forward Detectors: FMD, T0 and V0*, 2004.
- ₁₈₅₃ [102] ALICE, B. Abelev *et al.*, Phys. Lett. **B719**, 29 (2013), 1212.2001.
- ₁₈₅₄ [103] M. Cacciari, G. P. Salam, and G. Soyez, Eur. Phys. J. **C72**, 1896 (2012),
₁₈₅₅ 1111.6097.
- ₁₈₅₆ [104] M. Cacciari, G. P. Salam, and G. Soyez, JHEP **04**, 063 (2008), 0802.1189.
- ₁₈₅₇ [105] T. Sjöstrand, S. Mrenna, and P. Z. Skands, Comput. Phys. Commun. **178**,
₁₈₅₈ 852 (2008), 0710.3820.
- ₁₈₅₉ [106] Roounfold: Root unfolding framework, <http://hepunx.rl.ac.uk/~adye/software/unfold/RooUnfold.html>, 2013.
- ₁₈₆₁ [107] <https://alice-publications.web.cern.ch/node/3655>, 2018.